

Probing Our Heliospheric History: Constructing a Density Profile of the ISM in the Sun's Rearview Mirror

by

Katherine Wyman

Advisor: Dr. Seth Redfield

A thesis submitted to the
faculty of Wesleyan University
in partial fulfillment of the requirements for the
Degree of Master of Arts
in Astronomy

“What’s past is prologue”

–The Tempest

Acknowledgments

First off I'm thankful beyond words to my advisor Seth Redfield. Thank you for helping me realize that the interstellar medium IS cool, for never EVER giving me an answer right away, for making me figure out so many things on my own, and for expecting more from me than I ever thought I was capable of. You were an incredible mentor.

Secondly, thank you to my entire family for their boundless love and support throughout my education. Thanks to my wonderful parents for pushing me onwards and to my amazing little sister for keeping me grounded, I wouldn't have made it as far as I have if it weren't for you.

Thank you to Roy and Adam J. for putting up with my incessant questioning and for forgiving my general programming ignorance. There's really no way I would have even made my first plot without your help.

Thank you to my dear friends and fellow astronomers: Adam M., Holly, Karlen, Marshall, Jake, and Tyler for being just amazing people to work with. Thanks to Holly for being such a great officemate and for commiserating with me when I needed it, you are the wind beneath my baby-eagle wings. To my fellow Redtails: keep fighting the good fight. Go team exoplanet!

Finally my sincere thanks to Ed for convincing me to come to Wesleyan in the first place, and thank you to the entire Wesleyan astronomy community for making the last two years such an invaluable experience.

Abstract

In the course of our motion through the Galaxy, the solar system has encountered many interstellar environments of varying characteristics. Interstellar medium (ISM) density variations spanning six orders of magnitude are commonly seen throughout the general Galactic environment, and a sufficiently dense cloud within this range has the potential to compress the heliosphere to within one Astronomical Unit (AU). We present a reconstruction of the density profile for the clouds we have most recently passed through based on high-resolution optical spectra towards nearby stars. The data were obtained with the Harlan J. Smith 2.7-meter telescope coudé spectrographs at McDonald Observatory and the Ultra High Resolution Facility on the 3.9 meter Anglo-Australian Telescope at the Anglo-American Observatory. Observations were made of interstellar NaI and CaII doublet absorption towards 49 bright stars along the historical path of solar motion in our orbit around the center of the Galaxy. Spectra were taken of stars out to a distance of 480 parsecs, with a median separation distance of 5 parsecs between adjacent stars. No absorption is seen out to a distance of 120 pc (consistent with the Local Bubble), but a complex collection of absorbers (up to 10 components) is seen in stars between 130 and 480 pc. A possible link between our local interstellar environment, cosmic rays, and our planetary climate has long been a subject of interest to members of the astronomical community. Compression of the heliosphere (one of our three cosmic ray shields together with the Earth's magnetosphere and atmosphere) due to the Sun's passage through a dense interstellar cloud could have drastic effects on Earth's climate: global cool-

ing from atmospheric dust deposition, weather patterns from cloud nucleation due to an increased cosmic ray flux, and evolution from higher mutation rates for life forms. A timescale of interaction with each ISM component in this path can be constructed and ultimately compared with geologic records.

Contents

1	Introduction	1
1.1	The Interstellar Medium	2
1.1.1	Our Local Interstellar Environment	3
1.2	The Heliosphere	6
1.2.1	Heliospheric Structure	7
1.3	Heliospheric Variability	9
1.3.1	Solar Variability	10
1.3.2	Interstellar Variability	11
1.4	Cosmic Rays and the Heliosphere	12
1.4.1	Cosmic Ray Consequences	13
1.4.2	Comparison with the Geologic Record	15
2	Observations and Data Reduction	19
2.1	Stellar Parameters	21
2.2	Observations	23
2.2.1	Telescopes	23
2.2.2	Observational Parameters	25
2.2.3	Data Reduction Steps	30

3	ISM Absorption Measurements	35
3.1	Measuring ISM Absorption	35
3.1.1	Multiple Instrument Resolution Fits	37
3.2	Fits	41
3.3	Fit Results	59
3.4	Histograms	65
3.5	Apparent Optical Depth	68
4	Results	73
4.1	Column Density Profile	73
4.1.1	Cone Restriction	77
4.1.2	Distance Slices	79
4.2	Developing a Monotonic Profile	81
4.2.1	Boltzmann Method	81
4.2.2	Brute Force Method	85
4.3	Volume Densities from the Monotonic Fits	86
4.3.1	Volume Densities from the Brute Force Fits	88
4.3.2	Volume Densities from the Boltzmann Fits	90
4.4	The Component-by-Component Method	91
5	Discussion	98
5.1	Heliosphere Size	98
5.1.1	Historical Heliospheric Response	101
5.1.2	Cosmic Ray Modulation	104
6	Conclusions	106
6.1	Summary of Results	106

6.2	Future Work	107
6.2.1	The Literal Future	107
	Bibliography	109

List of Tables

1.1	Components of the Interstellar Medium	2
2.1	Stellar Parameters for Targets along the Past Solar Trajectory ^a . .	24
2.2	Observational Parameters for Stars along the Past Solar Trajectory	26
2.2	Observational Parameters for Stars along the Past Solar Trajectory	27
2.3	Observational Parameters for Stars along the Past Solar Trajectory	28
2.3	Observational Parameters for Stars along the Past Solar Trajectory	29
3.1	Multiple Instrument Resolution Fits	40
3.2	Ca II ISM Fit Parameters for Targets along the Past Solar Trajectory	60
3.2	Ca II ISM Fit Parameters for Targets along the Past Solar Trajectory	61
3.3	Ca II ISM Fit Parameters Total Column Density Per Sightline . .	62
3.4	Na I ISM Fit Parameters for Targets along the Past Solar Trajectory	63
3.4	Na I ISM Fit Parameters for Targets along the Past Solar Trajectory	64
3.5	Na I ISM Fit Parameters Total Column Density Per Sightline . . .	66
4.1	Cloud Parameters determined from the Sodium Data	89
4.2	Cloud Parameters determined from the Calcium Data	89
4.3	Mean Component Parameters determined from the Sodium Data via the Component-by-Component Method	92
4.4	Summary of Clouds found Via the Component-by-Component Method	95

5.1 Heliosphere Parameters determined from the Sodium Data	102
--	-----

Chapter 1

Introduction

Throughout the last 100 years, researchers have speculated on possible connections between our interstellar environment and Earth's climate. As far back as the 1920's, Harlow Shapley was suggesting the idea of "Cosmic Seasons" (Shapley 1921), the possibility that periodic mass extinctions and drastic climate changes on Earth could be attributed to the Sun's passage through different galactic environments in its orbit around the center of our galaxy. Fred Hoyle considered the possible effect of ISM clouds on climatic variations by postulating that ISM material falling onto the solar surface can change the amount of radiation emitted (Hoyle & Lyttleton 1939).

Such a connection is still of great scientific interest to this day (Bzowski et al. 1996; Shaviv 2003; Gies & Helsel 2005; Frisch & Mueller 2010). One likely effect that a dense interstellar medium cloud could have on Earth's atmosphere is the fluctuation of cosmic ray modulation through the heliosphere which is the "protective bubble" that surrounds the solar system and keeps the cosmic ray flux at Earth relatively low. Such a fluctuation would manifest itself in Earth's geologic record as cosmic ray interactions in the Earth's upper atmosphere create specific isotopes that fall to the surface of the planet to be locked up in ice cores for scientists to later extract and examine. Some unknown features in these geologic records could be due to a passage through a dense interstellar medium cloud.

Table 1.1. Components of the Interstellar Medium

Component	CNM	WNM	HIM
Fractional Volume	1 – 5%	10 – 50%	30 – 70%
Temperature(K)	10 – 100	6,000 – 10,000	$10^6 – 10^7$
Density (cm^{-3})	$10^2 – 10^6$	0.2 – 0.5	$10^{-4} – 10^{-2}$
Scale Height (pc)	~ 70	300 – 1000	1000 – 3000

1.1 The Interstellar Medium

The interstellar medium (ISM) refers to the gas and dust between stars in a galaxy and it is, by terrestrial standards, comprised of extremely low density material (air particle number density at sea level: 10^{19} cm^{-3}). The current model of the ISM in the Milky Way is that all the gas and dust resides in one of three phases: the cold neutral medium (CNM), the warm (partially) ionized medium (WNM/WIM), and the hot ionized medium (HIM). General properties of the three phase model are given in Table 1.1.

Until the late 1970's it was thought that the stable pressure equilibrium state of the galaxy consisted only of two phases: the warm, partially ionized medium, and the cold neutral medium (McKee & Ostriker 1977). The third component, the hot, ionized medium resides in the corona of the galaxy and was only observed recently due to its high degree of ionization (McCray 1987). The warm medium is found nearer to the disk (Heiles & Troland 2003), while the cold neutral medium is found at the lowest scale heights (Dame et al. 1987). Within these pockets of cold, neutral medium are molecular clouds, the birthplace of stars. As we will see, these molecular clouds are dense enough to pose potential hazards to life on Earth should the solar system slip through one in its passage around the center

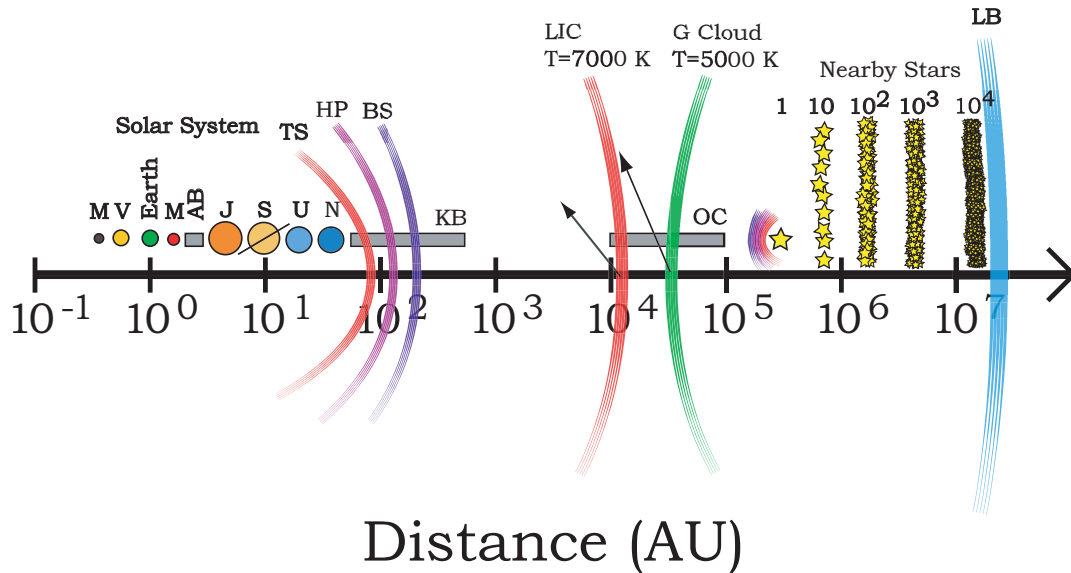


Figure 1.1: The solar system’s neighborhood is depicted here on a logarithmic distance scale extending from less than 1 AU to over 10 million AU. The Sun and its planets reside entirely within the protective bubble of the heliosphere, current estimates to the edge place it in the region of the Kuiper Belt at around 100 AU. Also shown are the edge of the LIC and its associated velocity vector, and the G Cloud with its velocity vector. Our nearest stellar neighbor, α Cen, is seen at a distance of 10^5 AU, also shown are the three components of its astrosphere, analogous to our heliosphere. With increasing distance we begin to encompass more and more of the local stellar population until we reach the edge of the Local Bubble at 10^7 AU.

of the Galaxy.

1.1.1 Our Local Interstellar Environment

Figure 1.1 is a schematic from Redfield (2009), adapted from a similar figure by Liewer et al. (2000). The figure is a logarithmic distance scale of our local galactic environment from the very nearby out to 10^7 AU. Shown are the 8 planets of the solar system as well as the Asteroid Belt, Kuiper Belt and the distant Oort Cloud. Current estimates of the location of the heliosphere boundary place it around 100 AU from the Sun, within the region of the Kuiper Belt. Also shown

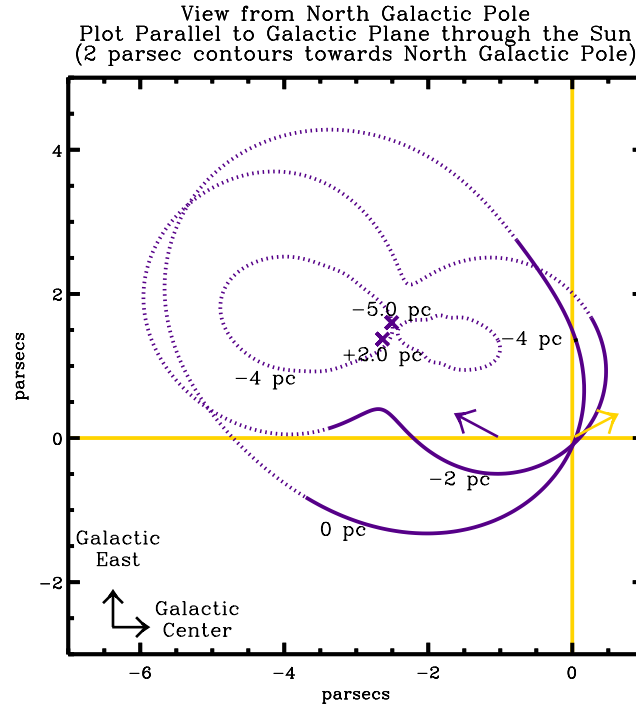


Figure 1.2: A model of the LIC as determined by Redfield & Linsky (2000). The Sun is located at (0,0) and its velocity is indicated with the yellow arrow. The edge of the LIC is shown in purple with well-constrained boundaries denoted by solid lines while the dotted lines indicate where the model is poorly constrained.

at a distance of 10^4 AU is a boundary referred to as the LIC, which stands for Local Interstellar Cloud. Currently the solar system is moving through a large (radius ~ 100 pc), high temperature ($T \sim 10^6$ K), low density ($n(\text{HI}) \sim 5 \text{ cm}^{-3}$) cavity known as the Local Bubble (Redfield 2006). Found throughout this low density cavity, are smaller-scale, slightly higher-density cloudlets referred to as the “local fluff” (Frisch 1995). These cloudlets are usually about 1 to 10 parsecs across and possess particle number densities of $n(\text{HI}) \sim 0.1 \text{ cm}^{-3}$, (Redfield & Linsky 2000) and temperatures of $T \sim 7000\text{K}$, significantly lower than the temperatures of the hot Local Bubble material (Redfield & Linsky 2004).

Figure 1.2 is a three-dimensional model of the LIC determined by Redfield &

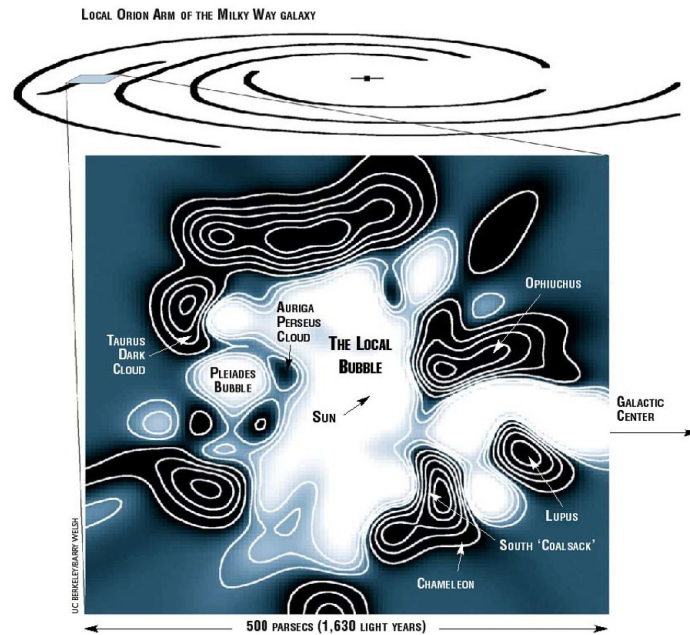


Figure 1.3: The Local Bubble. The hot, rarefied gas found throughout the Local Bubble is mapped in white, and cool, dense gas in black. Contours identify regions of increasing density. Based on a similar figure from Lallement et al. (2003).

Linsky (2000). The Sun is located at (0,0) in the image and is very near to the edge of the LIC. Given their relative velocities (shown by the purple and yellow vectors), the Sun will soon be moving out of the LIC and into hot Local Bubble material in a few thousand years. In fact, some of the furthest Oort Cloud objects might have already crossed this boundary.

Beyond the LIC boundary in Figure 1.1, we see a similar boundary for the Galactic Cloud or G Cloud. The G Cloud is a nearby member of the “local fluff” possessing slightly lower temperatures and higher number densities (Redfield & Linsky 2008). After the Sun exits the LIC, it will spend some time in hot Local Bubble material before it moves into the G Cloud. Moving to greater distances in Figure 1.1, at over 10^5 AU we encounter our nearest stellar neighbor, α Centauri, with its three components of its astrosphere, a feature that is analogous to our

heliosphere. At increasing distances, our volume begins to enclose more and more of the nearby stellar population until we reach the edge of the Local Bubble at around 10^7 AU away.

Figure 1.3 is a map of the Local Bubble in the galactic plane as seen from the north galactic pole, based on a figure from Lallement et al. (2003). The Local Bubble extends roughly 100 parsec from the Sun and was likely carved out by multiple supernova that occurred in within the past 2 to 4 million years. The edge of the Local Bubble is defined by the first detection of cold, high density neutral medium.

1.2 The Heliosphere

In the simplest terms, the heliosphere can be thought of as a bubble being “blown” into the interstellar medium surrounding the Sun, propelled by the solar wind. The solar wind is made up of the constant stream of charged particles emanating from the Sun.

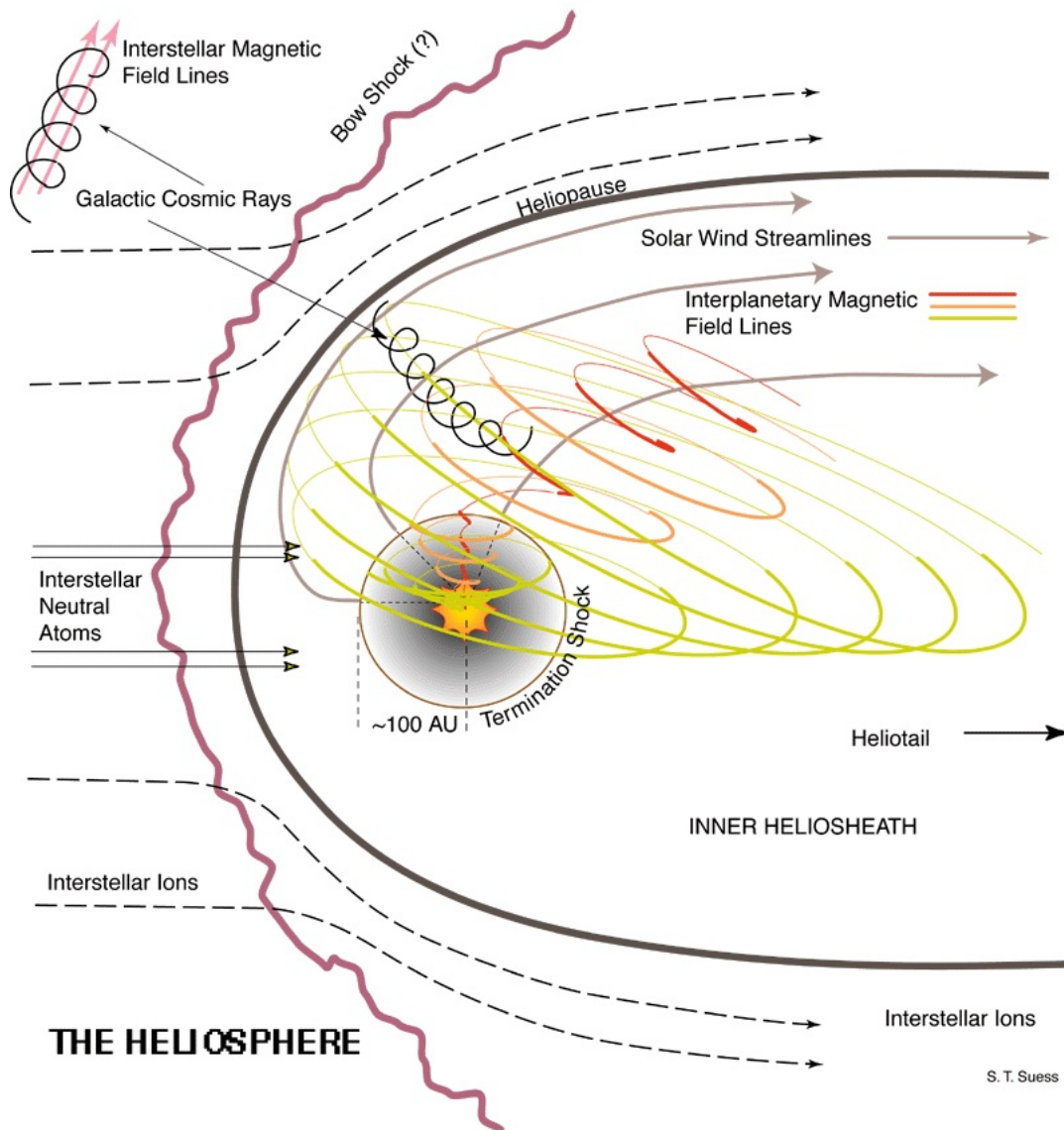
The heliosphere boundary is the location where the momentum of the inward moving ISM flow vector is balanced by the momentum of the outward moving solar wind. The position of this boundary is dictated by the pressure balance of these two flows and is by nature dynamic. Its radial extent is highly dependent on the strength of the solar wind as well as the density and relative velocity of the interstellar medium the solar system happens to be moving through. This boundary can shrink or expand in two ways, through changes in the strength of the solar wind or through variation of the density and velocity of the material surrounding our solar system.

1.2.1 Heliospheric Structure

The heliospheric boundary is comprised of three components: The bow shock, the heliopause, and the termination shock. An interstellar medium cloud encounters an obstacle (the heliosphere) and suffers a drastic reduction in speed to below the speed of sound. This causes a shock to form referred to as the bow shock. Moving outward from the Sun to meet the ISM, the solar wind is also moving at supersonic speeds inside the heliosphere, and also experiences a similar shock at the termination shock. The boundary where the subsonic ISM and heliospheric plasmas meet and flow downstream together is called the heliopause (see Figure 1.4). The stagnation axis is the line drawn from the Sun to the nose of the heliosphere, along this axis the heliosphere will be symmetric.

The region between the heliopause and the termination shock is called the inner heliosheath, and found throughout this volume are the Sun's interplanetary magnetic field lines. These lines propagate outward from the Sun and extend toward the tail-end of the heliosphere in the downwind direction. This magnetic field is the mechanism that diverts low-energy cosmic rays and keep the galactic cosmic ray (GCR) flux at Earth at low values.

Figure 1.5 is model of the heliosphere from Zank & Müller (2003). The top panel is a plot of the temperature distribution of the heliosphere where they have modeled both shocks and the heliopause as well as the ISM and solar wind flow vectors. The bottom panel is the number density distribution of neutral hydrogen. An important structure to make note of here is the region of high neutral hydrogen density directly downwind of the bow shock. This feature is known as the hydrogen wall and is the result of solar wind ions and ISM neutral particles undergoing charge exchange just outside the heliopause. These interactions serve



S. T. Suess

Figure 1.4: A schematic of the components of the heliosphere. The heliosphere is created by the supersonic solar wind meeting and diverting the interstellar plasma flow around the Sun. Depending on the relative velocity of the ISM, it is shocked to subsonic speeds at the bow shock, and the supersonic solar wind also makes a transition to subsonic speeds at the termination shock. The two plasmas meet at the heliopause boundary and turn downwind together toward the heliotail. Found throughout this volume are the interplanetary magnetic field lines generated by the Sun, which divert interstellar ions and low-energy cosmic rays. Image from U. S. Space Studies Board & Committee On Solar Space Physics (2004).

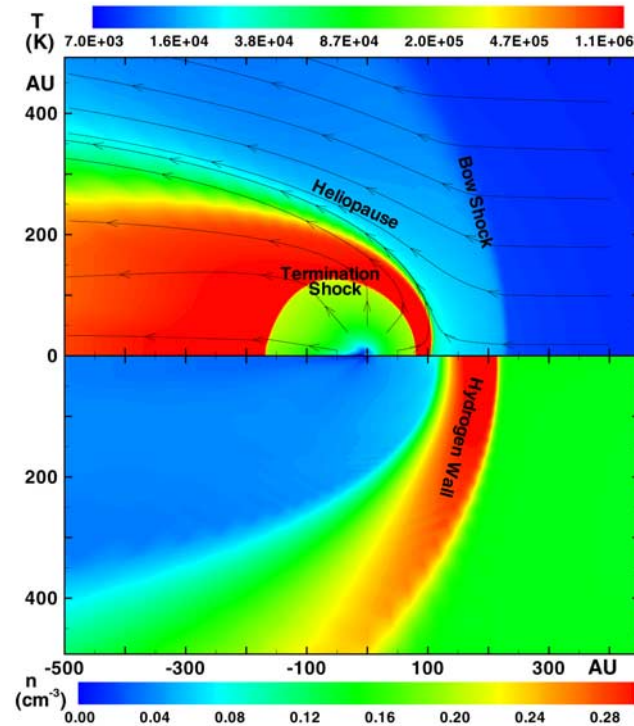


Figure 1.5: A model of the heliosphere from Zank & Müller (2003). The top panel is a plot of temperature and displays the ISM and solar wind flow vectors. The bottom panel is a plot of number density of neutral hydrogen. Both the termination and bow shocks (where the solar wind and ISM respectively are shocked to sub-sonic speeds) are visible, as well as the heliopause, where the two slower-moving plasmas meet and move downwind together. Readily seen in the bottom panel is the hydrogen wall feature just downwind of the bow shock.

to divert and remove momentum from the freshly-made neutral hydrogen which then accumulates within the bow shock.

1.3 Heliospheric Variability

There are a variety of factors that could shift the momentum balance between the solar wind and interstellar medium wind over time, driving overall expansion or contraction of the heliosphere. These factors can either be characterized as internal (changes in the strength of the solar wind due to physical solar processes),

or external (changes in the density of the surrounding ISM or a passing supernova shockwave). Solar variability can cause small, short-lived, fluctuations, changes in the parameters of the circumheliospheric ISM (CISM) can cause strong, long-lasting modulation effects.

1.3.1 Solar Variability

Changes on the solar surface or in the strength of the solar wind drive heliospheric expansion or compression on short timescales. The solar sunspot cycle is the well-documented 11 year variation in the number of sunspots on the solar surface. At the end of this period, the magnetic polarity of the Sun reverses and the cycle begins anew. This 11 year period also sees a variation in the strength of the solar wind, an increase in strength will gently push the heliosphere outwards. Coronal mass ejections and solar flares can cause the heliosphere to expand on even shorter timescales. In fact, it has been known for some time that solar flare activity modulates the cosmic ray flux (Gosling 1964; Markson 1981), and the physical extent of the heliosphere has been measured by spacecraft. In 2003, it was thought that one of the Voyager spacecrafts had crossed the termination shock when its instruments experienced a dramatic increase in charged particle encounters. A few months later, the frequency of charged particle encounters dropped back to levels the spacecraft had experienced throughout its time in the solar system, suggesting that the termination shock had increased in extent and possibly passed over the spacecraft (Decker et al. 2005). After a few additional months, the charged particle encounters increased again. Scientists now believe that the spacecraft is outside the terminator shock for good and might cross the heliopause and enter interstellar space in 2012 (Webber & Intriligator 2011).

1.3.2 Interstellar Variability

The heliosphere can be thought of as a weather balloon released at sea-level and slowly climbing to higher altitudes; the physical size of the balloon will increase as it encounters lower density air in the upper atmosphere. This is similar to how the heliosphere is thought to behave as it moves in and out of ISM environments of varying densities; the physical size of the heliosphere will be greatest in low-density ISM and smallest in high density ISM. The extent of the heliosphere can also be influenced by the speed of the passing cloud. As modeled by Müller et al. (2006), a warm partially ionized, low-density cloud with a high relative cloud-Sun velocity has the potential to compress the heliosphere nearly as much as a slow-moving, cool, high density cloud. The time scales for these types of heliospheric changes will be on the order of thousands of years depending on the size and velocity of the cloud.

The ISM that immediately surrounds the Sun, the LIC, is a warm, low-density, partially ionized cloud. Neutral interstellar particles make it past the magnetic field lines of the heliosphere and move through the solar system with a Sun-ISM velocity of 26 km s^{-1} (Zank & Frisch 1999). While the number density of ISM material inside the heliosphere rises with increasing distance from the Sun, the solar wind prevents most of this material from reaching Earth's orbit. At the distance of Jupiter's orbit, the number densities of ISM and solar wind particles are approximately equal.

Zank & Frisch (1999) have created detailed models investigating the response of the heliosphere as it moves into a dense ISM cloud. Initially they start off the simulation with the density of material around the solar system similar to what it is now. Keeping all other parameters constant, they increase the number

density of ISM neutrals to 10 cm^{-3} , a 50-fold increase from the contemporary value of 0.2 cm^{-3} (Zank & Frisch 1999). This number density is chosen to mimic the encounter of the heliosphere with a dense ISM cloud, similar to one outside the Local Bubble. This increase has a few effects on the heliosphere and the environment inside. First, the number of neutral ISM particles penetrating all the way to 1 AU is no longer zero, but has increased to 2 cm^{-3} . While this might not seem so impressive, the normal particle number density at 1 AU due to the solar wind is roughly 7 cm^{-3} , so this is an appreciable fraction of the normal number density in the immediate vicinity of Earth. Secondly, the size of the heliosphere is drastically reduced in extent from 80–100 AU to 10–14 AU. This will have some effect on the GCR modulation within the heliosphere.

1.4 Cosmic Rays and the Heliosphere

The magnetic field that permeates the heliosphere provides complex life-forms on Earth with a necessary shield from cosmic-rays. Galactic cosmic-rays (GCRs) are highly energetic charged particles that zip through the galaxy at considerable fractions of the speed of light. GCRs are thought to be produced in supernova, but even the high power of these events is unable to accelerate some of the high energy GCRs. It's possible that the particles spend some time moving between the expanding magnetic field lines of these supernova, gaining energy each time until they obtain enough kinetic energy to break free. The ambient magnetic fields found throughout the galaxy serve to diffuse and scatter these particles from their original direction, thus it becomes very difficult to trace a GCR's trajectory back to its origin.

The inner component of the heliosphere contains the strong solar magnetic

field that is capable of diverting most of these harmful particles away from Earth, since charged particles are diverted by magnetic fields. However, removal of this shield through a reduction of the size of the heliosphere could result in an increase in the GCR flux at the distance of Earth's orbit from the Sun. Aside from the heliosphere, Earth also has two other means of cosmic-ray screening: the sheer bulk of the Earth's atmosphere and the Earth's magnetic field. Above every centimeter of Earth's surface lies roughly one kilometer of air. It takes a vertical column of about 70 grams - about $\frac{1}{14}$ of the distance through the atmosphere before the average incoming proton hits the nucleus of an air atom (Parker 2006). This collision results in a shower of secondary and tertiary particles (see Figure 1.6) that propagate down through the atmosphere at decreasing energies and are found all the way to the ground and below.

With these three shields in place, the cosmic ray exposure at the surface of the planet is not extreme. The annual radiation exposure due to cosmic rays is equivalent to around 0.03 rem, and it is about as much as one would receive from two chest X-rays. An average U.S. inhabitant receives a total of 0.36 rems per year due to natural and man-made sources of radiation (Aroesty et al. 1991).

1.4.1 Cosmic Ray Consequences

Among the many results of a cosmic-ray shower are a high number density of electrons produced near the shower axis (Erlykin & Wolfendale 2010). These electrons could play a role in the initiation of lightning strikes. Lightning has possibly had an affect on the evolutionary history or even the origin of life. The famous experiments of Miller and Urey (Miller 1953) found that the passage of electricity through a pre-biotic soup of methane, ammonia and water caused com-

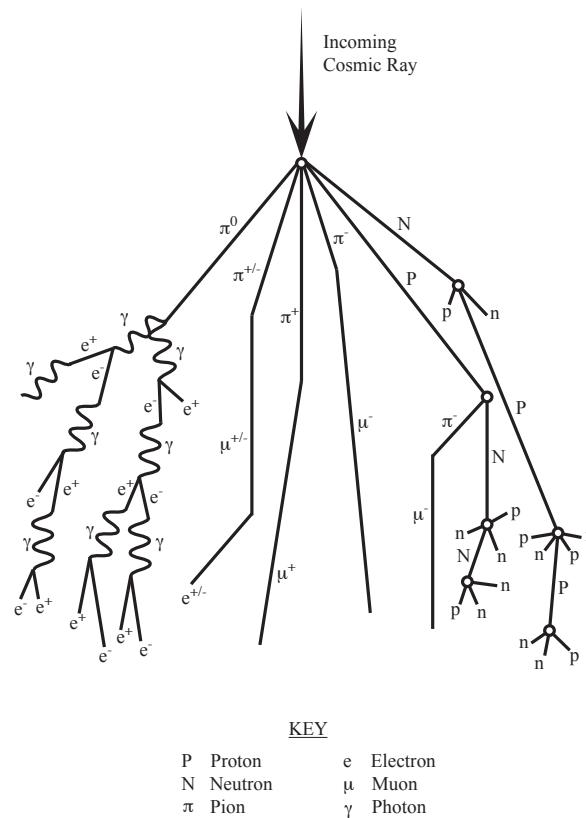


Figure 1.6: When an incoming cosmic ray particle collides with an air molecule it produces a cascade of lighter particles that go on to create a number of isotopes of varying half-lives that are found all the way to the ground and below.

plex molecules to form: amino acids, monomers, RNA, etc. All of these complex molecules are necessary precursors to life, and thus lightning from cosmic rays could have been part of the formation of life on Earth.

Later, when life had developed, lightning strikes could have played a further role in its continuing evolution. NO and NO₂ are formed by lightning strikes, and make up 20% of all NO_x (Allen et al. 2010). The formation of NO_x can modify Earth's atmospheric chemistry by increasing greenhouse gasses. Although damaging to animals, NO_x is beneficial to plants by way of the nitrates produced by NO_x reactions, so periods of high GCR radiation in the geologic record would

be as interesting as low ones.

Other potential consequences of increased CISM density are cloud nucleation and dust deposition. The high numbers of ions produced in a cosmic ray particle shower can also trigger cloud formation in Earth's lower atmosphere which could lead to an increase in planetary albedo (Carslaw et al. 2002) lowering global temperatures. The Sun's passage through a particularly dense ISM cloud could also lead to an increase in the number of ISM neutral particles at Earth's orbit. An increase of interstellar dust in Earth's upper atmosphere has been modeled by Pavlov et al. (2005) to produce a reverse greenhouse effect, also lowering global temperatures.

1.4.2 Comparison with the Geologic Record

Evidence of a solar encounter with dense molecular cloud could be reflected in our geologic record. Cosmic ray spallation reactions in Earth's stratosphere create the cosmogenic nuclide ^{10}Be which is then deposited on the surface of the Earth and secured in ice-cores. Periods of high cosmic ray flux will correspond to higher levels of ^{10}Be . A long archive of ^{10}Be data exists from an analysis of deposits in Greenland ice-cores, which also show the 11 year solar cycle modulation of cosmic rays.

Periods of low-solar activity such as the Maunder (1645-1715) and Dalton (1800-1830) minima have been shown to have strong associations with times of high GCR intensities as revealed by the ^{10}Be record (McCracken et al. 2004). However there are plenty of features in Earth's isotope record that are unaccounted for. Figure 1.7 shows Earth's record of ^{18}O and ^{13}C isotopes as determined from ice-cores that sample global conditions as long as 60 million years ago. Some

features have been identified and correspond to periods of glaciation. Some of the broader declines in global temperatures, such as the decline found after the Eocene Climatic Optimum, could possibly be due to a passage through a dense ISM cloud.

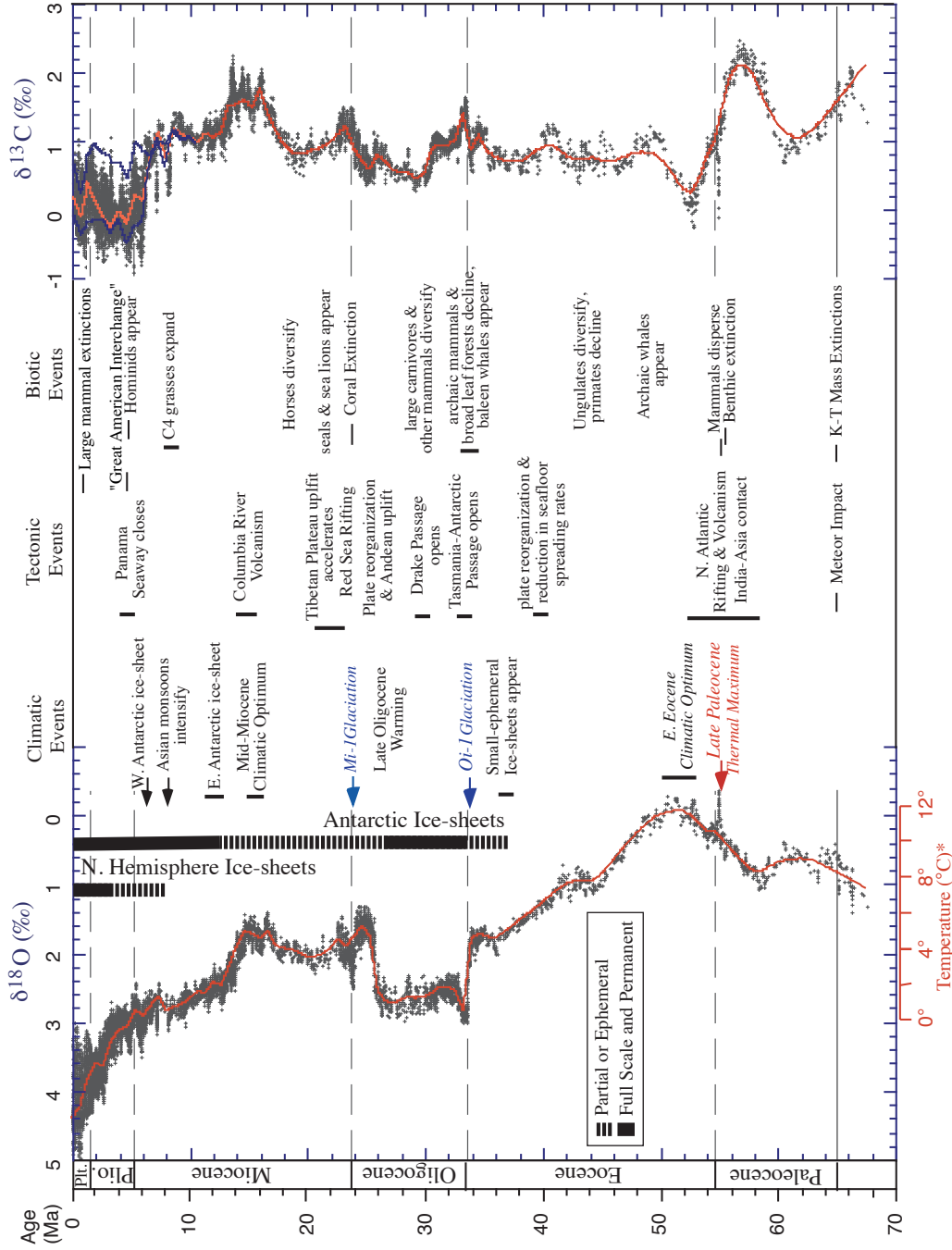


Figure 1.7: A historical record of atmospheric isotopes ^{18}O and ^{13}C . ^{18}O is a proxy for global temperatures. Many of the causes for sharp changes in isotope abundance with time have been identified, the long gradual slopes might be due to our passage through a dense ISM cloud. From Zachos et al. (2001)

This Work

Chapter 2 of this document will present observations made of the ISM that the Sun has passed through over the past 40 million years. Chapter 3 will detail how information is extracted from these observations and will discuss the data set as a whole. Chapter 4 will present the various methods used to determine volume densities of these ISM clouds and Chapter 5 will explore what these clouds mean for our historical heliosphere.

Chapter 2

Observations and Data Reduction

The ISM outside the Local Bubble is much denser and cooler than the gas we find in the immediate vicinity of the Sun. Neutral sodium (NaI) and singly ionized calcium (CaII) were chosen as the ISM component tracers since they both have strong doublet transition lines that can be observed in the temperature ranges we expect these clouds to possess. These lines are among the strongest absorption features in the Sun and were given letter designations in the 1800's by Joseph von Fraunhofer. The calcium lines, at 3933.6614 \AA and 3968.4673 \AA were named K and H respectively, and the sodium lines, due to their 5 \AA separation, were too closely spaced to resolve into two lines at the time. Consequently the two lines were assumed to be one and were given the designation D. Later with higher resolution they were resolved into their true, dual-lined nature and named D1 and D2, residing at 5895.9242 \AA and 5889.9510 \AA respectively.

As instruments capable of resolving finer structures were developed, it was discovered that each line in the sodium doublet is actually comprised of two finer closely-spaced lines referred to as the hyper-fine structure of sodium. The fine doublet (D1 and D2) arises as a result of the coupling between the electron's orbital angular momentum and its spin angular momentum. The hyper-fine structure is a result of this total electron angular momentum coupled with the nuclear angular momentum, each coupling results in a splitting of the absorption line.

The absorption lines of NaI and CaII are among the strongest optical resonance lines found in the ISM. A resonance line is the longest wavelength transition arising from the ground state of a particular atom or ion. The ionization potentials for NaI and CaII are 5.139 eV and 6.113 eV (Gray 2005), respectively, so sodium ionizes at a lower temperature than calcium. This means that the two species probe slightly different ISM environments.

Observations of doublet transitions are valuable since each half of a doublet serves as an independent measurement of the same absorbing medium. Each line measures cloud temperature, radial and turbulent velocity, as well as column density. Combining the values from independently fitting each line together allows us to get a more accurate value for each measurement than if we were observing only one line.

Stars were observed for ISM absorption out to a distance of 500 parsecs, which given current values for the velocity of the Sun (Schönrich et al. 2010), corresponds to about 40 million years (Myr) of our history. A distance of 500 parsecs is only about 1% of the circumference of the solar orbit at 8 kiloparsecs from the galactic center, so we can approximate the Sun's trajectory over the past 40 Myr as a straight line from the direction of past solar motion, $l_0 = 207.70^\circ$ and $b_0 = -32.41^\circ$ (Dehnen & Binney 1998). Stars were chosen based on their small angular separation from these coordinates. Figure 2.1 is a map of our sample location. l_0 and b_0 lie at the center of the pink circle and the entirety of our stellar sample also lies within this region with a diameter of about 20° .

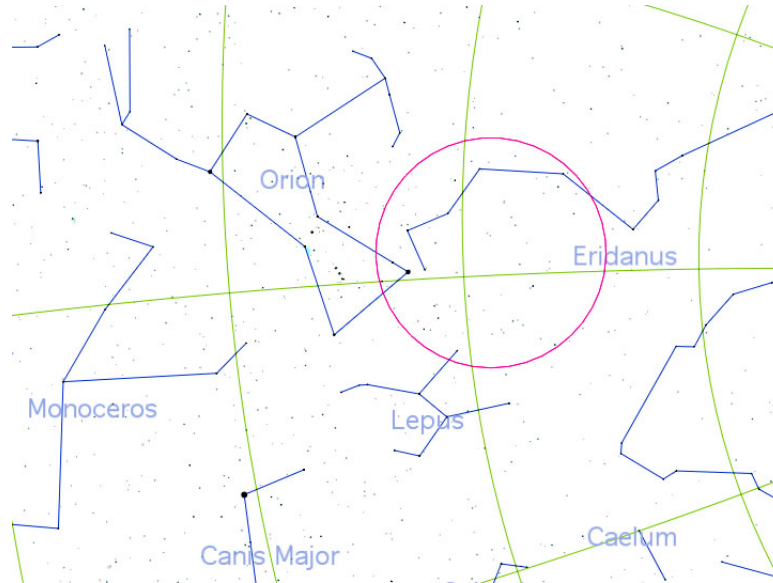


Figure 2.1: The direction of solar past motion is centered at $l_0 = 207.70^\circ$ and $b_0 = -32.41^\circ$, which is located in the center of the pink circle in this figure. The angular diameter of the region encompassing the entire stellar sample used in this thesis is about 20° .

2.1 Stellar Parameters

When looking at ISM absorption towards a background star, invariably you are also looking at stellar absorption features in the same wavelength range due to elements residing in the star itself. For this reason, stars of spectral type F or earlier were chosen for their relatively simple spectra with few absorption features. This helps to minimize any confusion between calcium or sodium stellar absorption and ISM absorption. Early type stars are also intrinsically brighter, allowing for higher S/R in our observations, and come with the added benefit that their surface temperatures are much too hot for neutral sodium and singly ionized calcium to exist in great quantities which further eliminates the chance of confusion between stellar and ISM absorption. A strong stellar absorption feature would easily overwhelm any additional absorption due to ISM. Rapidly rotating

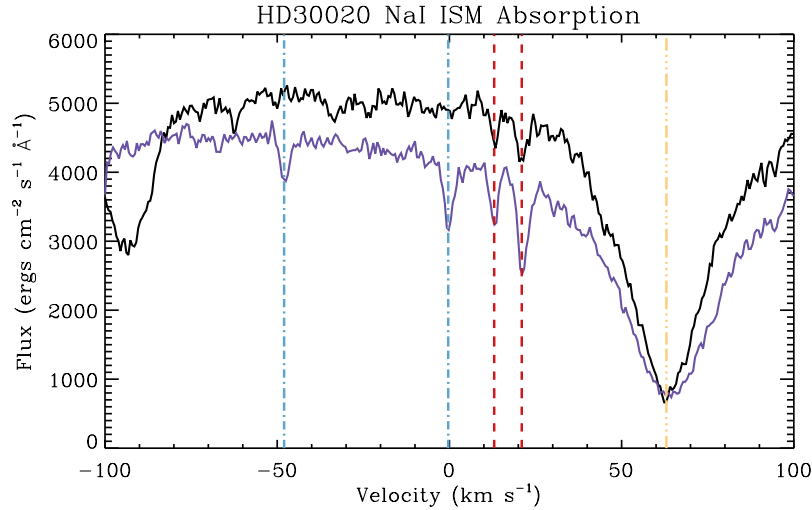


Figure 2.2: Sample spectra of neutral sodium absorption towards HD30020. Both the D1 and D2 components of the sodium doublet are plotted in velocity space to distinguish sodium absorption from non-sodium absorption. Telluric contamination due to water in Earth’s atmosphere is marked by two blue lines, the stellar sodium absorption is marked by a single yellow line and two ISM components are marked by red lines.

stars were also preferable, since stars with high rotational velocities have broadened stellar absorption features that are more easily distinguished from narrow ISM absorption components.

Figure 2.2 is an example of spectral data that illustrates the difference between stellar sodium absorption and ISM sodium absorption. For ease of identification, the wavelength scale has been translated into a velocity scale and the D1 range has been plotted over the D2 range. This allows the doublet absorption to become immediately apparent as both lines of the doublet have to be moving at the same radial velocity. The broad feature at 65 km s^{-1} can be identified as stellar absorption since the rotational and thermal broadening required for such a wide sodium line are much too high to be found in ISM. There are two ISM absorption features found in this figure, located at roughly 12 and 21 km s^{-1} . These features can be identified as being caused by the ISM since they are narrow and seen in

both D1 and D2. Other features which have no absorption in both spectra are most likely telluric absorption due to water vapor in Earth's atmosphere and are removed before ISM absorption measurements are made.

Table 2.1 lists relevant parameters for stars used in this study. Listed for each star are its Henry Draper catalogue number and an additional common name, stellar spectral type as well as apparent magnitude (m_V), its line of sight or radial velocity (v_R), and its rotational velocity subject to viewing angle i ($v \sin i$). Galactic longitude and latitude (l, b) are also listed and distances as determined from *Hipparcos* parallaxes. Finally each sight line's angular separation in degrees ($\Delta\theta$) from direction of the past solar trajectory, l_0, b_0 is also included in the table.

2.2 Observations

Data were obtained throughout the time period of October 2003 through October 2005. Additional data on a few objects were obtained in August 2010 but are not included in this study. Observations were made with two different telescopes at a variety of different resolutions. Targets were often observed multiple times at different resolutions to provide consistency checks on measurements of cloud parameters.

2.2.1 Telescopes

Harlan J. Smith

The Harlan J. Smith telescope is a 2.7 meter optical reflecting telescope located at McDonald Observatory in west Texas. Observations were made at three separate resolution ($R = \frac{\lambda}{\Delta\lambda}$) settings: CS12: coude Spectrometer ($R \sim 500,000$),

Table 2.1. Stellar Parameters for Targets along the Past Solar Trajectory^a

HD #	Other Name	Spectral Type	m_V (mag)	v_R (km s ⁻¹)	$v \sin i$ (km s ⁻¹)	l (°)	b (°)	Distance ^b (pc)	$\Delta\theta^c$ (°)
33111	β Eri	A3III	2.8	-9.2	195	205.34	-25.32	27.24 ^{+0.58} _{-0.55}	7.38
30743	HR1545	F5V	6.3	-3.0	7.0 ^d	212.08	-33.12	35.36 ^{+1.03} _{-0.97}	3.75
26574	σ^1 Eri	F2II-III	4.0	11.0	115	199.32	-38.39	38.5 ^{+1.6} _{-1.5}	9.07
33904	μ Lep	B9IV	3.3	27.7	18	217.25	-28.91	56.5 ^{+2.4} _{-2.2}	8.92
27861	ξ Eri	A2V	5.2	-11.0	179	197.82	-34.30	63.9 ^{+3.4} _{-3.1}	8.46
31109	ω Eri	A9IV	4.4	-6.0	186	203.75	-28.78	69.5 ^{+4.5} _{-4.0}	4.97
29573	HR1483	A0V	5.0	6.5	27	208.96	-34.85	69.7 ^{+4.0} _{-3.6}	2.66
33802	ι Lep	B8V	4.5	25.0	190	212.67	-27.32	73.9 ^{+4.0} _{-3.6}	6.67
32964	EN Eri	B9V	5.1	30.9	30	204.78	-25.35	85.8 ^{+5.7} _{-5.1}	7.51
32045	S Eri	F0V	4.8	-8.9	212	211.94	-30.34	89.2 ^{+6.3} _{-5.5}	4.17
30127	HR1513	A1V	5.5	5.0	195	216.99	-36.20	90.4 ^{+6.9} _{-6.0}	8.55
34863	ν Lep	B7V	5.3	16.0	285	214.00	-25.79	101.7 ^{+9.0} _{-7.7}	8.61
27925	HIP20521	A9IV/V	8.0			209.24	-38.96	103 ⁺¹³ ₋₁₁	6.67
32996	HR1661	B9.5/A0IV	6.0	25.8 ^e	26	213.32	-29.10	111.4 ^{+9.9} _{-8.4}	5.85
29173	HR1460	A1	6.4	15 ^f	26	205.87	-34.63	119 ⁺⁴⁶ ₋₂₆	2.69
28763	HR1438	A3V	6.3	-11.9 ^e	102	209.75	-37.13	123 ⁺¹⁵ ₋₁₂	5.01
30020	DW Eri	F4III	6.8	40.0	65	205.96	-32.37	124 ⁺²⁶ ₋₁₈	1.47
28843	DZ Eri	B9III	5.8	18.4		198.62	-32.10	131 ⁺¹⁶ ₋₁₃	7.68
29554	HIP21640	B9	7.7			204.73	-33.15	135 ⁺²¹ ₋₁₆	2.60
32468	HIP23493	A0	6.8			208.30	-28.00	151 ⁺³¹ ₋₂₂	4.44
28208	HIP20747	B9	7.3			201.61	-35.18	153 ⁺²⁵ ₋₁₉	5.77
31625	HIP23011	A5	6.9	27.7	77	207.34	-29.25	158 ⁺²⁴ ₋₁₈	3.18
29851	HIP21837	A2IV/V	6.7			209.70	-34.37	161 ⁺²⁴ ₋₁₉	2.57
30211	μ Eri	B5IV	4.0	8.5	150	200.53	-29.34	163 ⁺³³ ₋₂₃	6.87
34503	τ Ori	B5III	3.6	20.1	40	208.28	-23.96	170 ⁺²⁶ ₋₂₀	8.47
33949	κ Lep	B7V	4.4	18.0	120	213.88	-27.55	172 ⁺²³ ₋₁₈	7.23
28980	HIP21258	A0	6.6			204.05	-34.31	172 ⁺²⁶ ₋₂₀	3.59
29248	ν Eri	B2III	3.9	14.9	20	199.31	-31.38	180 ⁺³⁴ ₋₂₅	7.20
30050	RZ Eri	A	7.9	32.0	11 ^g	208.00	-33.16	185 ⁺⁵⁸ ₋₃₆	0.79
28377	HIP20849	A9IV	7.5			207.45	-37.20	210 ⁺⁵⁰ ₋₃₄	4.79
30535	HIP22304	A0	7.2			207.32	-31.65	224 ⁺⁴⁹ ₋₃₄	0.83
31512	62 Eri	B6V	5.5	24.0	80	203.93	-27.88	227 ⁺⁹⁴ ₋₅₁	5.58
27563	EM Eri	B5III	5.8	11.2	35	201.50	-36.83	232 ⁺⁴⁹ ₋₃₄	6.75
33224	HR1671	B8V	5.8	27.0	155	208.95	-26.83	233 ⁺⁶³ ₋₄₁	5.68
31089	HIP22669	B9V	7.8			208.90	-31.12	233 ⁺⁶⁵ ₋₄₂	1.64
34085	β Ori	B8I	0.1	20.7	40	209.24	-25.25	237 ⁺⁵⁶ ₋₃₈	7.29
29009	EH Eri	B9	5.7	1.7	55	202.47	-33.55	239 ⁺⁶⁴ ₋₄₂	4.53
28262	HIP20787	A0	8.6			203.85	-36.03	275 ⁺¹¹⁷ ₋₆₃	4.82
32249	ψ Eri	B3V	4.8	25.4	30	206.59	-27.69	293 ⁺⁹³ ₋₅₇	4.82
31726	HR1595	B2V	6.1	11.4	5	213.50	-31.51	305 ⁺⁸⁷ ₋₅₆	5.00
30332	HIP22169	B9	7.7			209.25	-33.00	305 ⁺¹¹⁷ ₋₆₆	1.43
34816	λ Lep	B0.5IV	4.3	20.2	25	214.83	-26.24	330 ⁺¹¹² ₋₆₇	8.75
26994	HIP19856	B7III	6.9			211.14	-41.78	375 ⁺¹⁷⁸ ₋₉₁	9.76
32612	HR1640	B2IV	6.4	16.0	65	214.33	-30.21	405 ⁺¹⁶⁷ ₋₉₁	6.08
30679	HIP22406	A2	7.7			206.93	-31.19	410 ⁺²⁰⁰ ₋₁₀₀	1.38
30076	DX Eri	B2V	5.8	15.1	160	205.72	-32.12	410 ⁺²¹⁰ ₋₁₀₀	1.70
30963	HIP22588	B9	7.3			208.57	-31.24	420 ⁺²²⁰ ₋₁₁₀	1.38
27436	HIP20179	A0	7.0			201.90	-37.34	470 ⁺³⁷⁰ ₋₁₄₀	6.85
28497	DU Eri	B2V	5.6	22.0	295	208.78	-37.40	480 ⁺³²⁰ ₋₁₄₀	5.07

^aAll values from SIMBAD unless otherwise noted.^bDistances calculated from *Hipparcos* parallaxes.^cAngular distance from direction of the past solar trajectory, $l = 207.70^\circ$ and $b = -32.41^\circ$ (Dehnen & Binney 1998).^dNordström et al. (2004)^eGrenier et al. (1999)^fShorlin et al. (2002)^gStawikowski & Glebocki (1994)

CS21: Cross-Dispersed Echelle Spectrometer (2d coudé) focus 1 ($R \sim 240,000$), and CS23: Cross-Dispersed Echelle Spectrometer (2d coudé) focus 2 ($R \sim 60,000$).

Anglo-Australian Telescope

The Anglo-Australian 3.9 meter telescope is located at the Siding Spring Observatory in Australia. Data were taken with the Ultra High Resolution Facility which is an echelle spectrograph located at the coudé focus ($R \sim 1,000,000$)

2.2.2 Observational Parameters

Tables 2.2 and 2.3 list the observational parameters for all data included in this study. Table 2.2 is ordered by date and 2.3 is ordered by distance from Earth. Each observation lists the date the data was obtained, the telescope and instrument used, what ion was observed, the length of the exposure, and approximate S/N for the observation. Table 2.3 also lists the velocity of Earth's atmosphere at the time of the observation for the sodium data. The region of the spectrum that contains sodium absorption also suffers from high amounts of telluric contamination which can be modeled out, but not without information about the velocity of the atmosphere relative to the data.

Table 2.2. Observational Parameters for Stars along the Past Solar Trajectory

HD #	Other Name	Date	Telescope ^a	Instrument ^b	Ion	Exposure (s)	S/N
29573	HR1483	2003 Oct 2	McD2.7	CS12	CaII	3600	4
33904	μ Lep	2003 Oct 5	McD2.7	CS12	CaII	3600	17
29248	ν Eri	2003 Dec 1	McD2.7	CS12	CaII	3600	36
34085	β Ori	2003 Dec 1	McD2.7	CS12	CaII	2400	119
30076	DX Eri	2003 Dec 1	McD2.7	CS12	CaII	7200	8
32249	ψ Eri	2003 Dec 1	McD2.7	CS12	CaII	4800	19
34816	λ Lep	2003 Dec 1	McD2.7	CS12	CaII	4800	16
29248	ν Eri	2003 Dec 2	McD2.7	CS12	NaI	3600	25
34085	β Ori	2003 Dec 2	McD2.7	CS12	NaI	2400	143
30076	DX Eri	2003 Dec 2	McD2.7	CS12	NaI	3600	6
32249	ψ Eri	2003 Dec 2	McD2.7	CS12	NaI	4800	19
34816	λ Lep	2003 Dec 2	McD2.7	CS12	NaI	4800	25
33904	μ Lep	2003 Dec 2	McD2.7	CS12	NaI	3600	30
33111	β Eri	2003 Dec 3	McD2.7	CS12	CaII	4800	27
34503	τ Ori	2003 Dec 3	McD2.7	CS12	CaII	4800	38
30211	μ Eri	2003 Dec 3	McD2.7	CS12	CaII	3600	18
30211	μ Eri	2004 Oct 18	McD2.7	CS21	NaI	1200	131
30211	μ Eri	2004 Oct 18	McD2.7	CS21	CaII	600	41
33904	μ Lep	2004 Oct 19	McD2.7	CS21	CaII	1200	117
28497	DU Eri	2004 Oct 19	McD2.7	CS21	CaII	1200	52
28497	DU Eri	2004 Oct 19	McD2.7	CS21	NaI	1200	98
34503	τ Ori	2004 Oct 19	McD2.7	CS21	NaI	1200	265
33111	β Eri	2004 Oct 19	McD2.7	CS21	NaI	1200	385
28763	HR1438	2004 Oct 20	McD2.7	CS21	CaII	1800	24
28763	HR1438	2004 Oct 20	McD2.7	CS21	NaI	1800	78
29573	HR1483	2004 Oct 20	McD2.7	CS21	NaI	1200	114
29573	HR1483	2004 Oct 20	McD2.7	CS21	CaII	1200	42
30127	HR1513	2004 Oct 20	McD2.7	CS21	CaII	1800	37
30127	HR1513	2004 Oct 20	McD2.7	CS21	NaI	1800	109
30020	DW Eri	2004 Oct 20	McD2.7	CS21	NaI	1200	57
30020	DW Eri	2004 Oct 20	McD2.7	CS21	CaII	1800	14
32045	S Eri	2004 Oct 20	McD2.7	CS21	CaII	1200	54
32045	S Eri	2004 Oct 20	McD2.7	CS21	NaI	600	86
30076	DX Eri	2004 Nov 30	McD2.7	CS23	CaII, NaI	900	101, 300
30332	HIP22169	2004 Nov 30	McD2.7	CS23	CaII, NaI	600	0, 3
30963	HIP22588	2004 Nov 30	McD2.7	CS23	CaII, NaI	1800	66, 241
29554	HIP21640	2004 Nov 30	McD2.7	CS23	CaII, NaI	1800	60, 206
32249	ψ Eri	2004 Nov 30	McD2.7	CS23	CaII, NaI	900	164, 398
28497	DU Eri	2004 Nov 30	McD2.7	CS23	CaII, NaI	900	70, 228
30211	μ Eri	2004 Nov 30	McD2.7	CS23	CaII, NaI	900	184, 522
31512	62 Eri	2004 Nov 30	McD2.7	CS23	CaII, NaI	900	71, 240
33224	HR1671	2004 Nov 30	McD2.7	CS23	CaII, NaI	900	38, 186
30332	HIP22169	2004 Dec 1	McD2.7	CS23	CaII, NaI	1800	40, 136
31089	HIP22669	2004 Dec 1	McD2.7	CS23	CaII, NaI	1800	41, 143
31726	HR1595	2004 Dec 1	McD2.7	CS23	CaII, NaI	1800	122, 301
30050	RZ Eri	2004 Dec 1	McD2.7	CS23	CaII, NaI	1800	16, 156
27563	EM Eri	2004 Dec 1	McD2.7	CS23	CaII, NaI	900	74, 273
29009	EH Eri	2004 Dec 1	McD2.7	CS23	CaII, NaI	900	71, 275
30535	HIP22304	2004 Dec 1	McD2.7	CS23	CaII, NaI	1800	29, 178
31109	ω Eri	2004 Dec 1	McD2.7	CS23	CaII, NaI	900	23, 438
33111	β Eri	2004 Dec 1	McD2.7	CS23	CaII, NaI	300	52, 465
32964	EN Eri	2004 Dec 1	McD2.7	CS23	CaII, NaI	900	29, 248
34085	β Ori	2004 Dec 2	McD2.7	CS23	CaII, NaI	10	105, 431
30679	HIP22406	2004 Dec 2	McD2.7	CS23	CaII, NaI	1800	17, 190

Table 2.2 (cont'd)

HD #	Other Name	Date	Telescope ^a	Instrument ^b	Ion	Exposure (s)	S/N
32612	HR1640	2004 Dec 2	McD2.7	CS23	CaII, NaI	1800	86, 284
29851	HIP21837	2004 Dec 2	McD2.7	CS23	CaII, NaI	1800	45, 238
32996	HR1661	2004 Dec 2	McD2.7	CS23	CaII, NaI	1800	92, 315
29173	HR1460	2004 Dec 2	McD2.7	CS23	CaII, NaI	1800	46, 193
28980	HIP21258	2004 Dec 2	McD2.7	CS23	CaII, NaI	1800	46, 181
30020	DW Eri	2004 Dec 2	McD2.7	CS23	CaII, NaI	900	0, 96
26574	ϕ^1 Eri	2004 Dec 3	McD2.7	CS23	CaII, NaI	3600	0, 8
33949	κ Lep	2004 Dec 3	McD2.7	CS23	CaII, NaI	1800	0, 7
26574	ϕ^1 Eri	2004 Dec 6	McD2.7	CS23	CaII, NaI	900	46, 442
26994	HIP19856	2004 Dec 6	McD2.7	CS23	CaII, NaI	1800	46, 142
27925	HIP20521	2004 Dec 6	McD2.7	CS23	CaII, NaI	1800	6, 83
28377	HIP20849	2004 Dec 6	McD2.7	CS23	CaII, NaI	1800	8, 101
27436	HIP20179	2004 Dec 6	McD2.7	CS23	CaII, NaI	1800	15, 102
28262	HIP20787	2004 Dec 6	McD2.7	CS23	CaII, NaI	2700	9, 65
28208	HIP20747	2004 Dec 6	McD2.7	CS23	CaII, NaI	1800	15, 96
31625	HIP23011	2004 Dec 6	McD2.7	CS23	CaII, NaI	1800	4, 113
33802	ι Lep	2005 Jan 28	McD2.7	CS12	CaII	4800	15
30743	HR1545	2005 Feb 14	McD2.7	CS21	NaI	1200	46
30743	HR1545	2005 Feb 14	McD2.7	CS21	CaII	2400	13
32468	HIP23493	2005 Feb 14	McD2.7	CS21	CaII	1800	21
32468	HIP23493	2005 Feb 14	McD2.7	CS21	NaI	1200	28
33802	ι Lep	2005 Feb 14	McD2.7	CS21	NaI	1200	108
33802	ι Lep	2005 Feb 14	McD2.7	CS21	CaII	1200	72
33949	κ Lep	2005 Feb 14	McD2.7	CS21	CaII	1200	68
33949	κ Lep	2005 Feb 14	McD2.7	CS21	NaI	1200	93
34085	β Ori	2005 Feb 27	AAT3.9	UHRF	NaI	900	316
33111	β Eri	2005 Feb 27	AAT3.9	UHRF	NaI	1200	82
33949	κ Lep	2005 Feb 27	AAT3.9	UHRF	NaI	2400	30
34085	β Ori	2005 Feb 28	AAT3.9	UHRF	CaII	900	246
33111	β Eri	2005 Feb 28	AAT3.9	UHRF	CaII	1200	42
33949	κ Lep	2005 Feb 28	AAT3.9	UHRF	CaII	1800	37
33802	ι Lep	2005 Feb 28	AAT3.9	UHRF	CaII	1800	37
28843	DZ Eri	2005 Mar 14	McD2.7	CS21	CaII	2700	36
28843	DZ Eri	2005 Mar 14	McD2.7	CS21	NaI	1800	32
34863	ν Lep	2005 Mar 16	McD2.7	CS21	NaI	1200	56
34863	ν Lep	2005 Mar 16	McD2.7	CS21	CaII	1800	47
27861	ξ Eri	2005 Mar 16	McD2.7	CS21	CaII	1800	49
27861	ξ Eri	2005 Mar 16	McD2.7	CS21	NaI	1200	72
34085	β Ori	2005 Mar 22	McD2.7	CS12	CaII	2400	129
33904	μ Lep	2005 Oct 17	AAT3.9	UHRF	CaII	2400	50

^aMcD2.7: the Harlan J. Smith 2.7m Telescope at McDonald Observatory; AAT3.9: the Anglo-Australian 3.9m Telescope at the Anglo-Australian Observatory.

^bCS12: Coudé double-pass Spectrometer ($R \sim 500,000$); CS21: Cross-Dispersed Echelle Spectrometer (2D Coudé) Focus 1 ($R \sim 240,000$); CS23: Cross-Dispersed Echelle Spectrometer (2D Coudé) Focus 3 ($R \sim 60,000$); UHRF: Ultra High Resolution Facility ($R \sim 1,000,000$).

Table 2.3. Observational Parameters for Stars along the Past Solar Trajectory

HD #	Other Name	Date	Telescope ^a	Instrument ^b	Ion	v_{atm} km s ⁻¹	Exposure (s)	S/N
33111	β Eri	2003 Dec 3	McD2.7	CS12	CaII		4800	27
33111	β Eri	2004 Oct 19	McD2.7	CS21	NaI	+21.2	1200	385
33111	β Eri	2004 Dec 1	McD2.7	CS23	CaII, NaI	+2.7	300	52, 465
33111	β Eri	2005 Feb 27	AAT3.9	UHRF	NaI	-29.7	1200	82
33111	β Eri	2005 Feb 28	AAT3.9	UHRF	CaII		1200	42
30743	HR1545	2005 Feb 14	McD2.7	CS21	NaI	-28.5	1200	46
30743	HR1545	2005 Feb 14	McD2.7	CS21	CaII		2400	13
26574	σ^1 Eri	2004 Dec 3	McD2.7	CS23	CaII, NaI	-5.4	3600	0, 8
26574	σ^1 Eri	2004 Dec 6	McD2.7	CS23	CaII, NaI	-6.8	900	46, 442
33904	μ Lep	2003 Oct 5	McD2.7	CS12	CaII		3600	17
33904	μ Lep	2003 Dec 2	McD2.7	CS12	NaI	+3.9	3600	30
33904	μ Lep	2004 Oct 19	McD2.7	CS21	CaII		1200	117
33904	μ Lep	2005 Oct 17	AAT3.9	UHRF	CaII		2400	50
27861	ξ Eri	2005 Mar 16	McD2.7	CS21	CaII		1800	49
27861	ξ Eri	2005 Mar 16	McD2.7	CS21	NaI	-26.6	1200	72
31109	ω Eri	2004 Dec 1	McD2.7	CS23	CaII, NaI	+0.7	900	23, 438
29573	HR1483	2003 Oct 2	McD2.7	CS12	CaII		3600	4
29573	HR1483	2004 Oct 20	McD2.7	CS21	NaI	+19.2	1200	114
29573	HR1483	2004 Oct 20	McD2.7	CS21	CaII		1200	42
33802	ι Lep	2005 Jan 28	McD2.7	CS12	CaII		4800	15
33802	ι Lep	2005 Feb 14	McD2.7	CS21	NaI	-27.4	1200	108
33802	ι Lep	2005 Feb 14	McD2.7	CS21	CaII		1200	72
33802	ι Lep	2005 Feb 28	AAT3.9	UHRF	CaII		1800	37
32964	EN Eri	2004 Dec 1	McD2.7	CS23	CaII, NaI	+2.5	900	29, 248
32045	S Eri	2004 Oct 20	McD2.7	CS21	CaII		1200	54
32045	S Eri	2004 Oct 20	McD2.7	CS21	NaI	+21.1	600	86
30127	HR1513	2004 Oct 20	McD2.7	CS21	CaII		1800	37
30127	HR1513	2004 Oct 20	McD2.7	CS21	NaI	+20.3	1800	109
34863	ν Lep	2005 Mar 16	McD2.7	CS21	NaI	-29.3	1200	56
34863	ν Lep	2005 Mar 16	McD2.7	CS21	CaII		1800	47
27925	HIP20521	2004 Dec 6	McD2.7	CS23	CaII, NaI	-4.9	1800	6, 83
32996	HR1661	2004 Dec 2	McD2.7	CS23	CaII, NaI	+2.5	1800	92, 315
29173	HR1460	2004 Dec 2	McD2.7	CS23	CaII, NaI	-1.7	1800	46, 193
28763	HR1438	2004 Oct 20	McD2.7	CS21	CaII		1800	24
28763	HR1438	2004 Oct 20	McD2.7	CS21	NaI	+18.7	1800	78
30020	DW Eri	2004 Oct 20	McD2.7	CS21	NaI	+19.2	1200	57
30020	DW Eri	2004 Oct 20	McD2.7	CS21	CaII		1800	14
30020	DW Eri	2004 Dec 2	McD2.7	CS23	CaII, NaI	-0.7	900	0, 96
28843	DZ Eri	2005 Mar 14	McD2.7	CS21	CaII		2700	36
28843	DZ Eri	2005 Mar 14	McD2.7	CS21	NaI	-27.2	1800	32
29554	HIP21640	2004 Nov 30	McD2.7	CS23	CaII, NaI	-0.3	1800	60, 206
32468	HIP23493	2005 Feb 14	McD2.7	CS21	CaII		1800	21
32468	HIP23493	2005 Feb 14	McD2.7	CS21	NaI	-27.5	1200	28
28208	HIP20747	2004 Dec 6	McD2.7	CS23	CaII, NaI	-5.1	1800	15, 96
31625	HIP23011	2004 Dec 6	McD2.7	CS23	CaII, NaI	-1.1	1800	4, 113
29851	HIP21837	2004 Dec 2	McD2.7	CS23	CaII, NaI	-0.7	1800	45, 238
30211	μ Eri	2003 Dec 3	McD2.7	CS12	CaII		3600	18
30211	μ Eri	2004 Oct 18	McD2.7	CS21	NaI	+19.3	1200	131
30211	μ Eri	2004 Oct 18	McD2.7	CS21	CaII		600	41
30211	μ Eri	2004 Nov 30	McD2.7	CS23	CaII, NaI	+0.1	900	184, 522
34503	τ Ori	2003 Dec 3	McD2.7	CS12	CaII		4800	38
34503	τ Ori	2004 Oct 19	McD2.7	CS21	NaI	+22.3	1200	265
33949	κ Lep	2004 Dec 3	McD2.7	CS23	CaII, NaI	+2.8	1800	0, 7
33949	κ Lep	2005 Feb 14	McD2.7	CS21	CaII		1200	68

Table 2.3 (cont'd)

HD #	Other Name	Date	Telescope ^a	Instrument ^b	Ion	v_{atm} km s ⁻¹	Exposure (s)	S/N
33949	κ Lep	2005 Feb 14	McD2.7	CS21	NaI	-27.4	1200	93
33949	κ Lep	2005 Feb 27	AAT3.9	UHRF	NaI	-29.7	2400	30
33949	κ Lep	2005 Feb 28	AAT3.9	UHRF	CaII		1800	37
28980	HIP21258	2004 Dec 2	McD2.7	CS23	CaII, NaI	-2.0	1800	46, 181
29248	ν Eri	2003 Dec 1	McD2.7	CS12	CaII		3600	36
29248	ν Eri	2003 Dec 2	McD2.7	CS12	NaI	-1.5	3600	25
30050	RZ Eri	2004 Dec 1	McD2.7	CS23	CaII, NaI	-0.0	1800	16, 156
28377	HIP20849	2004 Dec 6	McD2.7	CS23	CaII, NaI	-4.5	1800	8, 101
30535	HIP22304	2004 Dec 1	McD2.7	CS23	CaII, NaI	+0.4	1800	29, 178
31512	62 Eri	2004 Nov 30	McD2.7	CS23	CaII, NaI	+1.7	900	71, 240
27563	EM Eri	2004 Dec 1	McD2.7	CS23	CaII, NaI	-3.2	900	74, 273
33224	HR1671	2004 Nov 30	McD2.7	CS23	CaII, NaI	+3.5	900	38, 186
31089	HIP22669	2004 Dec 1	McD2.7	CS23	CaII, NaI	+1.1	1800	41, 143
34085	β Ori	2003 Dec 1	McD2.7	CS12	CaII		2400	119
34085	β Ori	2003 Dec 2	McD2.7	CS12	NaI	+3.7	2400	143
34085	β Ori	2004 Dec 2	McD2.7	CS23	CaII, NaI	+3.3	10	105, 431
34085	β Ori	2005 Feb 27	AAT3.9	UHRF	NaI	-29.7	900	316
34085	β Ori	2005 Feb 28	AAT3.9	UHRF	CaII		900	246
34085	β Ori	2005 Mar 22	McD2.7	CS12	CaII		2400	129
34085	β Ori	2006 Feb 17	McD2.7	CS21	CaII		1200	107
34085	β Ori	2006 Feb 17	McD2.7	CS21	NaI	-27.4	600	346
29009	EH Eri	2004 Dec 1	McD2.7	CS23	CaII, NaI	-1.6	900	71, 275
28262	HIP20787	2004 Dec 6	McD2.7	CS23	CaII, NaI	-4.9	2700	9, 65
32249	ψ Eri	2003 Dec 1	McD2.7	CS12	CaII		4800	19
32249	ψ Eri	2003 Dec 2	McD2.7	CS12	NaI	+1.9	4800	19
32249	ψ Eri	2004 Nov 30	McD2.7	CS23	CaII, NaI	+2.5	900	164, 398
31726	HR1595	2004 Dec 1	McD2.7	CS23	CaII, NaI	+2.0	1800	122, 301
30332	HIP22169	2004 Nov 30	McD2.7	CS23	CaII, NaI	+0.9	600	0, 3
30332	HIP22169	2004 Dec 1	McD2.7	CS23	CaII, NaI	+0.4	1800	40, 136
34816	λ Lep	2003 Dec 1	McD2.7	CS12	CaII		4800	16
34816	λ Lep	2003 Dec 2	McD2.7	CS12	NaI	+4.6	4800	25
26994	HIP19856	2004 Dec 6	McD2.7	CS23	CaII, NaI	-5.7	1800	46, 142
32612	HR1640	2004 Dec 2	McD2.7	CS23	CaII, NaI	+2.3	1800	86, 284
30679	HIP22406	2004 Dec 2	McD2.7	CS23	CaII, NaI	+0.1	1800	17, 190
30076	DX Eri	2003 Dec 1	McD2.7	CS12	CaII		7200	8
30076	DX Eri	2003 Dec 2	McD2.7	CS12	NaI	-0.2	3600	6
30076	DX Eri	2004 Nov 30	McD2.7	CS23	CaII, NaI	+0.4	900	101, 300
30963	HIP22588	2004 Nov 30	McD2.7	CS23	CaII, NaI	+1.5	1800	66, 241
27436	HIP20179	2004 Dec 6	McD2.7	CS23	CaII, NaI	-5.9	1800	15, 102
28497	DU Eri	2004 Oct 19	McD2.7	CS21	CaII		1200	52
28497	DU Eri	2004 Oct 19	McD2.7	CS21	NaI	+18.8	1200	98
28497	DU Eri	2004 Nov 30	McD2.7	CS23	CaII, NaI	-1.2	900	70, 228

^aMcD2.7: the Harlan J. Smith 2.7m Telescope at McDonald Observatory; AAT3.9: the Anglo-Australian 3.9m Telescope at the Anglo-Australian Observatory.

^bCS12: Coudé double-pass Spectrometer ($R \sim 500,000$); CS21: Cross-Dispersed Echelle Spectrometer (2D Coudé) Focus 1 ($R \sim 240,000$); CS23: Cross-Dispersed Echelle Spectrometer (2D Coudé) Focus 3 ($R \sim 60,000$); UHRF: Ultra High Resolution Facility ($R \sim 1,000,000$).

2.2.3 Data Reduction Steps

Data reduction steps were completed prior to the author's involvement in this project. Therefore only a summary of the general production procedure will be provided here. For a detailed description see Redfield (2007).

Each night of observing, sets of biases and flat field images were taken and combined to create a master bias and master flat for the night. The master flat (see image (c) in Figure 2.3) was used to identify the echelle orders that correspond to the orders in our science images that contain the absorption features. Virtual apertures were placed over these orders, and a polynomial function is fit to the order in the dispersion direction so we can characterize how the light varies across the chip. The same identification and tracing procedures are then applied to the science images which are then divided by the master flat for the night. After this the spectra are ready to be extracted as one-dimensional fits files composed of uncalibrated flux versus pixel number.

Before every exposure, a thorium argon comparison lamp spectra (see image (b) in Figure 2.3) was taken to provide a wavelength calibration. This wavelength solution is then applied to our extracted science spectra (see image (a) in Figure 2.3) allowing pixel numbers to be converted into a wavelength array.

From this point forward in the data reduction procedure, all reduction steps are carried out with programs written the Interactive Data Language (IDL) and are applied only to orders containing the sodium and calcium doublet absorption lines. Three steps remain in the reduction process before we can measure ISM absorption in the direction of the Sun's past motion through the Galaxy. Multiple observations are first added together and averaged to increase the S/N of the ISM absorption signal. Figure 2.4 is an example of what the data looks like at this

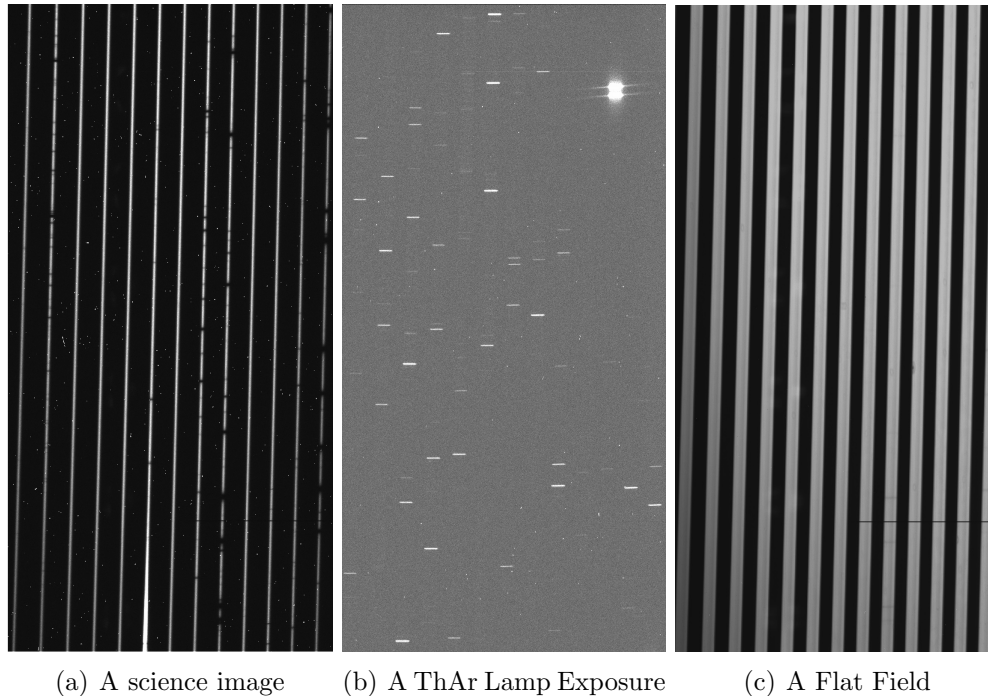


Figure 2.3: Data reduction images. Image (a) is an observation of a stellar spectrum split into orders that cover different wavelength ranges. Dark, horizontal regions in the lines correspond to wavelengths of light that are absorbed along the sight line to the star and are either due to ISM, the chemistry of our atmosphere, or absorption in the star itself. Image (b) is a thorium argon comparison lamp spectra, which is used to calibrate the wavelengths of our stellar spectra. Image (c) is a flat field which tells us how light varies across our chip due to instrumental effects.

point. The peak of this blaze function denotes the location of maximum intensity on the chip for this order, light falls off in intensity on either side. The rest wavelengths for the sodium doublet are marked by two vertical orange lines. We expect the ISM clouds to be moving at most a few hundreds of kilometers per second, velocities in this range will still be relatively close to their rest wavelengths, so we began looking for ISM absorption there.

The reduction process from this point on is illustrated in Figure 2.5. Panel 1 of the figure shows the region immediately surrounding the sodium doublet (5895.9242 and 5889.9510 Å). The second panel shows the same data range with

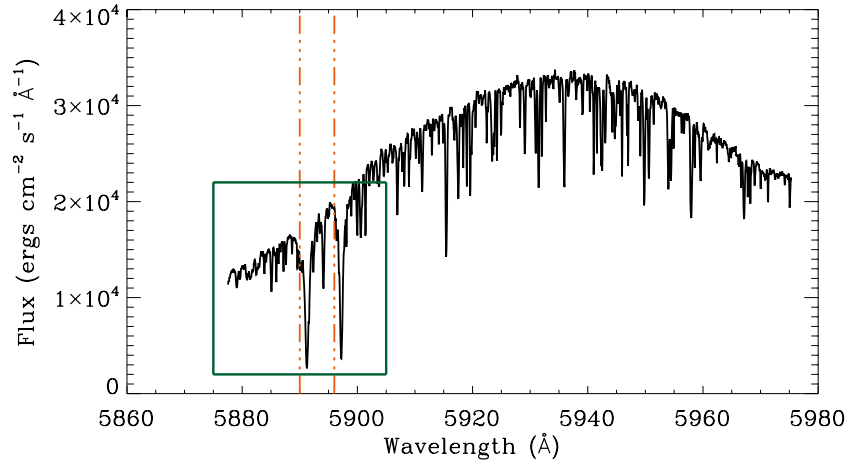


Figure 2.4: The raw, un-normalized echelle order containing the sodium doublet absorption towards HD30020. The sodium doublet is marked by two vertical orange lines, seen nearby are two broad sodium features that are likely due to absorption by sodium on the stellar surface. The radial velocity of this star is 40 km s^{-1} which results in a wavelength shift of any stellar sodium absorption towards the red end of the spectrum, which would explain why the stellar sodium absorption components are seen at slightly longer wavelengths. The green box outlines the region for which the remainder of the reduction process will be detailed.

a solution to the shape of the flux continuum in the region over plotted in red. Panel 3 shows the same data with the continuum solution divided out. The result is a normalized flux continuum which will allow us to accurately measure the amount of absorbing material.

The majority of weak lines still present in the data at this point are due to water vapor in Earth’s atmosphere. This telluric contamination must be modeled and removed from the data before we can measure the interstellar sodium absorption. A modeling technique used by Redfield (2007) was employed to remove this contamination. The model is allowed to vary in wavelength range, position and strength until it is matched to the observed profile. The model determined for our region is plotted in blue in panel 4, and panel 5 shows the result once the model is used to subtract out the telluric profile.

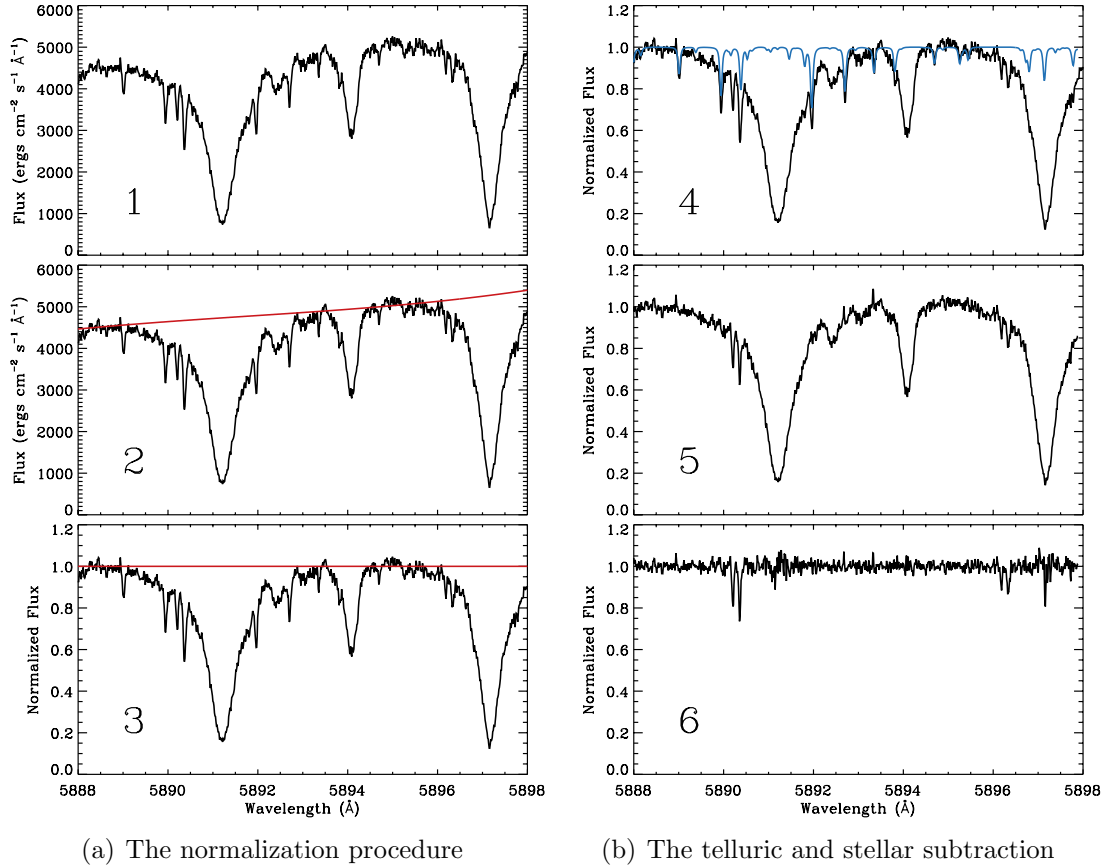


Figure 2.5: Figures illustrating the reduction procedure for a sodium observation. Panel 1 shows the raw data in the range of the sodium doublet. Panel 2 and 3 show the continuum fit and the result once it is divided out. Panel 4 plots our solution to the telluric contamination in the data range and panel 5 is the result once the model is subtracted from the data. In panel 5 the ISM absorption can be identified a little more easily, in panel 6 the stellar component is modeled and removed and two sodium components can be seen in absorption near the rest wavelengths of the sodium doublet.

The broad features remaining in the data are most likely stellar sodium absorption. The SIMBAD Astronomical Database can be queried for stellar radial and rotational velocities (if known) which can then be used to help identify stellar features in the data. If the position and width of the suspected stellar profile matches the radial velocity and $v \sin i$ of the star (if known), then we can be sure that the feature is stellar and can be modeled and removed. Stellar components, like the one in Figure 2.5 are much wider than the ISM components, this is due to the high surface temperatures of stars and high rotational velocities. Rotational and thermal broadening causes stellar lines to be much wider than the cool, weak ISM lines.

The final result of the reduction process is shown in panel 6 of Figure 2.5. Here all non-ISM features have been removed and two weak signatures of ISM absorption can be seen appearing near the rest wavelengths for D1 and D2. The process of ISM absorption measurement is detailed in the next chapter.

Chapter 3

ISM Absorption Measurements

Much can be learned from analyzing the position, shape and depth of a particular ISM absorption profile. The position of the wavelength centroid tells us the radial velocity of the cloud, determined with use of the Doppler effect and information about its rest wavelength. The shape, or width of the profile gives us information about the temperature and turbulent velocity of the cloud. Finally the depth of the line tells us about the amount of absorbing material along the line of sight.

3.1 Measuring ISM Absorption

ISM absorption measurements were made with the IDL program `gismfit.pro` which has been tested and utilized for a wide variety of observations (Redfield & Linsky 2002, 2004). The program uses a Marquart χ^2 minimization technique to fit Gaussian absorption profiles to the data. The program queries for initial guesses for absorption centroid wavelength, width (or Doppler parameter) and log column density. Initial guesses come from visual inspection of raw data plotted in velocity space. The program then attempts to find absorption profiles in the data near the input values, occasionally this process returns a poor fit but yields better initial guesses. The fitting routine is repeated (altering initial guesses) until a satisfactory fit is produced, and the reduced χ^2 has reached a minimum.

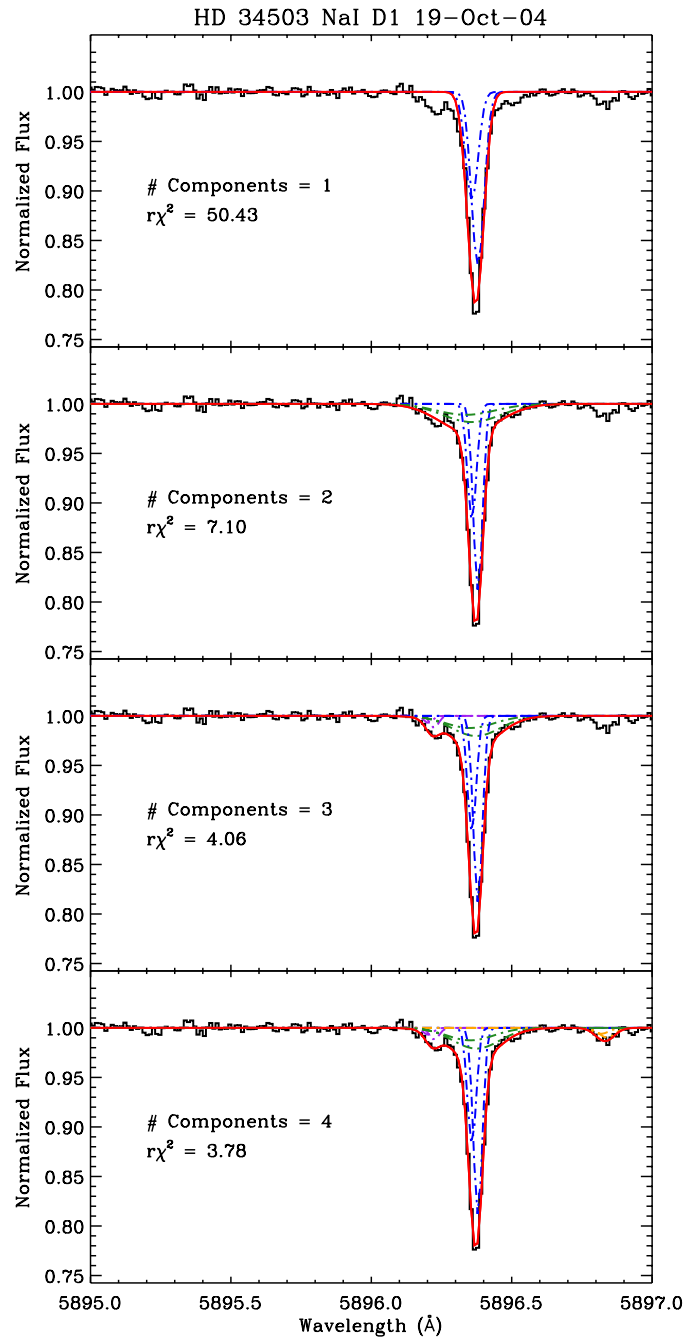


Figure 3.1: An F-Test sequence. Initially the ISM absorption was fit with one component, additional components were added until either the $r\chi^2$ of each subsequent fit stopped decreasing, or the fit failed the F-test meaning that the addition of the last component is not a statistically significant improvement over the previous fit. For this particular observation, the addition of the 4th component did not significantly improve the $r\chi^2$. Single ISM components are plotted in color coded dashed lines, total fit in red.

Each sightline was initially fit with one component unless visual inspection of the raw data strongly suggested the presence of multiple clouds. After this initial fit, guesses for additional components were fed into `gismfit.pro` to investigate the possibility of multiple clouds. Each observation was then fit with an increasing number of components until an F-test no longer warranted the addition. The F-test is a method for comparing the quality of two fits to the same data using a different number of free parameters (Bevington 2003). This is accomplished by taking the ratio of the higher χ^2 (corresponding to the worse fit and presumably more free parameters) to the lower χ^2 (corresponding to the better fit, and less free parameters). With each addition of another component, the χ^2 naturally goes down since you are able to fit smaller and finer components, eventually a point is reached when `gismfit.pro` begins to fit noise in the data, so the F-test is used to determine if each addition of another component is statistically justified.

This process of a best-fit determination is illustrated in Figure 3.1. The form of χ^2 evaluated for each fit was the reduced χ^2 ($r\chi^2$), which is the χ^2 of the fit divided by the number of free parameters used. Each of the four panels has the same ISM absorption profile which is first fit with one component, then two, three, and finally four individual ISM profiles. Each additional component was statistically motivated by the F-test save for the addition of the 4th component. So the final fit we used to describe this data set was three ISM clouds.

3.1.1 Multiple Instrument Resolution Fits

Occasionally a complex absorption profile's fit was not endorsed by the F-test, but a fit with more components was motivated due to other observations of the same sightline. Other observations taken at higher resolutions were able

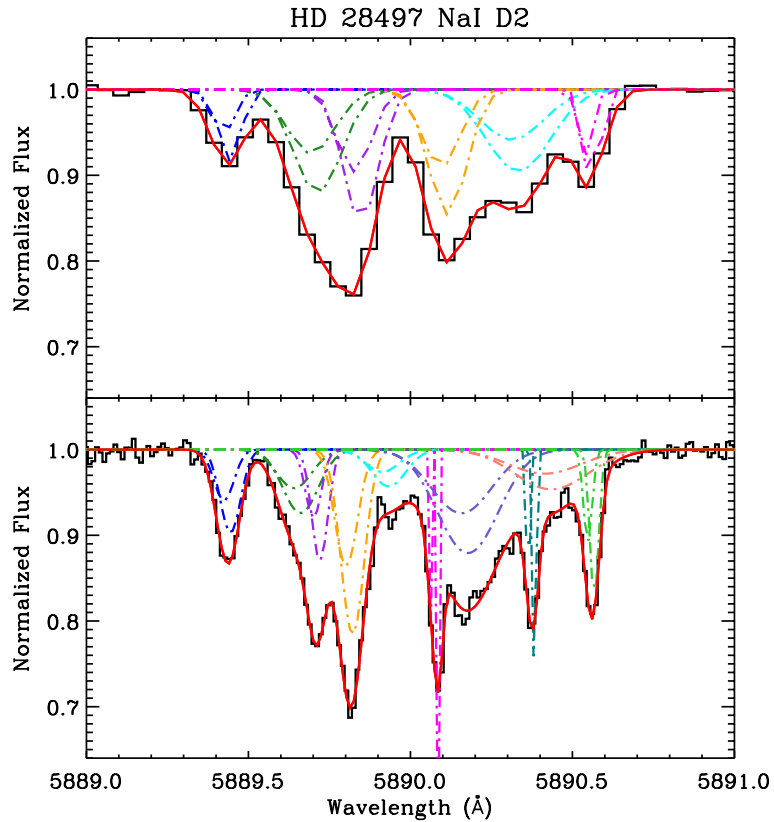


Figure 3.2: HD28497 NaI absorption at two different resolutions. The top panel is data taken with CS23 at a resolution of $R \sim 60,000$, and the bottom panel was taken with CS21 at a resolution of $R \sim 240,000$. Most of the narrow absorbers seen in the higher resolution observation fail to be resolved in the lower resolution observation. However both these observations yielded the same measurement of total column density (within the errors) along this particular sightline.

to resolve the presence of narrow components that are otherwise indiscernible at lower resolutions. Our data set contains a few sight lines along which the ISM absorption was measured multiple times at different resolutions. In almost all cases, the highest resolution observation was chosen to represent the ISM absorption along the line of sight and measurements of cloud parameters were based on that observation.

Figure 3.2 shows an example of ISM absorption towards the star HD28497 observed at two different resolutions. When running the fitting routine on the high-resolution absorption spectra in the lower panel, `gismfit.pro` was able to successfully fit 10 components validated by the F-test, while running the same process on the lower-resolution data in the upper panel validated a fit consisting of only 6 components. In both cases, the fit yields a measurement of total column density that is the same (within the errors) for both observations: the CS23 total column density for this particular observation was measured to be $11.948^{+0.014}_{-0.016}$ for 6 components and the CS21 fit yielded a total column density of $11.936^{+0.036}_{-0.060}$ for 10 components. It is encouraging that we arrive at the same total column density, regardless of the resolution. Table 3.5 lists all observations taken at two or more multiple resolutions.

Even our highest resolution fits are sometimes unable to fit the weakest components in the data. Broad features, such as the broad, shallow, salmon-colored component near $\sim 5890.4 \text{ \AA}$ in the bottom panel of Figure 3.2 are not necessarily representative of the actual ISM absorption along that line of sight, rather we think that it is a blend of several small absorption components too weak to be resolved by our telescope instrumentation or fit by `gismfit.pro`.

Table 3.1. Multiple Instrument Resolution Fits

HD #	Ion	Components	Instrument	log N (cm^{-2})
30020	NaI	2	cs23	11.18 $^{+0.09}_{-0.22}$
30020	NaI	2	cs21	11.13 $^{+0.030}_{-0.038}$
30211	NaI	1	cs21	12.11 $^{+0.14}_{-0.27}$
30211	NaI	2	cs23	12.01 $^{+0.14}_{-0.48}$
33949	NaI	3	cs21	11.704 $^{+0.017}_{-0.019}$
33949	NaI	3	uhrf	11.515 ± 0.028
34085	NaI	5	cs12	11.684 ± 0.0050
34085	NaI	4	cs23	11.671 $^{+0.026}_{-0.035}$
34085	NaI	4	uhrf	11.524 ± 0.0016
34085	NaI	6	cs21	11.664 $^{+0.019}_{-0.027}$
32249	NaI	2	cs12	11.945 ± 0.0052
32249	NaI	3	cs23	12.142 $^{+0.050}_{-0.066}$
28497	NaI	10	cs21	11.936 $^{+0.036}_{-0.060}$
28497	NaI	6	cs23	11.948 $^{+0.014}_{-0.016}$
30211	CaII	1	cs12	11.489 ± 0.0094
30211	CaII	2	cs21	11.73 ± 0.11
30211	CaII	2	cs23	11.738 $^{+0.019}_{-0.021}$
34085	CaII	5	cs12	11.507 ± 0.0030
34085	CaII	5	cs23	11.48 $^{+0.07}_{-0.13}$
34085	CaII	8	uhrf	11.549 ± 0.011
34085	CaII	7	cs12	11.517 ± 0.0042
32249	CaII	1	cs12	11.715 ± 0.0091
32249	CaII	3	cs23	12.07 $^{+0.10}_{-0.23}$
28497	CaII	5	cs21	12.202 $^{+0.034}_{-0.047}$
28497	CaII	6	cs23	12.152 $^{+0.043}_{-0.12}$

3.2 Fits

Figures 3.3 through 3.19 are the F-test motivated, flux-normalized, best-fit results of the fitting process for each sightline in the data set ordered by distance to each background star. Absorption spectra for each line in both sodium and calcium doublets are plotted in black (if observations exist), each individual absorption component is plotted in a dash-dot line and color coded to allow for separate components to be easily distinguished from one another. Two Gaussian profiles are plotted for each sodium line due to the hyper-fine nature of the D1 and D2 lines, while calcium has only one Gaussian profile per component. The fit to the total absorption profile is plotted in red after it has been convolved with the resolution of the instrument that the data were taken with. HD number and distance to the target star are plotted at the top of each data set, specific line and the number of components used in the fit are included in each plot.

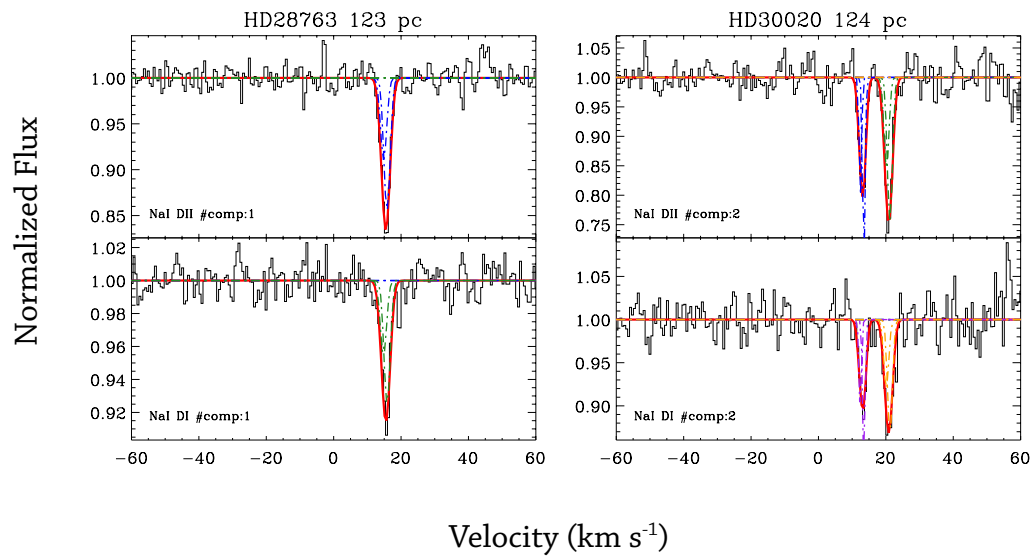


Figure 3.3: Best-fit result of our fitting procedure. Spectra is plotted in black, individual components are color-coded and plotted with a dash-dot line. Total absorption profile fit is plotted in red.

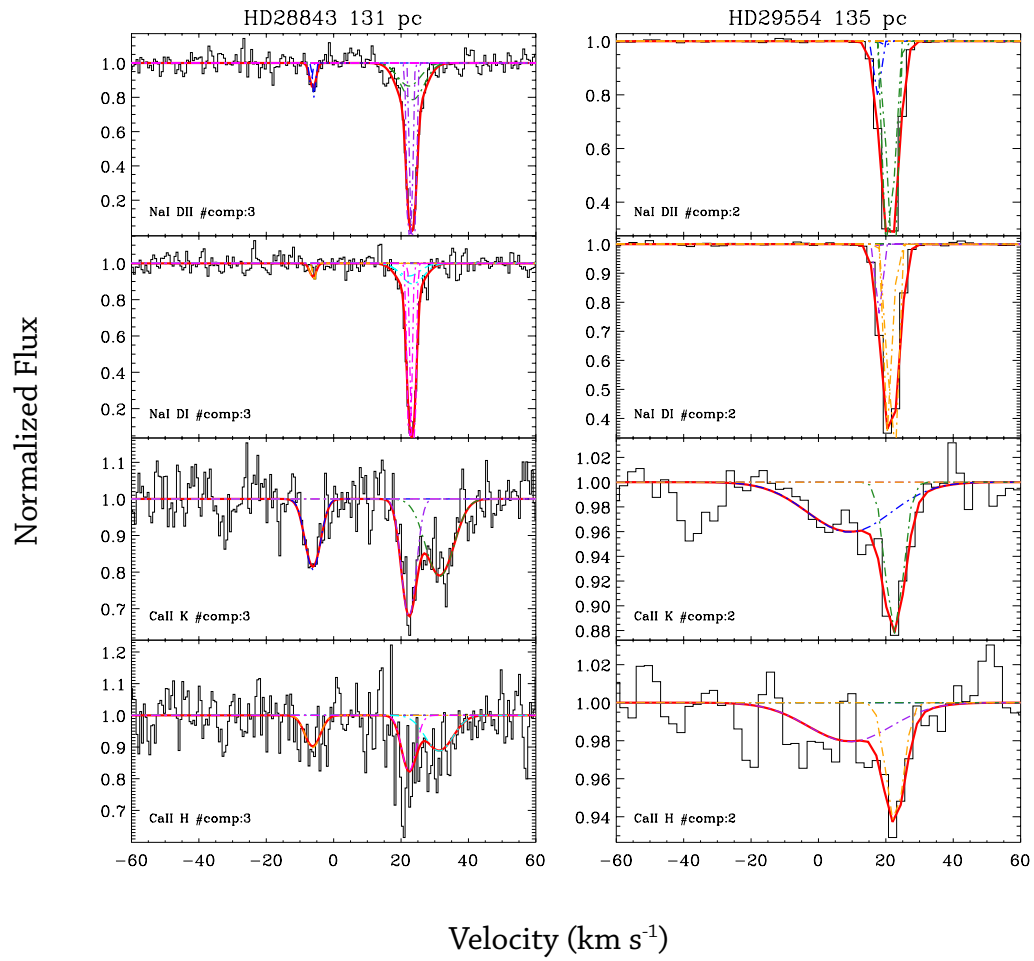


Figure 3.4: Same as Figure 3.3

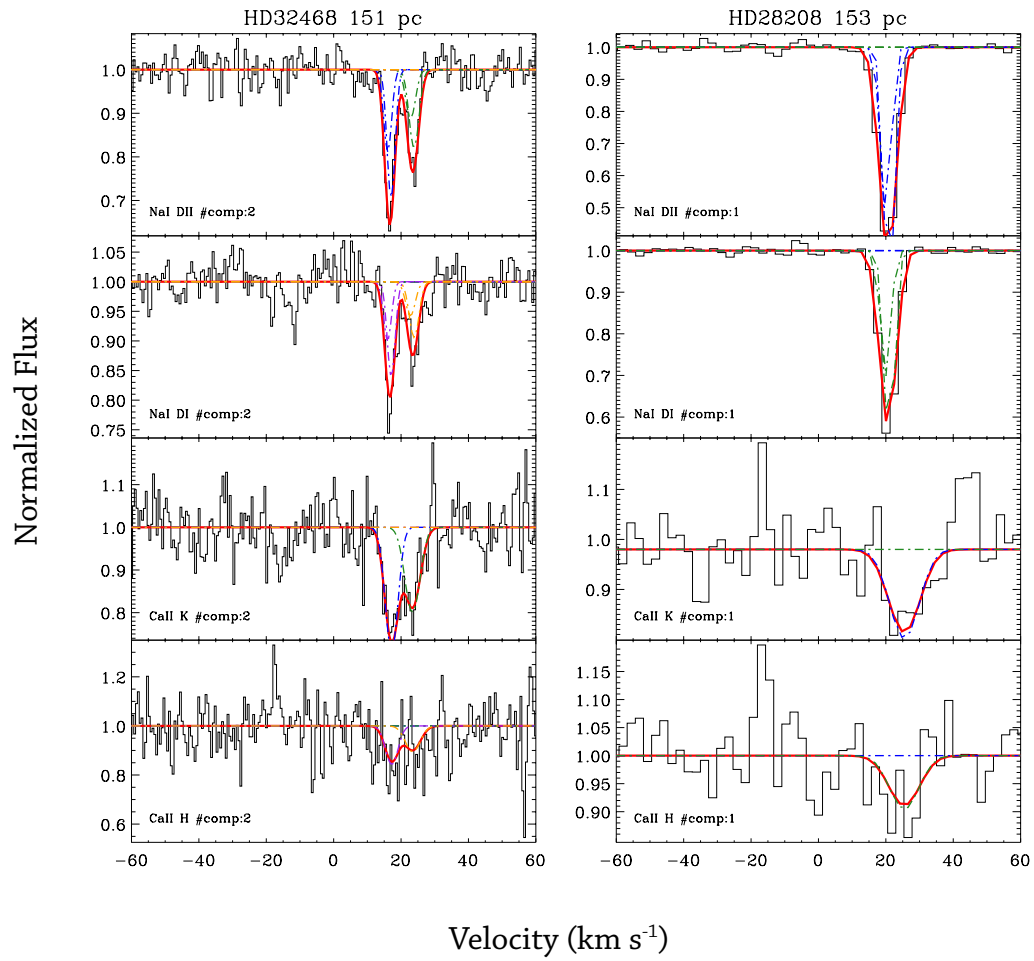


Figure 3.5: Same as Figure 3.3

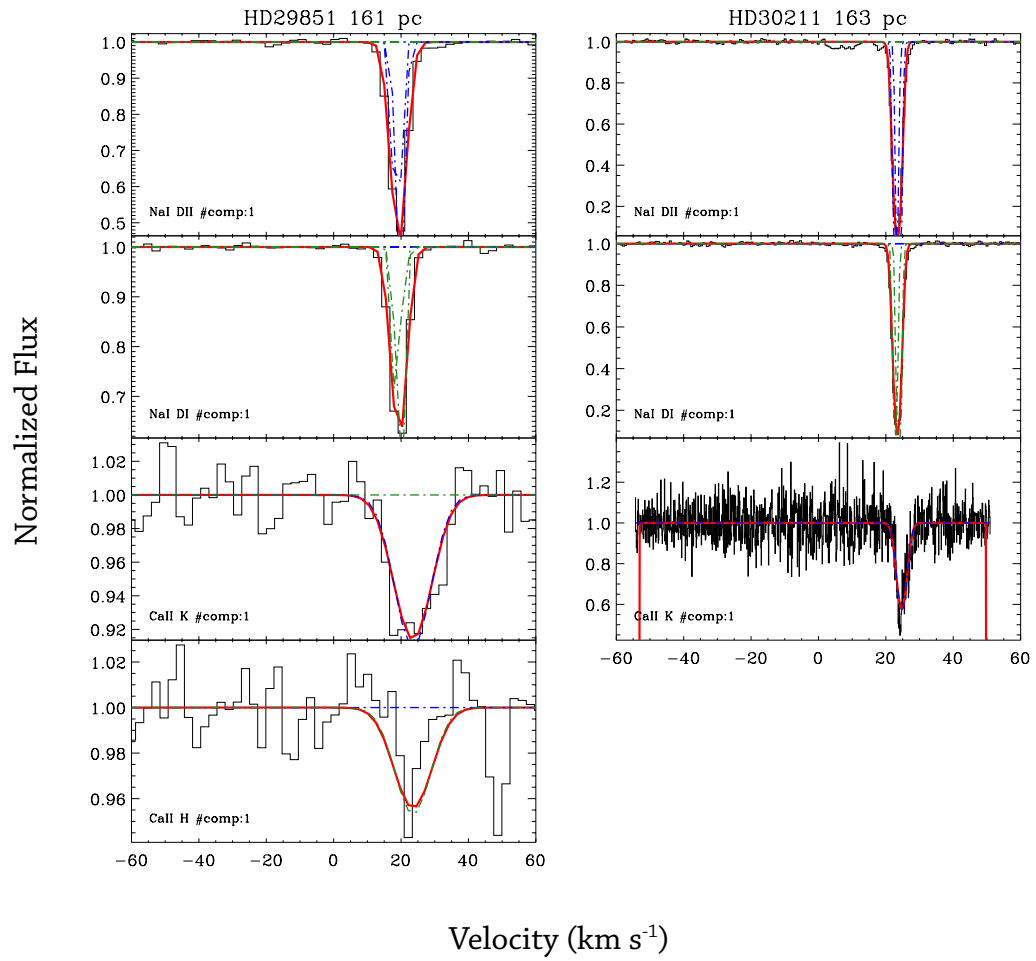


Figure 3.6: Same as Figure 3.3

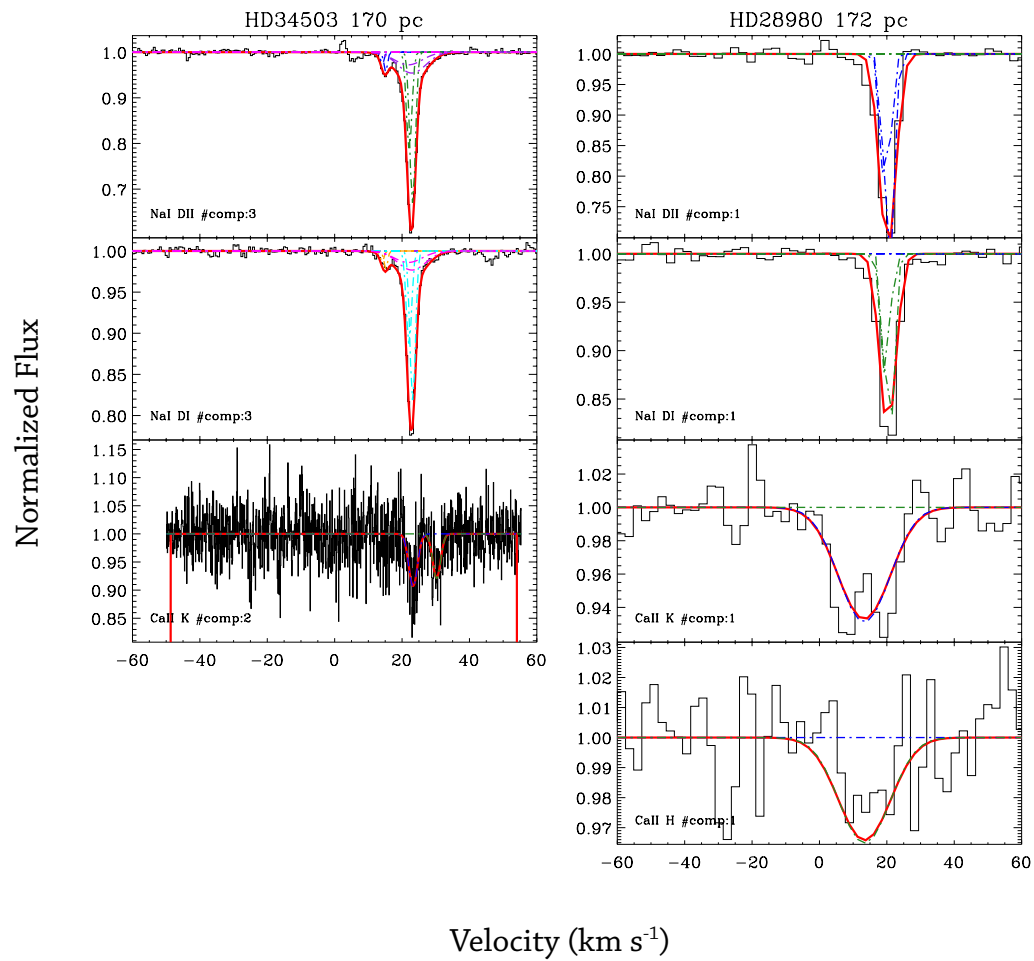


Figure 3.7: Same as Figure 3.3

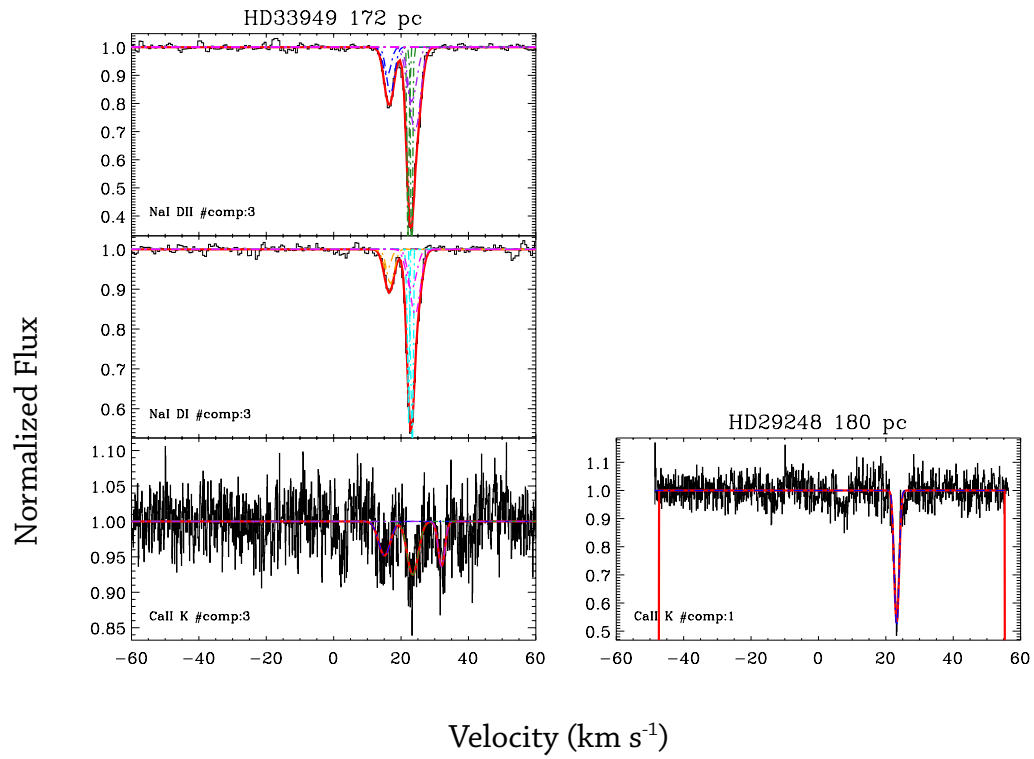


Figure 3.8: Same as Figure 3.3

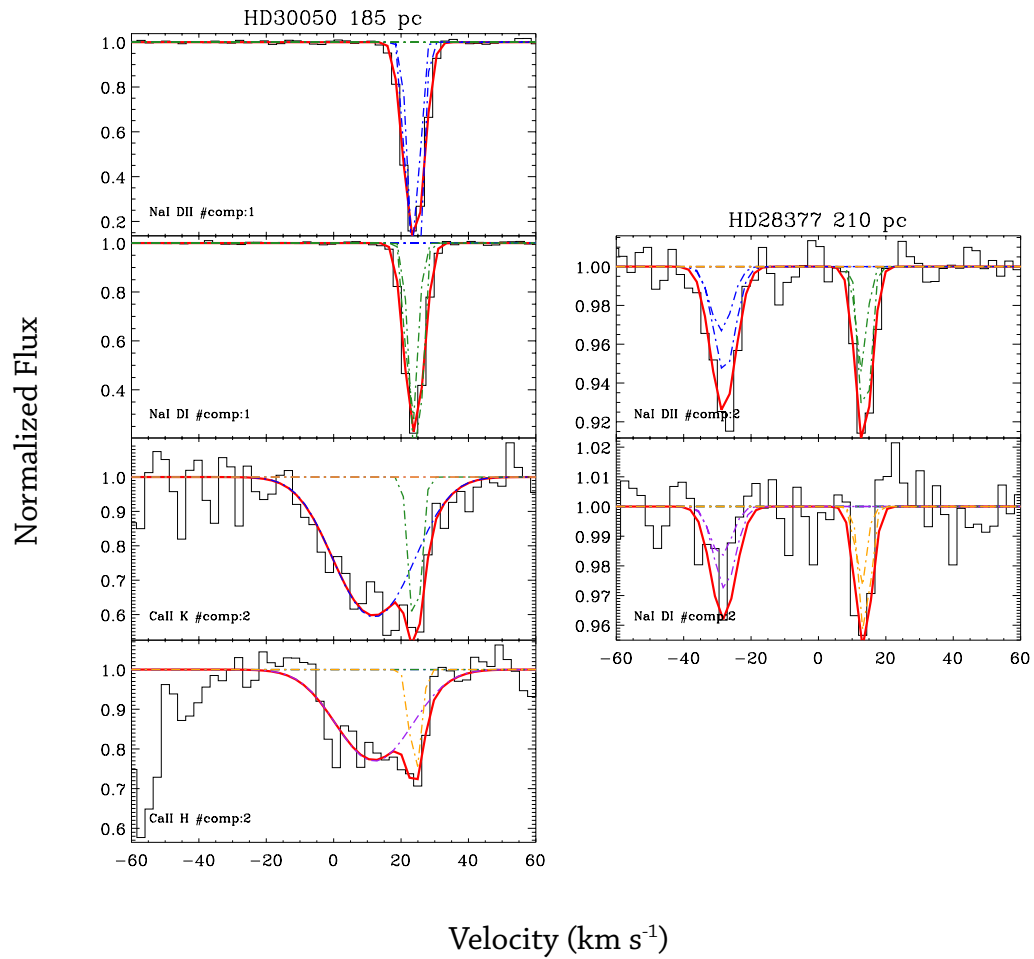
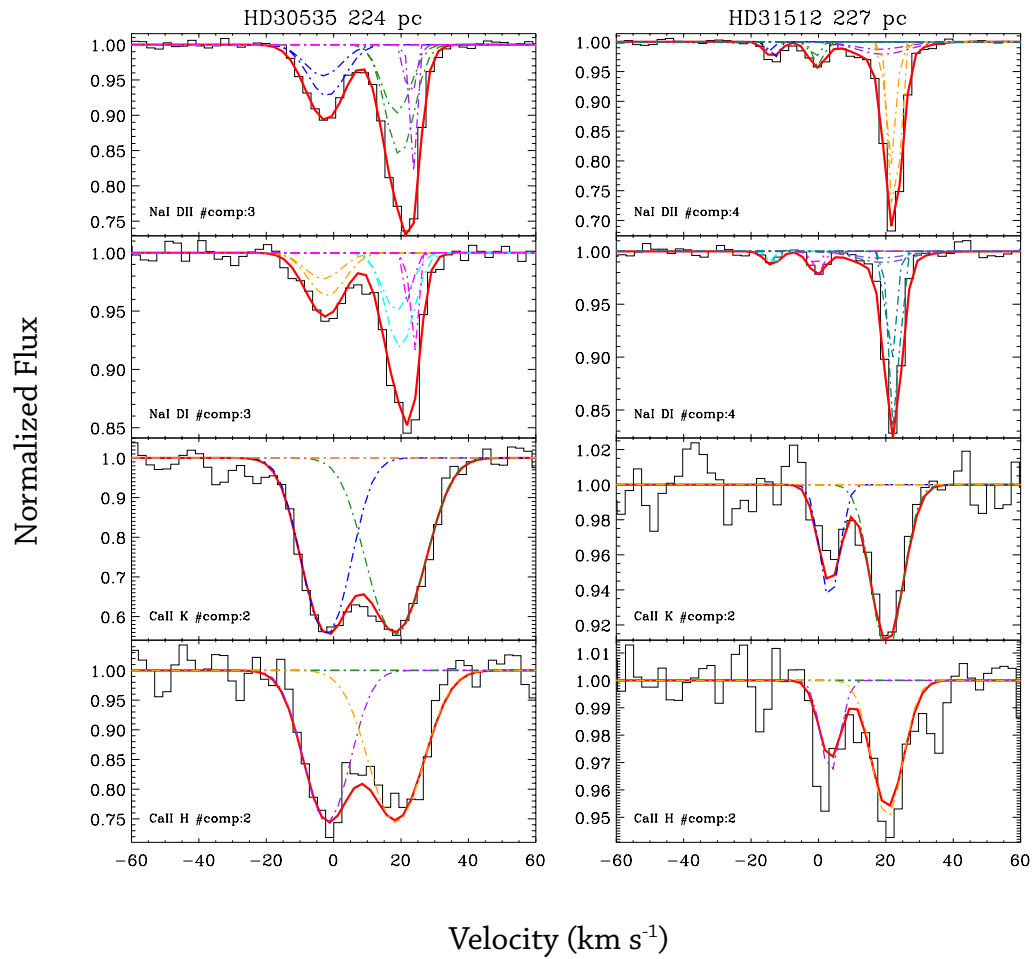


Figure 3.9: Same as Figure 3.3

**Figure 3.10:** Same as Figure 3.3

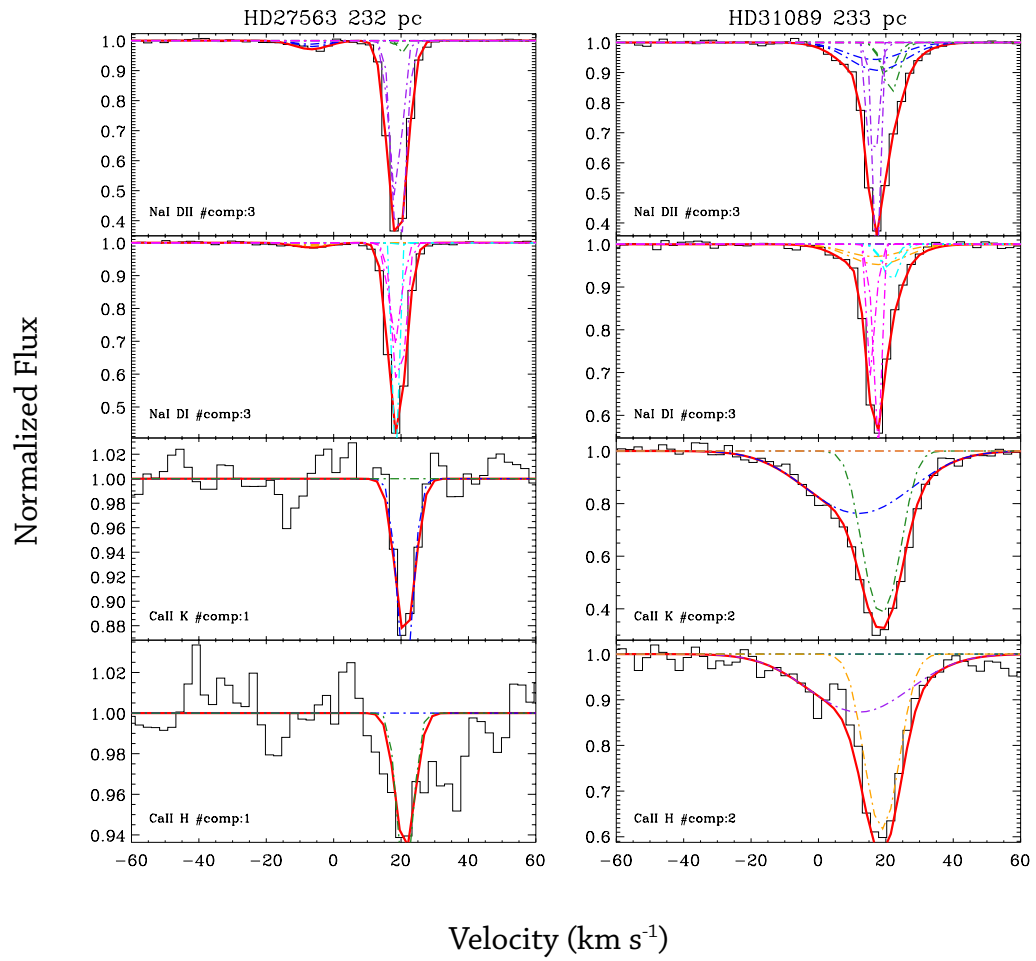


Figure 3.11: Same as Figure 3.3

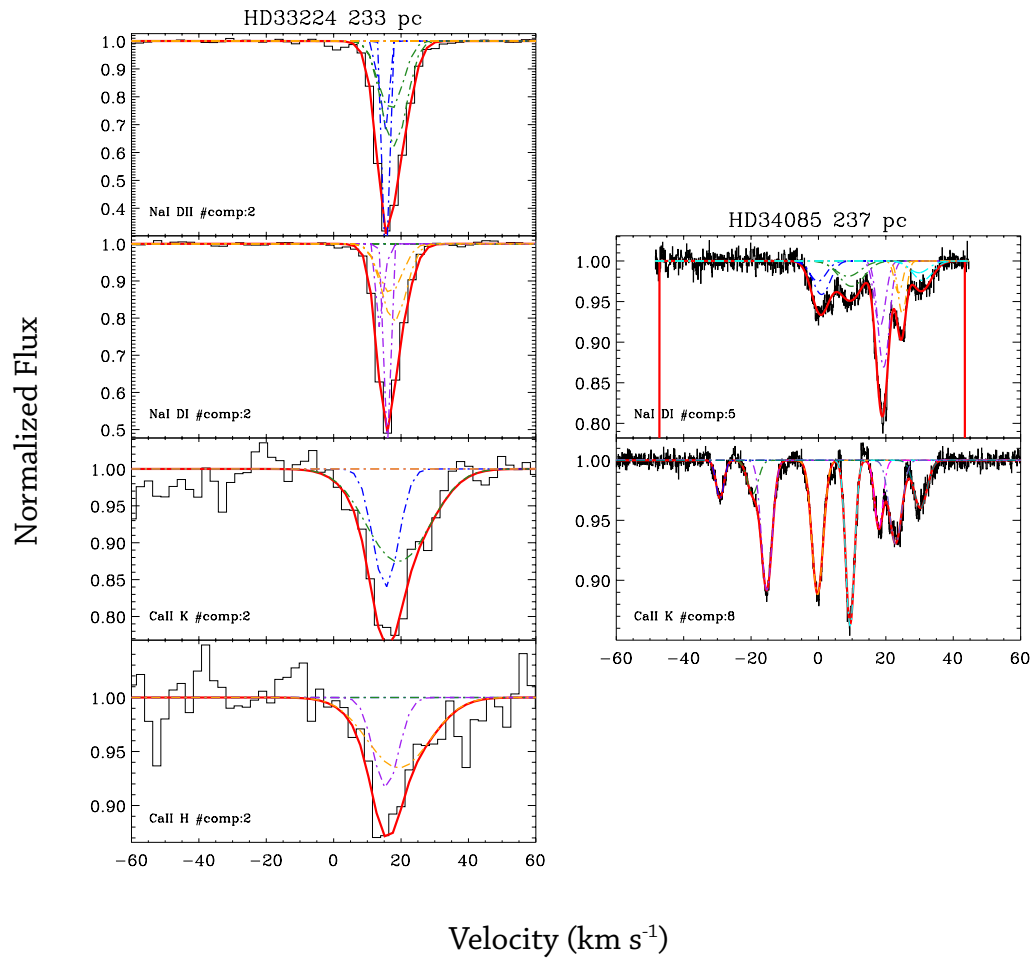


Figure 3.12: Same as Figure 3.3

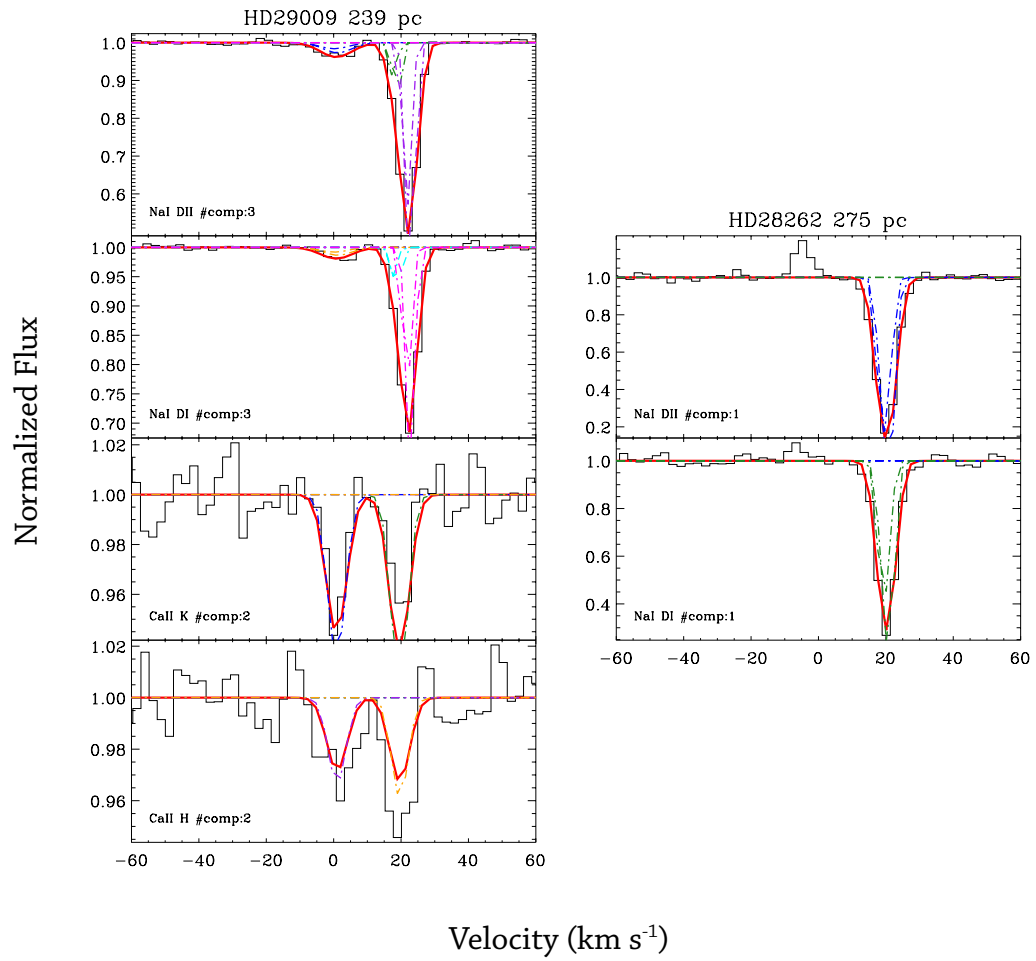


Figure 3.13: Same as Figure 3.3

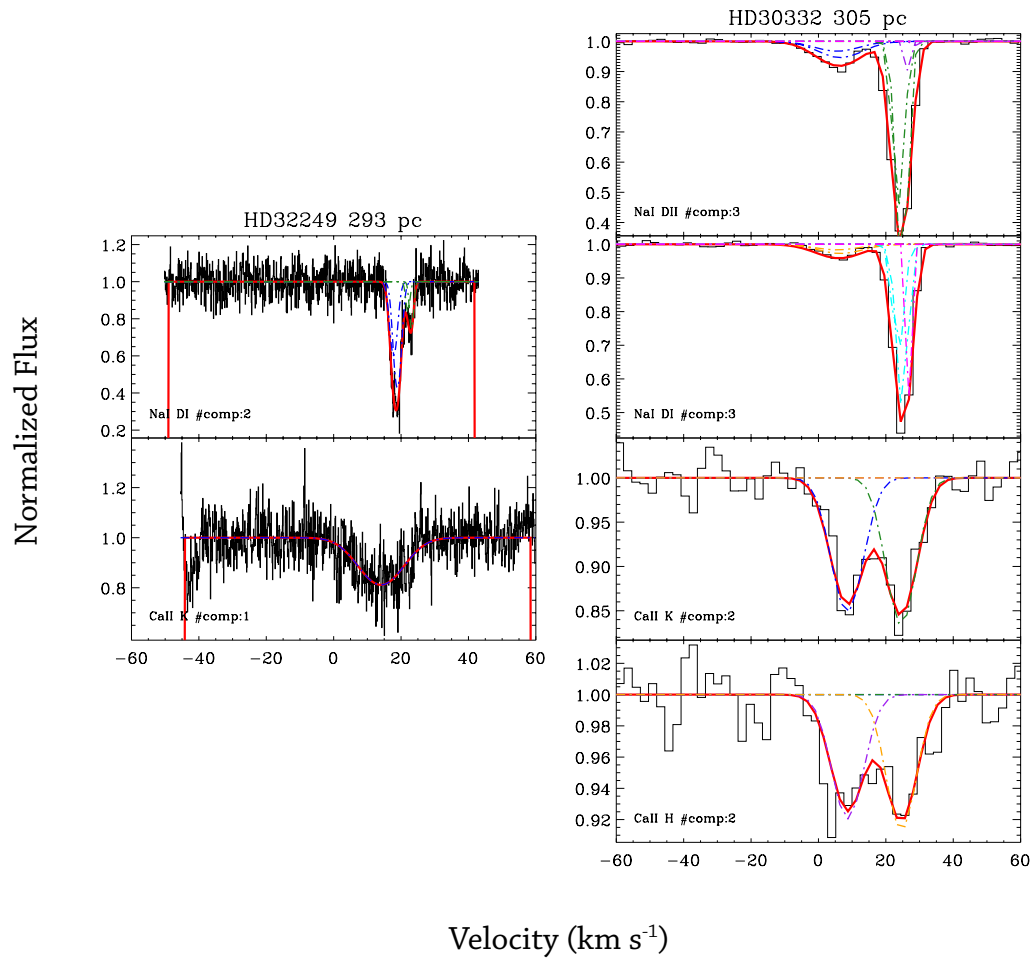


Figure 3.14: Same as Figure 3.3

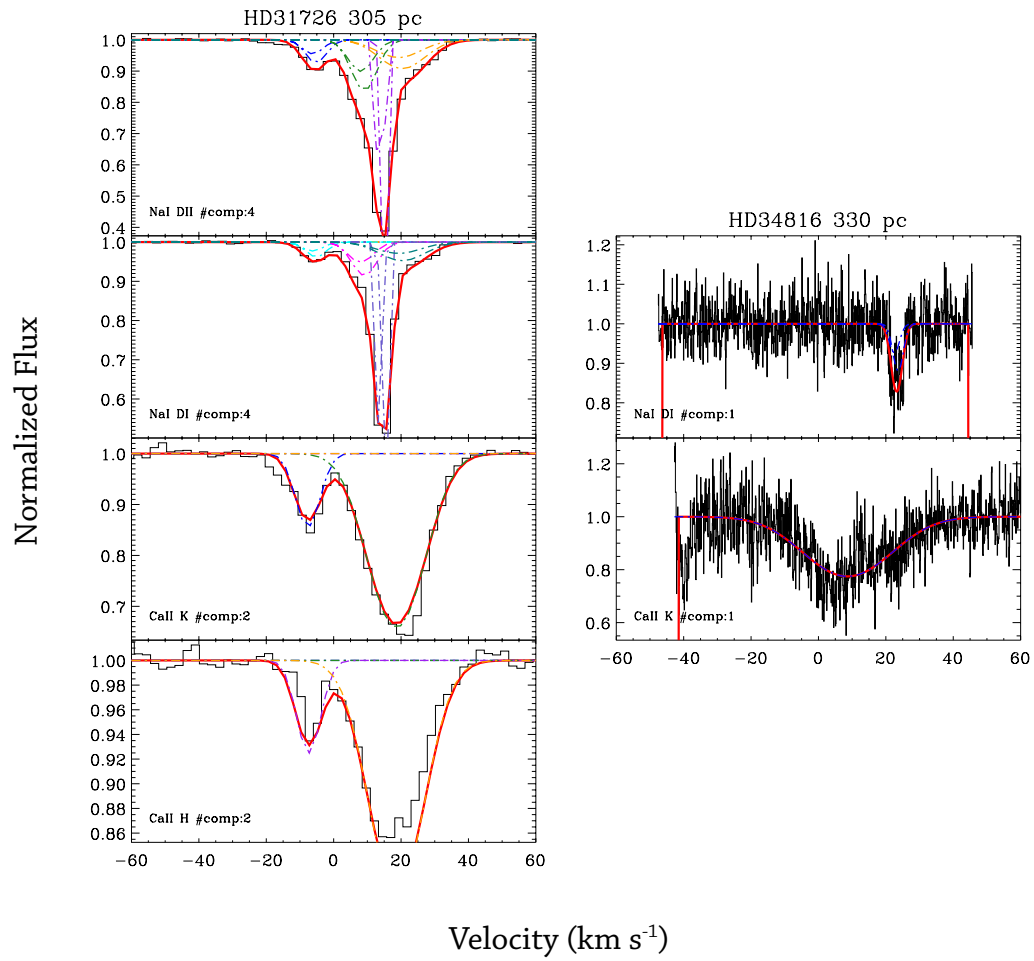


Figure 3.15: Same as Figure 3.3

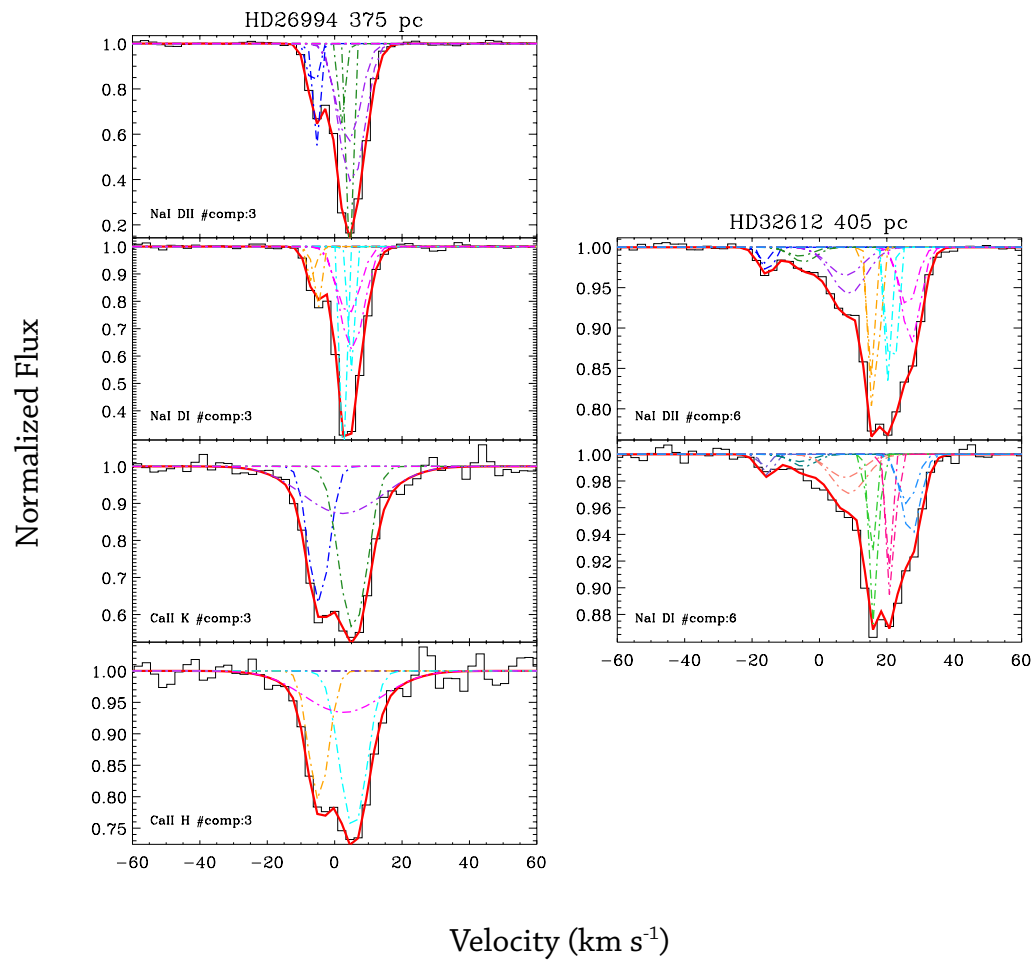


Figure 3.16: Same as Figure 3.3

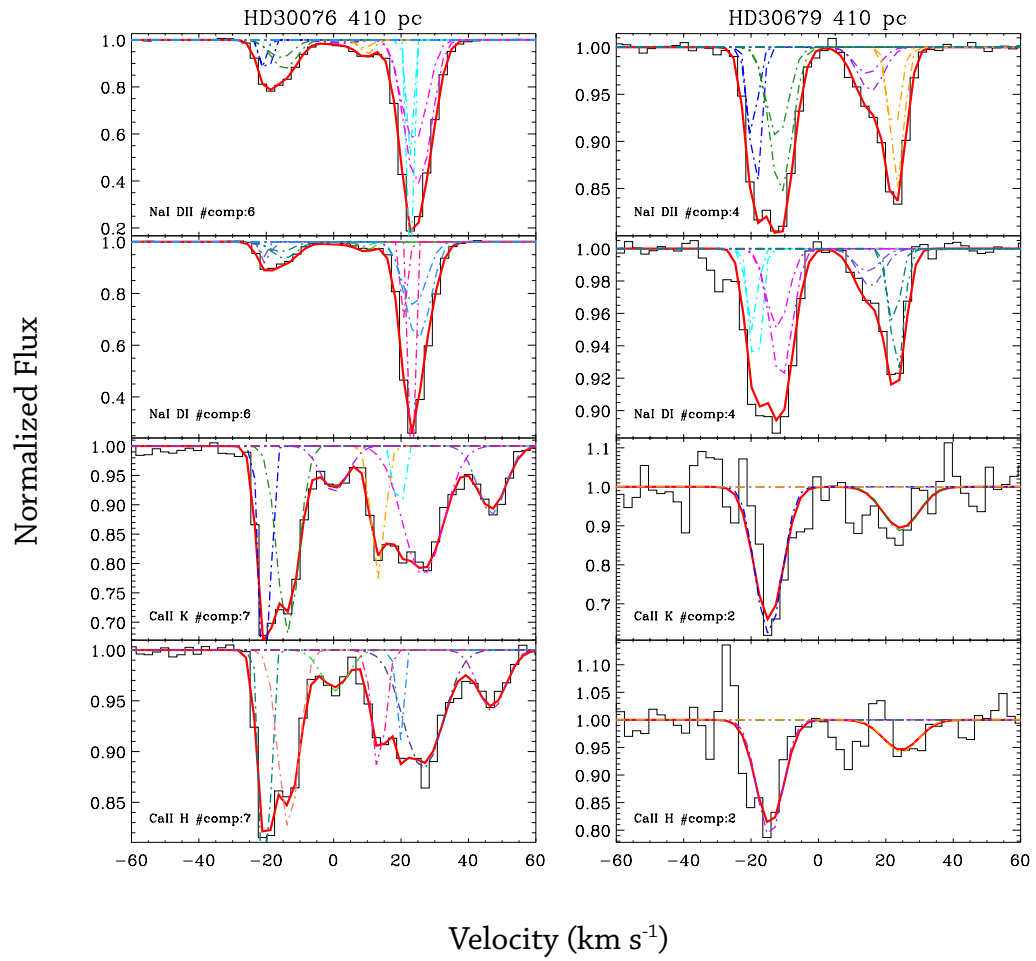
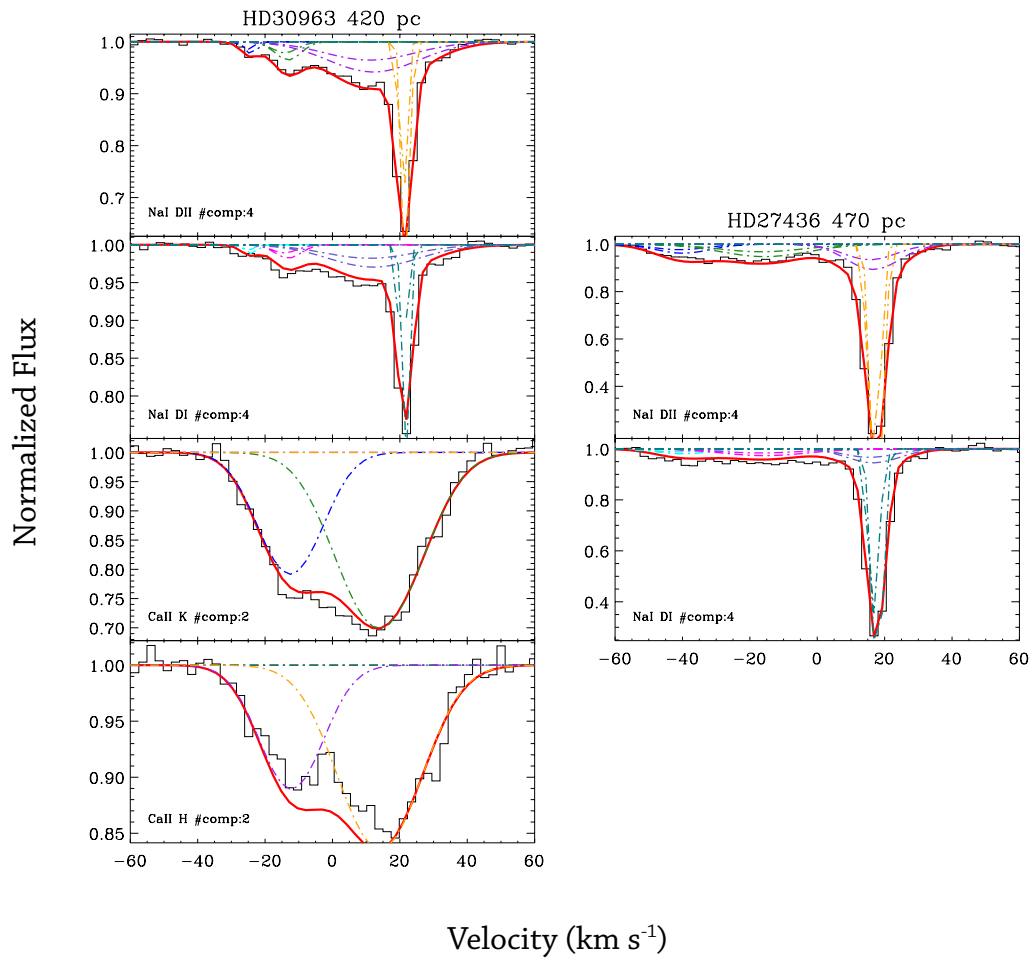


Figure 3.17: Same as Figure 3.3

**Figure 3.18:** Same as Figure 3.3

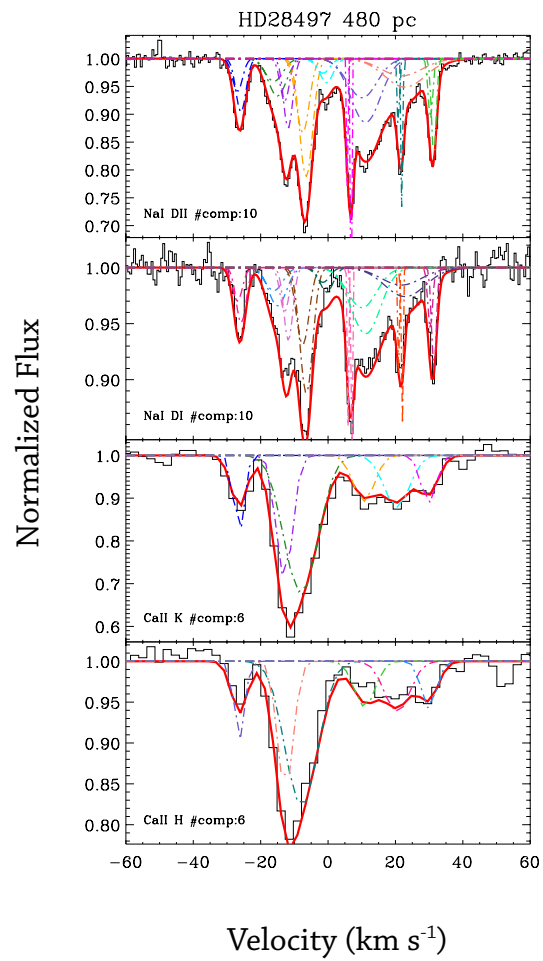


Figure 3.19: Same as Figure 3.3

3.3 Fit Results

Tables 3.2 through 3.5 tabulate the parameter results for each of the fits shown in the previous section. Table 3.2 lists the properties of individual calcium components seen in absorption towards each sightline ordered by distance. Instrument used to obtain the data as well as component velocity, Doppler parameter, and log column density are listed for each sightline. Table 3.3 tabulates the computed total calcium column density along each sightline, where we can begin to see the first suggestion of an overall trend in increasing total column density with distance. Table 3.4 is the same component-by-component break down of individual sodium absorption component values for velocity, Doppler parameter and log column density. The general increase in column density with distance becomes much more apparent in Table 3.5 where total column density per sightline is listed for the sodium data.

Table 3.2. Ca II ISM Fit Parameters for Targets along the Past Solar Trajectory

HD #	Component #	Instrument	v (km s ⁻¹)	b (km s ⁻¹)	$\log N$ (cm ⁻²)
28843	1	cs21	-6.212 ± 0.21	2.90 ± 0.95	11.25 ^{+0.13} _{-0.19}
28843	2	cs21	22.13 ± 0.93	2.7 ± 1.1	11.451 ^{+0.073} _{-0.089}
28843	3	cs21	31.2 ± 2.4	5.6 ± 2.6	11.5 ^{+0.3} _{-1.2}
29554	1	cs23	7.8 ± 4.1	19.3 ± 4.5	11.32 ^{+0.12} _{-0.11}
29554	2	cs23	22.548 ± 0.091	3.65 ± 0.20	11.117 ^{+0.011} _{-0.011}
32468	1	cs21	17.01 ± 0.86	2.548 ± 0.032	11.29 ^{+0.15} _{-0.20}
32468	2	cs21	23.10 ± 0.47	4.3 ± 5.1	11.36 ± 0.41
28208	1	cs23	23.8 ± 1.6	7.3 ± 1.1	11.30 ^{+0.19} _{-0.33}
29851	1	cs23	23.36 ± 0.36	6.2 ± 3.9	11.26 ^{+0.14} _{-0.20}
30211	1	cs12	24.715 ± 0.037	2.055 ± 0.041	11.489 ± 0.0094
34503	1	cs12	23.266 ± 0.091	1.80 ± 0.13	10.681 ± 0.021
34503	2	cs12	30.23 ± 0.11	1.64 ± 0.14	10.562 ± 0.028
28980	1	cs23	13.15 ± 0.95	10.2 ± 2.6	11.31 ^{+0.12} _{-0.17}
33949	1	uhfr	15.08 ± 0.42	2.45 ± 0.58	10.516 ± 0.076
33949	2	uhfr	23.46 ± 0.25	2.32 ± 0.34	10.693 ± 0.058
33949	3	uhfr	32.00 ± 0.34	1.38 ± 0.67	10.391 ± 0.081
29248	1	cs12	23.190 ± 0.015	0.912 ± 0.016	11.213 ± 0.0057
30050	1	cs23	11.0 ± 2.2	14.5 ± 3.0	12.305 ^{+0.061} _{-0.071}
30050	2	cs23	23.75 ± 0.83	3.5 ± 1.7	11.65 ^{+0.21} _{-0.44}
30535	1	cs23	-2.06 ± 0.19	9.07 ± 0.90	12.159 ^{+0.021} _{-0.022}
30535	2	cs23	18.56 ± 0.41	10.70 ± 0.61	12.227 ^{+0.032} _{-0.034}
31512	1	cs23	2.9 ± 1.2	3.82 ± 0.90	10.87 ^{+0.10} _{-0.12}
31512	2	cs23	20.33 ± 0.45	6.5 ± 2.2	11.25 ^{+0.12} _{-0.16}
27563	1	cs23	21.21 ± 0.18	3.2 ± 2.3	11.18 ^{+0.13} _{-0.18}
31089	1	cs23	11.98 ± 0.57	20.3 ± 4.6	12.180 ^{+0.017} _{-0.017}
31089	2	cs23	18.70 ± 0.17	6.58 ± 0.37	12.236 ^{+0.026} _{-0.027}
33224	1	cs23	15.22 ± 0.40	5.7 ± 1.9	11.42 ^{+0.13} _{-0.19}
33224	2	cs23	20.6 ± 1.4	11.7 ± 1.6	11.57 ^{+0.13} _{-0.14}
34085	1	uhfr	-29.20 ± 0.061	1.645 ± 0.076	10.157 ± 0.019
34085	2	uhfr	-19.48 ± 0.45	2.27 ± 0.37	10.241 ± 0.089
34085	3	uhfr	-15.32 ± 0.071	2.201 ± 0.085	10.834 ± 0.036
34085	4	uhfr	-0.271 ± 0.024	2.312 ± 0.032	10.871 ± 0.0052
34085	5	uhfr	9.389 ± 0.019	1.790 ± 0.026	10.857 ± 0.0061
34085	6	uhfr	17.898 ± 0.076	1.765 ± 0.095	10.441 ± 0.021
34085	7	uhfr	22.867 ± 0.060	2.56 ± 0.11	10.698 ± 0.014
34085	8	uhfr	30.238 ± 0.076	2.73 ± 0.11	10.479 ± 0.015
29009	1	cs23	0.81 ± 0.59	3.5 ± 2.0	10.81 ^{+0.20} _{-0.37}
29009	2	cs23	19.52 ± 0.18	3.53 ± 0.57	10.87 ^{+0.23} _{-0.53}
32249	1	cs12	14.03 ± 0.15	9.19 ± 0.22	11.715 ± 0.0091
30332	1	cs23	8.4 ± 1.5	6.01 ± 0.68	11.448 ^{+0.032} _{-0.033}
30332	2	cs23	24.35 ± 0.22	6.5 ± 2.0	11.499 ^{+0.058} _{-0.067}
31726	1	cs23	-7.60 ± 0.57	5.1 ± 1.9	11.33 ^{+0.12} _{-0.17}
31726	2	cs23	18.57 ± 0.78	11.15 ± 0.50	12.108 ^{+0.055} _{-0.063}
34816	1	cs12	8.61 ± 0.21	17.65 ± 0.28	12.086 ± 0.0062
26994	1	cs23	-4.70 ± 0.25	4.02 ± 0.43	11.68 ^{+0.10} _{-0.13}
26994	2	cs23	5.542 ± 0.047	5.35 ± 0.34	11.913 ^{+0.025} _{-0.027}
26994	3	cs23	2.60 ± 0.97	15.2 ± 1.9	11.78 ^{+0.11} _{-0.15}
30076	1	cs23	-20.40 ± 0.12	1.38 ± 0.88	11.31 ^{+0.29} _{-0.48}
30076	2	cs23	-14.01 ± 0.86	5.0 ± 1.1	11.70 ^{+0.10} _{-0.10}
30076	3	cs23	0.36 ± 0.77	4.4 ± 1.2	11.051 ^{+0.048} _{-0.051}
30076	4	cs23	13.50 ± 0.38	3.20 ± 0.89	11.330 ^{+0.072} _{-0.080}
30076	5	cs23	20.43 ± 0.72	1.10 ± 0.24	10.74 ^{+0.12} _{-0.16}
30076	6	cs23	26.82 ± 0.25	7.45 ± 0.73	11.703 ^{+0.032} _{-0.032}
30076	7	cs23	46.73 ± 0.79	5.85 ± 0.94	11.291 ^{+0.023} _{-0.024}

Table 3.2 (cont'd)

HD #	Component #	Instrument	v (km s ⁻¹)	b (km s ⁻¹)	$\log N$ (cm ⁻²)
30679	1	cs23	-14.5 ± 1.5	4.80 ± 0.43	11.816 ^{+0.021} _{-0.022}
30679	2	cs23	24.0 ± 3.8	7.1 ± 2.2	11.38 ^{+0.13} _{-0.18}
30963	1	cs23	-12.47 ± 0.092	13.07 ± 0.24	11.909 ^{+0.029} _{-0.031}
30963	2	cs23	14.4 ± 1.9	16.89 ± 0.71	12.206 ^{+0.042} _{-0.047}
28497	1	cs23	-26.41 ± 0.019	2.18 ± 0.82	11.06 ^{+0.15} _{-0.23}
28497	2	cs23	-11.3 ± 2.6	5.1 ± 1.0	11.858 ^{+0.045} _{-0.051}
28497	3	cs23	-10.2 ± 4.9	3.10 ± 0.69	11.27 ^{+0.26} _{-0.75}
28497	4	cs23	10.81 ± 0.20	4.9 ± 1.6	11.151 ^{+0.086} _{-0.099}
28497	5	cs23	20.53 ± 0.46	4.70 ± 0.46	11.18 ^{+0.11} _{-0.12}
28497	6	cs23	29.55 ± 0.67	3.00 ± 0.12	11.015 ^{+0.039} _{-0.040}

Table 3.3. Ca II ISM Fit Parameters Total Column Density Per Sightline

HD #	Components	Instrument	$\log N$ (cm^{-2})
33111		uhrf	<10.6
26574		cs23	<11.1
33904		uhrf	<10.4
27861		cs21	<11.1
31109		cs23	<11.5
29573		cs21	<11.4
33802		cs21	<10.5
32045		cs21	<11.7
30127		cs21	<11.1
34863		cs21	<11.0
32996		cs23	<10.8
28843	3	cs21	11.91 \pm 0.11
29554	2	cs23	11.534 $^{+0.061}_{-0.084}$
32468	2	cs21	11.63 \pm 0.19
28208	1	cs23	11.30 $^{+0.15}_{-0.63}$
29851	1	cs23	11.26 $^{+0.12}_{-0.27}$
30211	1	cs12	11.489 \pm 0.0094
34503	2	cs12	10.927 \pm 0.017
28980	1	cs23	11.31 $^{+0.10}_{-0.22}$
33949	3	uhrf	11.028 \pm 0.040
29248	1	cs12	11.213 \pm 0.0057
30050	2	cs23	12.39 $^{+0.06}_{-0.11}$
30535	2	cs23	12.496 $^{+0.019}_{-0.022}$
31512	2	cs23	11.40 $^{+0.08}_{-0.14}$
27563	1	cs23	11.18 $^{+0.11}_{-0.23}$
31089	2	cs23	12.510 $^{+0.015}_{-0.017}$
33224	2	cs23	11.80 $^{+0.08}_{-0.14}$
34085	8	uhrf	11.549 \pm 0.011
29009	2	cs23	11.14 $^{+0.13}_{-0.63}$
32249	1	cs12	11.715 \pm 0.0091
30332	2	cs23	11.775 $^{+0.033}_{-0.041}$
31726	2	cs23	12.175 $^{+0.047}_{-0.064}$
34816	1	cs12	12.086 \pm 0.0062
26994	3	cs23	12.277 $^{+0.043}_{-0.064}$
30076	7	cs23	12.253 $^{+0.043}_{-0.069}$
30679	2	cs23	11.952 $^{+0.036}_{-0.053}$
30963	2	cs23	12.384 $^{+0.029}_{-0.034}$
28497	6	cs23	12.15 $^{+0.04}_{-0.12}$

Table 3.4. NaI ISM Fit Parameters for Targets along the Past Solar Trajectory

HD #	Component #	Instrument	v (km s ⁻¹)	b (km s ⁻¹)	$\log N$ (cm ⁻²)
28763	1	cs21	15.491 ± 0.050	1.302 ± 0.040	10.759 ^{+0.0041}
30020	1	cs21	13.088 ± 0.065	0.492 ± 0.096	10.741 ^{+0.0045}
30020	2	cs21	20.810 ± 0.074	1.00 ± 0.36	10.906 ^{+0.053}
28843	1	cs21	-6.13 ± 0.23	0.58 ± 0.89	10.590 ^{+0.060}
28843	2	cs21	23.08 ± 0.21	4.78 ± 0.96	11.466 ^{+0.079}
28843	3	cs21	23.148 ± 0.049	0.78 ± 0.14	12.13 ^{+0.15}
29554	1	cs23	18.639 ± 0.045	0.482 ± 0.057	11.089 ^{+0.028}
29554	2	cs23	21.58 ± 0.11	1.43 ± 0.13	12.183 ^{+0.049}
32468	1	cs21	16.657 ± 0.090	1.61 ± 0.15	11.197 ^{+0.019}
32468	2	cs21	23.45 ± 0.24	1.96 ± 0.85	11.04 ^{+0.020}
28208	1	cs23	20.603 ± 0.048	2.05 ± 0.21	11.857 ^{+0.035}
29851	1	cs23	19.362 ± 0.051	1.53 ± 0.21	11.794 ^{+0.038}
30211	1	cs21	23.419 ± 0.030	0.83 ± 0.13	12.11 ^{+0.044}
34503	1	cs21	14.783 ± 0.045	0.63 ± 0.37	9.9560 ^{+0.016}
34503	2	cs21	22.741 ± 0.0067	1.130 ± 0.018	11.107 ^{+0.20}
34503	3	cs21	22.487 ± 0.035	5.95 ± 0.14	10.889 ^{+0.037}
28980	1	cs23	20.29 ± 0.14	1.91 ± 0.70	11.40 ^{+0.040}
33949	1	cs21	16.474 ± 0.067	1.622 ± 0.064	10.921 ^{+0.0058}
33949	2	cs21	22.755 ± 0.052	0.337 ± 0.025	11.330 ^{+0.021}
33949	3	cs21	23.772 ± 0.067	2.10 ± 0.13	11.320 ^{+0.022}
30050	1	cs23	23.912 ± 0.024	2.21 ± 0.22	12.33 ^{+0.10}
28377	1	cs23	-28.11 ± 0.70	4.51 ± 0.36	10.853 ^{+0.031}
28377	2	cs23	13.40 ± 0.46	2.30 ± 0.36	10.777 ^{+0.093}
30535	1	cs23	-2.45 ± 0.51	7.55 ± 0.93	11.207 ^{+0.021}
30535	2	cs23	19.33 ± 0.17	5.82 ± 0.22	11.449 ^{+0.047}
30535	3	cs23	23.22 ± 0.20	1.18 ± 0.37	10.918 ^{+0.029}
31512	1	cs23	-13.45 ± 0.25	1.62 ± 0.80	10.29 ^{+0.0095}
31512	2	cs23	-0.370 ± 0.25	2.43 ± 0.84	10.462 ^{+0.084}
31512	3	cs23	19.7 ± 1.3	8.41 ± 2.0	10.90 ^{+0.10}
31512	4	cs23	22.80 ± 0.36	0.49 ± 0.87	11.60 ^{+0.15}
27563	1	cs23	-6.36 ± 0.51	5.8 ± 3.7	10.54 ^{+0.24}
27563	2	cs23	19.19 ± 0.22	0.48 ± 0.19	12.11 ^{+0.26}
27563	3	cs23	18.893 ± 0.094	2.53 ± 0.67	11.59 ^{+0.36}
31089	1	cs23	17.006 ± 0.039	1.73 ± 0.20	11.832 ^{+0.14}
31089	2	cs23	17.4 ± 2.0	11.67 ± 0.30	11.495 ^{+0.27}
31089	3	cs23	22.58 ± 0.37	2.40 ± 0.75	11.04 ^{+0.039}
33224	1	cs23	15.11 ± 0.12	1.00 ± 0.15	11.729 ^{+0.043}
33224	2	cs23	17.512 ± 0.067	4.84 ± 0.12	11.815 ^{+0.081}
34085	1	cs12	0.5458 ± 0.054	3.524 ± 0.066	10.924 ± 0.095
34085	2	cs12	9.4294 ± 0.075	5.23 ± 0.17	10.972 ± 0.011
34085	3	cs12	18.941 ± 0.011	2.310 ± 0.019	11.263 ± 0.0030
34085	4	cs12	24.450 ± 0.021	1.73 ± 0.48	10.815 ± 0.0099
34085	5	cs12	30.46 ± 0.10	4.13 ± 0.14	10.753 ± 0.011
29009	1	cs23	0.9 ± 1.0	5.8 ± 1.2	10.658 ^{+0.015}
29009	2	cs23	18.3 ± 1.0	1.49 ± 0.72	10.76 ^{+0.016}
29009	3	cs23	22.36 ± 0.21	1.80 ± 0.29	11.685 ^{+0.25}
28262	1	cs23	20.085 ± 0.048	2.37 ± 0.21	12.223 ^{+0.67}
32249	1	cs12	18.484 ± 0.017	1.541 ± 0.031	11.869 ± 0.0052
32249	2	cs12	22.697 ± 0.045	0.861 ± 0.081	11.152 ± 0.017
30332	1	cs23	5.79 ± 0.50	8.3 ± 1.0	11.134 ^{+0.044}
30332	2	cs23	24.23 ± 0.27	2.33 ± 0.45	11.85 ^{+0.049}
30332	3	cs23	27.49 ± 0.21	0.318 ± 0.093	11.441 ^{+0.11}
31726	1	cs23	-5.63 ± 0.17	4.19 ± 0.49	10.961 ^{+0.13}
31726	2	cs23	8.36 ± 0.64	5.09 ± 0.44	11.400 ^{+0.060}
					11.400 ^{+0.069}
					11.400 ^{+0.027}
					11.400 ^{+0.029}
					11.400 ^{+0.045}
					11.400 ^{-0.050}

Table 3.4 (cont'd)

HD #	Component #	Instrument	v (km s ⁻¹)	b (km s ⁻¹)	$\log N$ (cm ⁻²)
31726	3	cs23	14.543 ± 0.012	1.04 ± 0.51	11.82 ^{+0.12} _{-0.17}
31726	4	cs23	21.2 ± 2.3	8.9 ± 1.6	11.33 ^{+0.12} _{-0.16}
34816	1	cs12	23.208 ± 0.066	2.14 ± 0.11	11.184 ± 0.016
26994	1	cs23	-5.44 ± 0.24	1.71 ± 0.49	11.393 ^{+0.036} _{-0.039}
26994	2	cs23	3.22 ± 0.33	0.60 ± 0.12	11.97 ± 0.38
26994	3	cs23	5.00 ± 0.26	4.13 ± 0.34	12.092 ^{+0.061} _{-0.072}
32612	1	cs23	-15.5 ± 1.1	2.4 ± 2.4	10.42 ^{+0.11} _{-0.11}
32612	2	cs23	-4.1 ± 1.8	4.57 ± 0.97	10.52 ^{+0.10} _{-0.11}
32612	3	cs23	8.01 ± 0.35	6.12 ± 0.86	11.099 ^{+0.064} _{-0.073}
32612	4	cs23	15.86 ± 0.20	1.65 ± 0.44	11.175 ^{+0.068} _{-0.072}
32612	5	cs23	21.14 ± 0.45	1.64 ± 0.46	11.13 ^{+0.13} _{-0.18}
32612	6	cs23	26.89 ± 0.28	3.65 ± 0.45	11.15 ^{+0.11} _{-0.15}
30076	1	cs23	-20.29 ± 0.18	1.56 ± 0.18	10.980 ^{+0.037} _{-0.065}
30076	2	cs23	-14.91 ± 0.45	4.96 ± 0.71	11.259 ^{+0.067} _{-0.079}
30076	3	cs23	-0.3 ± 3.1	4.9 ± 2.8	10.34 ^{+0.24} _{-0.32}
30076	4	cs23	9.69 ± 0.94	3.3 ± 1.9	10.751 ^{+0.086} _{-0.095}
30076	5	cs23	22.22 ± 0.12	0.616 ± 0.051	12.218 ^{+0.037} _{-0.041}
30076	6	cs23	24.61 ± 0.40	4.86 ± 0.41	12.089 ^{+0.024} _{-0.024}
30679	1	cs23	-19.04 ± 0.16	2.4 ± 1.2	11.059 ^{+0.096} _{-0.12}
30679	2	cs23	-11.49 ± 0.37	4.54 ± 0.43	11.335 ^{+0.019} _{-0.019}
30679	3	cs23	15.37 ± 0.82	5.25 ± 0.31	10.853 ^{+0.030} _{-0.032}
30679	4	cs23	22.931 ± 0.022	2.6 ± 1.0	11.072 ^{+0.069} _{-0.074}
30963	1	cs23	-24.2 ± 1.8	1.5 ± 1.1	10.268 ^{+0.050} _{-0.050}
30963	2	cs23	-13.64 ± 0.53	5.25 ± 0.28	10.727 ^{+0.074} _{-0.090}
30963	3	cs23	11.56 ± 0.33	18.97 ± 0.77	11.503 ^{+0.069} _{-0.082}
30963	4	cs23	21.411 ± 0.026	1.56 ± 0.16	11.433 ^{+0.038} _{-0.041}
27436	1	cs23	-39.1 ± 2.9	11.8 ± 2.3	11.201 ^{+0.093} _{-0.10}
27436	2	cs23	-12.3 ± 5.9	17. ± 10.	11.46 ^{+0.38} _{-1.1}
27436	3	cs23	17.3 ± 7.5	11.0 ± 6.5	11.30 ^{+0.36} _{-0.68}
27436	4	cs23	17.375 ± 0.055	2.39 ± 0.40	12.24 ^{+0.10} _{-0.11}
28497	1	cs21	-26.21 ± 0.080	2.03 ± 0.52	10.767 ^{+0.074} _{-0.089}
28497	2	cs21	-15.3 ± 1.6	3.75 ± 0.71	10.74 ^{+0.31} _{-0.50}
28497	3	cs21	-12.15 ± 0.13	1.8 ± 1.1	10.85 ^{+0.19} _{-0.33}
28497	4	cs21	-6.909 ± 0.057	2.49 ± 0.51	11.23 ^{+0.11} _{-0.14}
28497	5	cs21	-1.2 ± 1.7	3.34 ± 0.55	10.62 ^{+0.16} _{-0.27}
28497	6	cs21	6.494 ± 0.054	0.21 ± 0.34	10.66 ^{+0.14} _{-0.22}
28497	7	cs21	11.09 ± 0.44	6.32 ± 0.45	11.357 ^{+0.044} _{-0.049}
28497	8	cs21	21.57 ± 0.27	0.38 ± 0.24	10.524 ^{+0.044} _{-0.049}
28497	9	cs21	23.5 ± 1.0	8.1 ± 1.2	11.045 ^{+0.062} _{-0.073}
28497	10	cs21	31.022 ± 0.045	0.94 ± 0.11	10.710 ^{+0.0070} _{-0.0071}

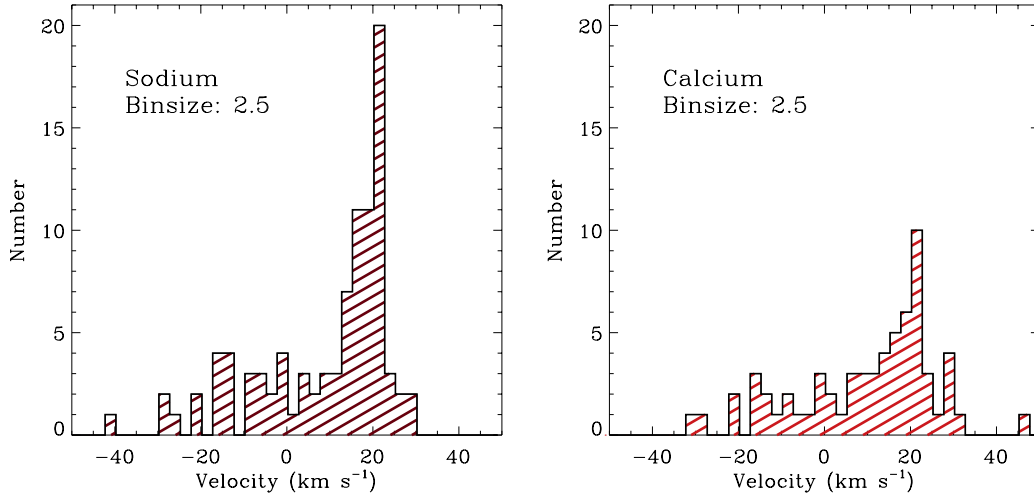


Figure 3.20: Distribution of cloud velocities from the sodium (left) and calcium (right) data. Both data sets reveal a proportionally large spike near $\sim 20 \text{ km s}^{-1}$. Median velocity for the entire sodium data set is 17.3 km s^{-1} , and 15.2 km s^{-1} for calcium.

3.4 Histograms

To get a sense of the overall characteristics of the ISM clouds in our Sun’s recent history, we construct histograms of the three parameters of our clouds for the sodium and calcium data: component velocity, Doppler parameter, and log column density.

Velocity Histograms

The left side of Figure 3.20 is a histogram of the velocities for the entire set of individual sodium components and the same plot for the calcium data is on the right. Both the sodium and calcium component velocities range from approximately -40 km s^{-1} to $+40 \text{ km s}^{-1}$. Calcium components tended to be broader (higher temperatures) or blends of components too weak to resolve individually, this could explain why there are fewer overall components in the calcium his-

Table 3.5. NaI ISM Fit Parameters Total Column Density Per Sightline

HD #	Number of Components	Instrument	log N (cm ⁻²)
33111		uhrf	<9.9
30743		cs21	<10.3
26574		cs23	<10.8
33904		cs12	<10.8
27861		cs21	<10.2
31109		cs23	<10.5
29573		cs21	<10.2
33802		cs21	<10.0
32964		cs23	<10.4
32045		cs21	<10.7
30127		cs21	<10.2
34863		cs21	<10.5
27925		cs23	<10.5
32996		cs23	<10.2
29173		cs23	<10.2
28763	1	cs21	10.759 ^{+0.0041} _{-0.0042}
30020	2	cs21	11.132 ^{+0.030} _{-0.036}
28843	3	cs21	12.22 ^{+0.11} _{-0.23}
29554	2	cs23	12.216 ^{+0.043} _{-0.055}
32468	2	cs21	11.428 ^{+0.042} _{-0.062}
28208	1	cs23	11.857 ^{+0.034} _{-0.040}
29851	1	cs23	11.794 ^{+0.042} _{-0.052}
30211	1	cs21	12.11 ^{+0.14} _{-0.27}
34503	3	cs21	11.331 ^{+0.0084} _{-0.0090}
28980	1	cs23	11.395 ^{+0.093} _{-0.16}
33949	3	cs21	11.704 ^{+0.017} _{-0.019}
30050	1	cs23	12.326 ^{+0.091} _{-0.13}
28377	2	cs23	11.118 ^{+0.048} _{-0.070}
30535	3	cs23	11.720 ^{+0.020} _{-0.024}
31512	4	cs23	11.72 ^{+0.16} _{-0.43}
27563	3	cs23	12.23 ±0.38
31089	3	cs23	12.041 ^{+0.034} _{-0.043}
33224	2	cs23	12.075 ^{+0.016} _{-0.019}
34085	5	cs12	11.684 ±0.0050
29009	3	cs23	11.769 ^{+0.040} _{-0.083}
28262	1	cs23	12.223 ^{+0.068} _{-0.085}
32249	2	cs12	11.945 ±0.0052
30332	3	cs23	12.051 ^{+0.064} _{-0.090}
31726	4	cs23	12.083 ^{+0.065} _{-0.11}
34816	1	cs12	11.184 ±0.016
26994	3	cs23	12.38 ±0.13
32612	6	cs23	11.786 ^{+0.042} _{-0.062}
30076	6	cs23	12.510 ^{+0.021} _{-0.024}
30679	4	cs23	11.716 ^{+0.027} _{-0.034}
30963	4	cs23	11.820 ^{+0.035} _{-0.046}
27436	4	cs23	12.376 ^{+0.083} _{-0.22}
28497	10	cs21	11.936 ^{+0.036} _{-0.059}

togram. The high frequency of components found around 22 or 23 km s^{-1} in both sets of data suggests that there is a large amount of material nearby moving away from us at that speed. If there is a cloud nearby, it would likely be seen in absorption towards all stars at increasing distances.

Doppler Parameter Histograms

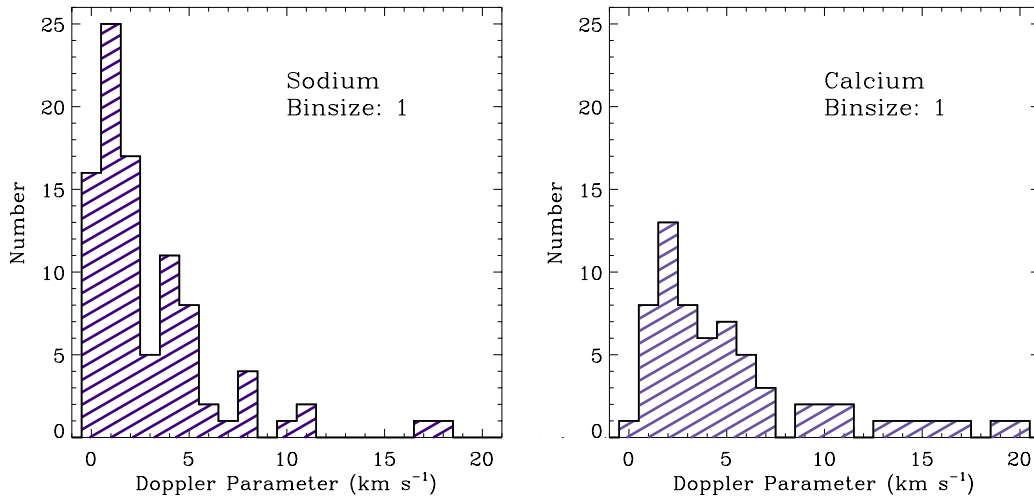


Figure 3.21: Distribution of Doppler parameters for the complete sample of absorption components as determined from the fits. Median Doppler parameter for the sodium data is 2.3 km s^{-1} and for the calcium 4.4 km s^{-1} .

The preponderance of ISM components moving at 23 km s^{-1} are typically narrow, cool components, which is why we see a larger number of ISM components with Doppler parameters of 3 km s^{-1} or less. The ionization potential of sodium means it probes slightly cooler temperatures, which is another reason why we see more narrow components in the sodium data. The high Doppler parameter tail in both the sodium and calcium histograms are a reflection of our inability to resolve the weakest components in the ISM. As a result, multiple weak absorbers that are likely present are blended into broad shallow components. While such blends may

mask the true number of absorbers, the total column density remains the same.

Column Density Histograms

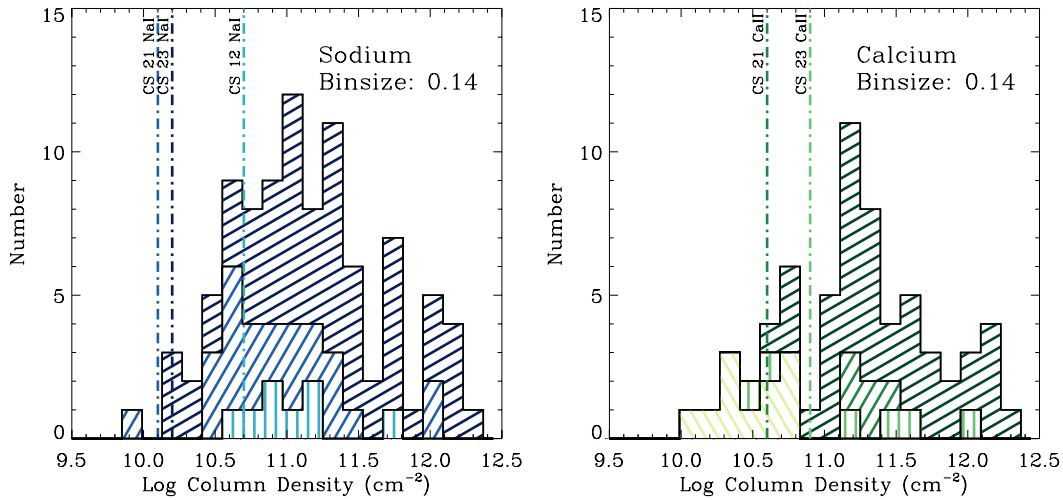


Figure 3.22: Column density distribution for the sodium and calcium data sets, color-coded by instrument. Median sodium column density is 11.2 cm^{-2} and 11.3 cm^{-2} for calcium. Vertical lines depict each instrument’s sensitivity limit.

Figure 3.22 shows the frequency of observed individual component column densities determined from our fitting routine. Distinction here is made between observations with different instrument resolutions since each suffers a different sensitivity limit, shown by the vertical dashed lines named for each instrument. The number of weak absorbers is likely underestimated due to our inability to resolve the shallow, broad components into the more likely small individual absorption profiles.

3.5 Apparent Optical Depth

Savage & Sembach (1991) developed a method for analyzing interstellar absorption by converting absorption line profiles into profiles of apparent optical

depth, $\tau_a(v)$, and apparent column density, $N_a(v)$, per unit velocity. The value of the method lies in its ability to quickly provide a diagnostic of the velocity structure of some absorbing medium.

Apparent optical depth as a function of wavelength is obtained from Equation 3.1 where $I_0(\lambda)$ is our normalized flux continuum (1 in our case), and $I_{obs}(\lambda)$ is the absorption line profile for a particular observation.

$$\tau_a(\lambda) = \ln \left[\frac{I_0(\lambda)}{I_{obs}(\lambda)} \right] \quad (3.1)$$

Apparent optical depth is different from true optical depth in that the apparent optical depth has been blurred by the resolution of the instrument used to take the data. However, the apparent optical depth is a good approximation of the true optical depth when the instrument resolution is very high, the continuum is well defined, and the measurements have a high signal to noise ratio. When these conditions are met, $\tau_a(\lambda) \approx \tau(\lambda)$, and we can make use of the relation between true optical depth and column density:

$$\tau(\lambda) = \frac{\pi e^2}{m_e c^2} f \lambda^2 N(\lambda) \quad (3.2)$$

Total column density can be found from $N = \int N(\lambda) d\lambda$ and expressing total column density as a function of velocity, we can solve for Equation 3.2 for $N(v)$ and integrating, giving:

$$N = \frac{m_e c}{\pi e^2 f \lambda} \int \ln \frac{I_0(v)}{I(v)} dv \quad (3.3)$$

Where m_e is the mass of an electron, f is the transition oscillator strength, c is the speed of light, and λ is wavelength in Ångstroms. Apparent optical depth per

unit velocity as a function of distance is plotted in Figures 3.23 for the sodium data and 3.24 for the calcium data. For these plots, the sodium and calcium column densities have been translated into hydrogen column densities, this process will be explained in the next chapter.

In the sodium apparent optical depth plot (Figure 3.23), we see the edge of the Local Bubble at roughly 120 parsecs, shortly thereafter there is a strong absorption feature at $\sim 23 \text{ km s}^{-1}$ which is frequently seen in absorption profiles at increasing distances. This suggests that there is a cloud near the edge of the Local Bubble taking up a significant portion of the stellar sample area, that is why it is seen in absorption profiles at greater distances. Occasionally this component disappears altogether, such as the absorption profile seen at around 375 parsecs where there is no absorption around 23 km s^{-1} , suggesting that the cloud is not present along this particular sight line.

Components seen in the calcium apparent optical depth plot (Figure 3.24) are much broader since calcium probes slightly higher temperatures. Similar to the sodium data, calcium has a number of absorption components near 23 km s^{-1} , but also a few at negative velocities.

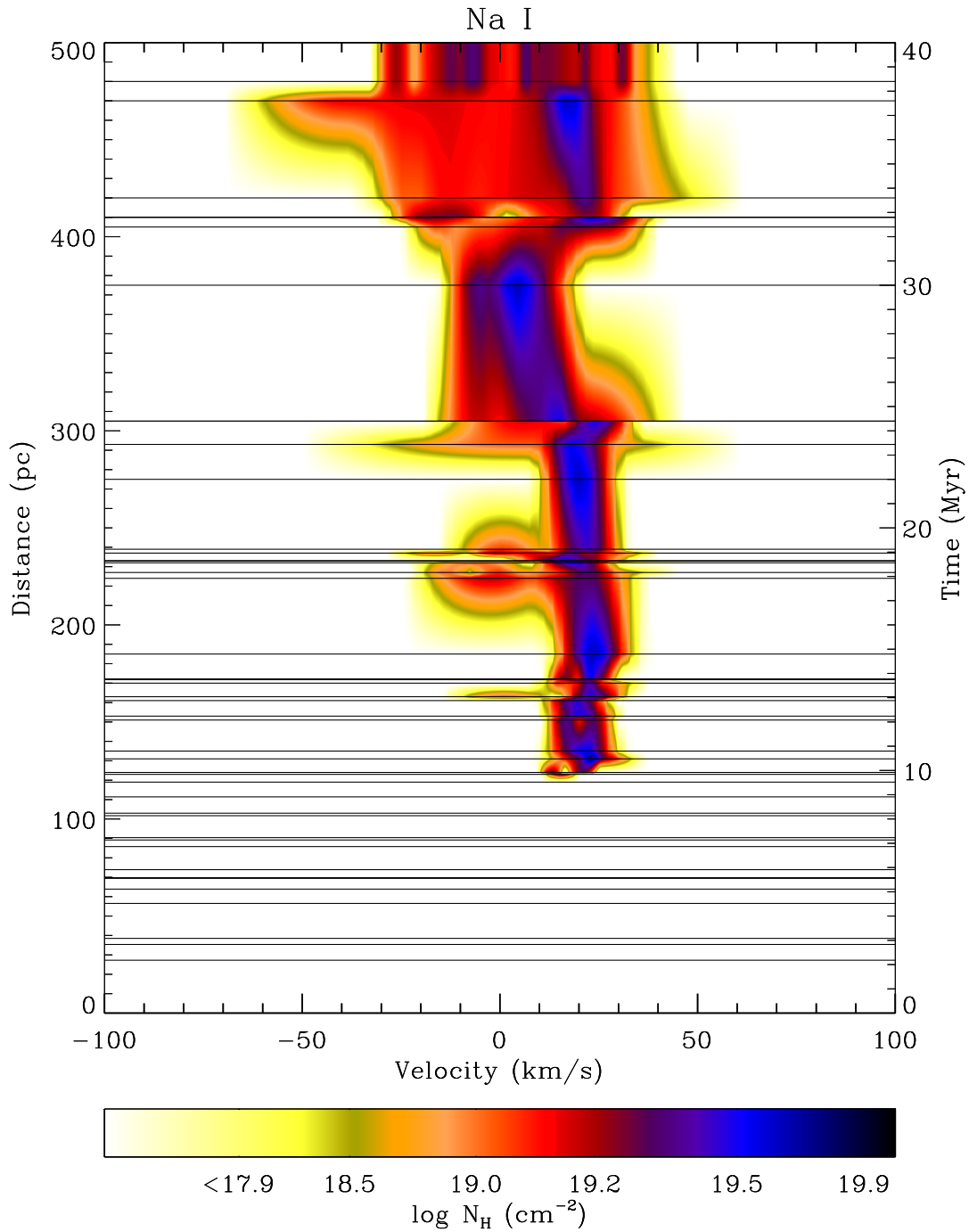


Figure 3.23: Apparent optical depth profile determined from the sodium data plotted at the distance to each sightline, marked by black horizontal bars. Distance to targets is plotted along the left y-axis and timeline of interaction based on current values of the solar motion is plotted along the right y-axis.

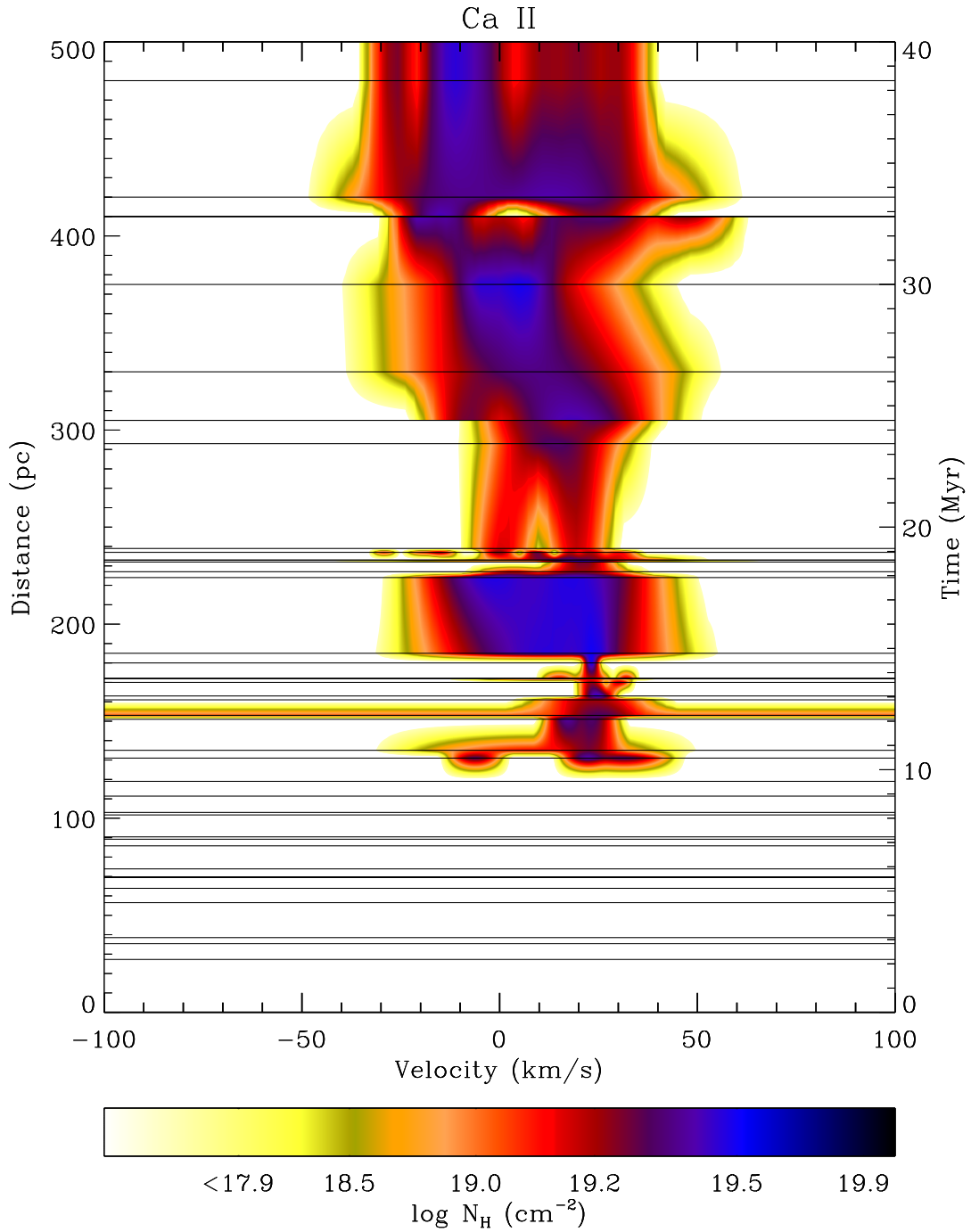


Figure 3.24: Same as Figure 3.23 plotted for the calcium data.

Chapter 4

Results

The apparent optical depth profiles in the previous chapter (Figures 3.23 and 3.24) were a first attempt at a visual representation of the overall data set. Next, taking the total column densities listed in Tables 3.3 and 3.5, we can create a column density profile and subsequently a volume density profile which will allow us to place distance constraints on the locations of individual ISM clouds. In Chapter 5, we will use the ISM cloud parameters derived here to explore their potential influence on the size and shape of our heliosphere. Ultimately we will discuss possible implications that an encounter with these ISM clouds will have for the GCR flux at 1 AU.

4.1 Column Density Profile

Using the column density data in Tables 3.3 and 3.5, I have plotted total column density as a function of distance to create a column density profile, see Figures 4.1 and 4.2. The closest measurements of ISM sample the truly “local” ISM: relatively low-density, high temperature cloudlets located within the Local Bubble. Our measurements of sodium and calcium are insensitive to these weak column densities and as a result, our observations of the ISM within roughly 120 parsecs provide only upper limits on column density.

The region of upper limits is roughly the same for both the sodium and cal-

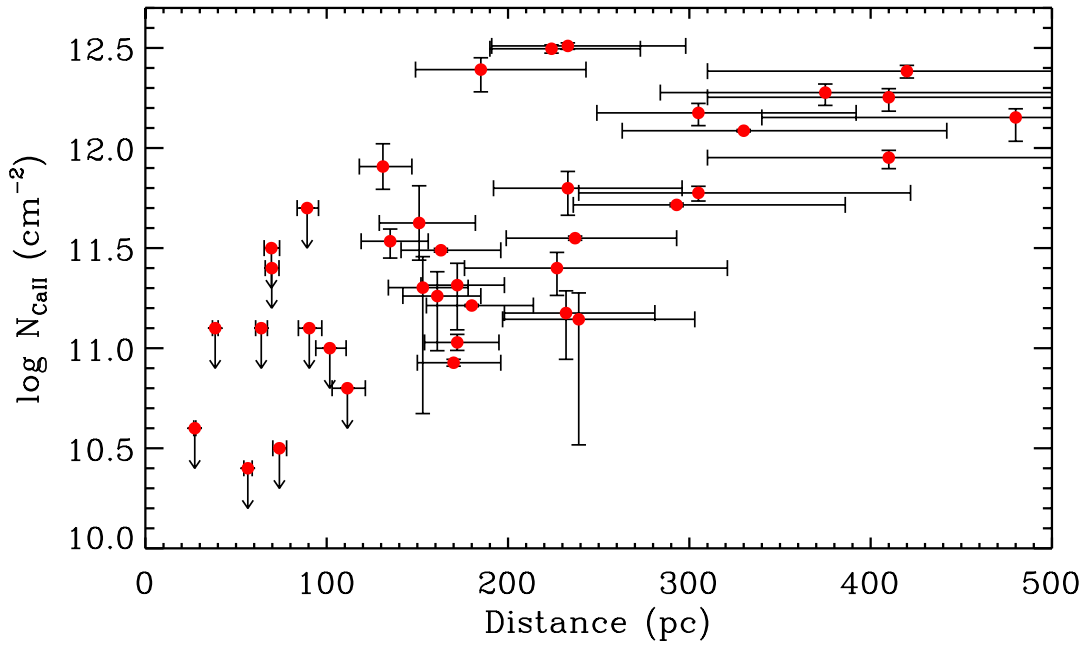


Figure 4.1: Calcium column density profile as a function of distance. Calcium has significantly more scatter in the measurements of column density than the sodium data, however we do see the sudden encounter of high column densities found between 100 and 200 parsecs from the Sun, which is reflected in the sodium data as well. Errors in distance are from *Hipparcos* parallax measurements. Data is shown for 49 stars between 25 and 500 parsecs, median distance between stars in 5 parsecs. 11 ISM absorption measurements inside the Local Bubble resulted in column density upper limits.

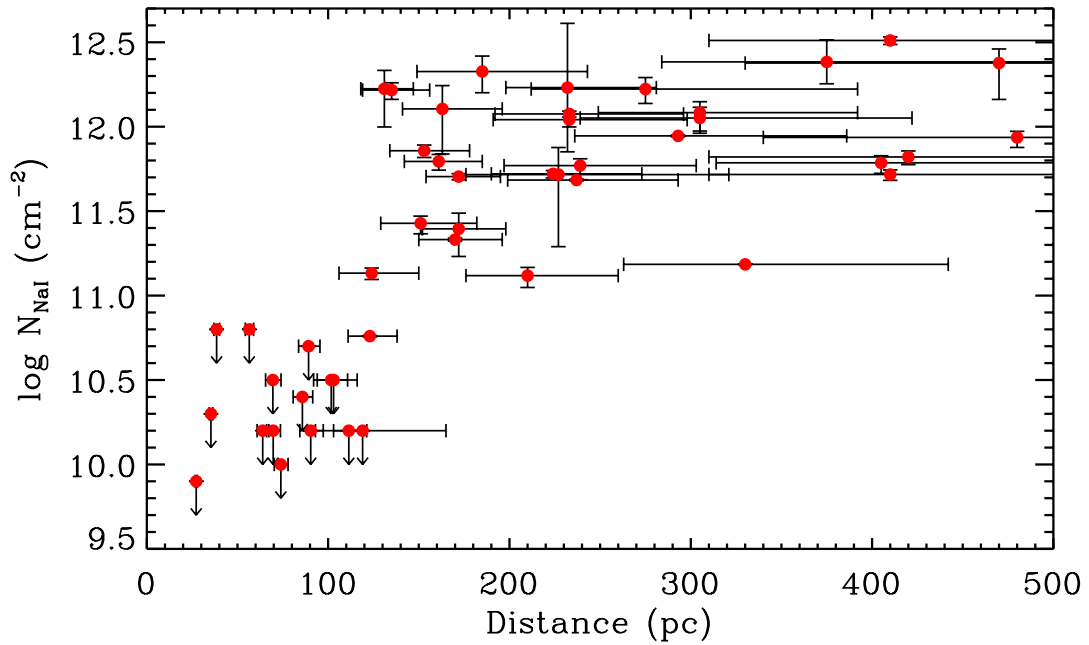


Figure 4.2: Sodium column density profile as a function of distance. First detection of cold, dense ISM lies at roughly 120 parsecs, consistent with measurements made by Lallement et al. (2003). At this distance we see a sharp sudden increase in NaI column density corresponding to the edge of the Local Bubble. This increase is also seen in the calcium density profile though not as dramatically. Errors in distance are from *Hipparcos* parallax measurements. Data is shown for 49 stars between 25 and 500 parsecs, median distance between stars in 5 parsecs. 15 ISM absorption measurements inside the Local Bubble resulted in column density upper limits.

cium observations. At around 120 to 130 parsecs, we see a sharp sudden increase in column density which corresponds to the edge of the Local Bubble. Our measurements of the distance to this edge are in agreement with Lallement et al. (2003) who did an all sky survey of interstellar neutral sodium out to a distance of 500 parsecs. This sharp rise is most apparent in the sodium column density profile but is also seen in the calcium data. Often the calcium observations have much lower S/N, this is one possible explanation for the greater amount of scatter and relatively larger error bars on calcium column density. The error in the distance measurements are from *Hipparcos* parallax measurements, for this reason, the error bars tend to grow with distance as parallax becomes more difficult to measure.

The spread in column densities at any given distance might be explained in a couple of different ways and is likely an indication that we are observing small scale structure within the ISM. The scatter in the measurements of column density most likely arise from the fact that we are not looking along one line of sight, instead we are observing a volume of stars in a cone of about 20° in diameter. Figure 4.3 illustrates the angular distribution of our sight lines. Stars on the left side of our distribution could reveal some absorption from an intervening cloud that might not be present in sight lines towards stars on the right side of our distribution. This is why the total column density appears to decrease with distance occasionally. This angular separation of sight lines can also be used to explain the apparent disappearing and reappearing of absorbing components in the apparent optical depth profiles presented in the previous chapter (Figures 3.23 and 3.24).

To investigate the degree with which spatial separation might be affecting our data, we take two approaches: first we narrow our cone of sample stars to smaller regions immediately surrounding the path of the Sun's historical trajectory, sec-

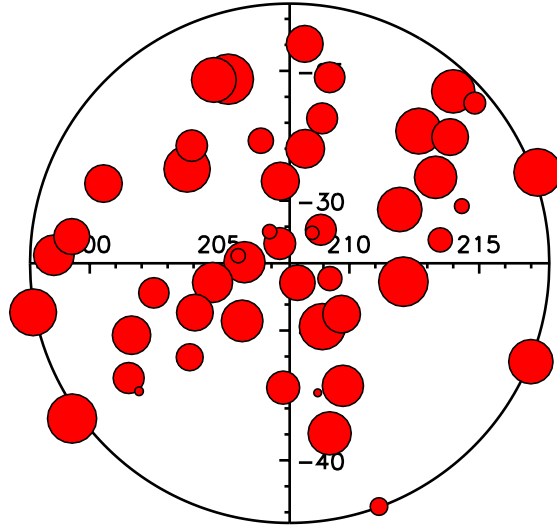


Figure 4.3: Angular distribution of the complete sample of stars, projected on the sky. Size of circle is inversely proportional to distance. The angular separation between two stars in some cases could be as great as 50 parsecs.

only we explore the variation in total column densities in distinct distance regions along the historical path of the Sun.

4.1.1 Cone Restriction

To decrease the possibility of probing many different clouds, we can narrow our sample of stars to only those that are in a smaller cone centered on the direction of the solar motion's past (Galactic longitude: $l_0 = 207.70^\circ$ and galactic latitude: $b_0 = -32.41^\circ$). If we were to restrict our cone to smaller angles, we might see this spread in column densities tighten up since we would be sampling ISM with stellar sight lines that are not as spatially separated. We split the cone up into 3 annuli of increasing radii: instead of considering all stars within 10 degrees of l_0, b_0 we limited our measurements to sight lines within 6.6° and finally 3.3° of l_0, b_0 . Figure 4.4a shows a map of these angular bins. Each sightline is color-coded according to the angular region it belongs to. Figure 4.4b shows the total

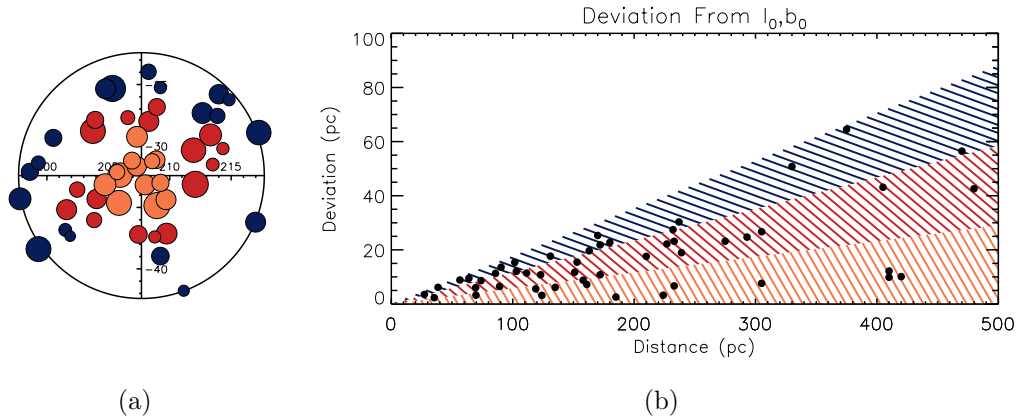


Figure 4.4: (a) Sight lines colored according to angular bin membership. Distance to star indicated by size of symbol. (b) Sight lines plotted as total spatial separation from l_0, b_0 as a function of distance. Stars within 3.3° of the center belong to the orange bin, stars between 3.3° and 6.6° belong to the red bin, and stars greater than 6.6° away from the center belong to the blue bin.

deviation from l_0, b_0 as a function of distance and each shaded region is colored to match the corresponding angular bin.

In Figure 4.5 we have re-plotted the column density profiles with each data-point color-coded according to the angular bin it resides in. In some regions the orange dots (corresponding to the smallest angular bin) show less variation in column densities while at other distances the scatter is still quite large. Reviewing the sodium data in particular: between 200 and 300 parsecs, the orange data points exhibit the smallest amount of column density variation, but between 400 and 500 parsecs, they show the greatest amount of variation.

These plots serve to support our suspicion that we are seeing small scale structure outside the Local Bubble, clouds on the order of a few tens of parsecs across. Clouds of this size could explain why a measurement of high column density could be immediately followed by another measurement that is a full order of magnitude lower in column density, but only 10 parsecs farther beyond in distance. The

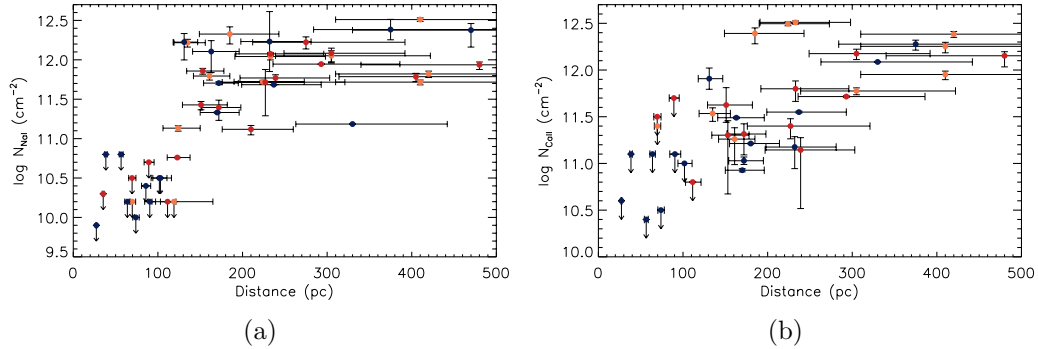


Figure 4.5: Color coding of our column density measurements for sodium (a), and calcium (b), according to the angular regions set up and described in Figure 4.4.

physical separation of these two sight lines might be as great as 50 parsecs.

4.1.2 Distance Slices

Another way to explore possible causes for the large amount of variation in column density is to make cuts in distance rather than angular separation. To accomplish this, we began at the edge of the Local Bubble and made cuts in distance starting at 150, 200, 250 and 350 parsecs for the sodium data. These distance ranges were chosen around specific sight lines that exhibited large differences in column density. Our hopes were that plots of column densities at different distance slices would reveal trends in column density across a slice, which could represent an intervening cloud at some distance. Our last two distance bins were much larger than the others because they both had significantly fewer sight lines.

Plots of each distance slice, the sight lines within, and their column densities are shown in Figure 4.6. In some distance regions such as the one containing stellar sources between 250 and 350 parsecs, we do see a gradual increase in column density from the bottom left to the upper right region of the plot.

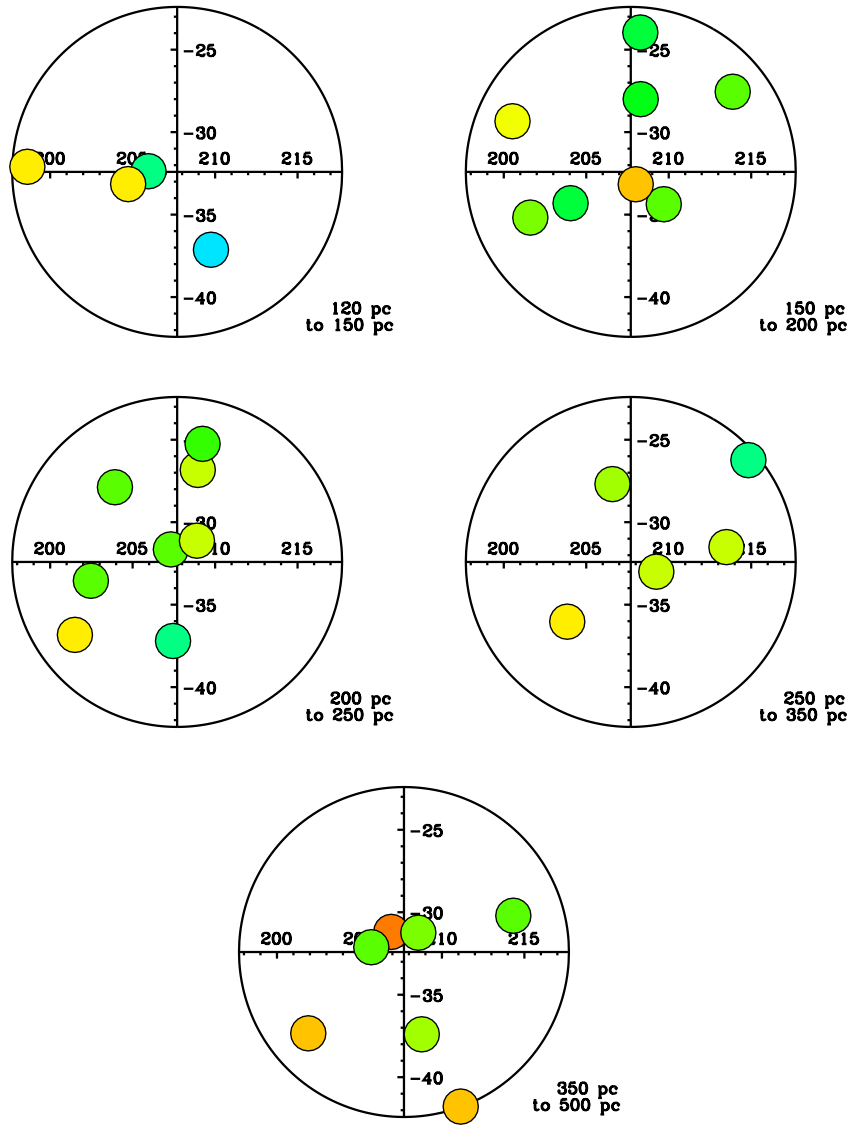


Figure 4.6: Distance bins showing the spatial variation in sodium column density across the cone containing our stellar sight lines. Each circle corresponds to a star residing within the distance bin indicated to the lower right of each plot. Column density starts out at 10.759 cm^{-2} for the blue symbol in the nearest distance bin, increasing towards a high column density of 12.51 cm^{-2} for the dark orange dot near the center of the furthest distance bin.

4.2 Developing a Monotonic Profile

Before we can make any calculations concerning the density of the ISM the Sun has passed through in the past 40 Myrs, corresponding heliosphere size and its effects on the cosmic ray flux at 1 AU, our column density profile needs to be converted into a volume density profile. A volume density profile will allow us to quantify the regions over which large increases in column density occur. Increases like this should correspond to an encounter with large amounts of absorbing medium. The volume density profile will also give us more information about regions where there is relatively little increase in column density.

If we are comparing the absorption profile of two adjacent stars, and we see an absorption feature in the data for the more distant star which was absent from the star immediately preceding it, we can then make estimates on the location of the absorbing material since it necessarily needs to reside between the two stars. If however, we see no significant increase in absorbing material between two adjacent stars, we can assume that not much material is present between the two stars. To make this calculation, first we need a model to quantify the increase in total column density as a function of distance. This fit is required to be monotonically increasing and has to start out below our column density limits inside the Local Bubble. Two approaches were taken to develop a fit to the data.

4.2.1 Boltzmann Method

The Boltzmann fit is a sigmoidal function with a linear x scale. Sigmoids are used to describe the progression of a variety of natural processes from low starting values that increase to a higher maximum values with time (Simmons 1996). There

seems to be no physical reason that the increase in column density with distance should behave like a sigmoid, however the data has a similar appearance to a Boltzmann function: starting from the low upper-limits on column density inside the Local Bubble, through the sharp increase in column density seen at a distance of ~ 120 parsecs, to somewhat of a plateau of high column densities from about 300 parsecs and beyond. Fortunately for our purposes, the Boltzmann fit is defined to be monotonically increasing, and is not entirely unphysical since we want to describe the overall trend in increasing column densities. However this method will be insensitive to sharp increases in density due to the possible occurrence of small individual clouds.

The IDL routine `amoeba` was used to fit a series of Boltzmann functions to the data. `amoeba` is a downhill simplex method for minimizing a function. In our case, the function we wanted to minimize was a χ^2 evaluation of the quality of the Boltzmann fit to the data. Equation 4.1 is the form of the fit used for this process. A_1 is the initial value or the lower horizontal asymptote, A_2 is the final value or the upper horizontal asymptote, x_0 is the center of the rise (or point of inflection), and dx is the width of the inflection area. `amoeba` was fed initial guesses for all four parameters, these guesses were made from visual inspection of the profiles, but `amoeba` was given large ranges over which each parameter could vary to arrive at whatever was deemed to be the best fit based on the minimization of χ^2 . One of the free parameters, A_1 , the lower limit, was set to be below our Local Bubble upper limit values, and not allowed to vary. Each subsequent additional Boltzmann's A_1 was automatically set to the previous Boltzmann's A_2 .

$$y = \frac{A_1 - A_2}{1 + e^{\frac{x-x_0}{dx}}} + A_2. \quad (4.1)$$

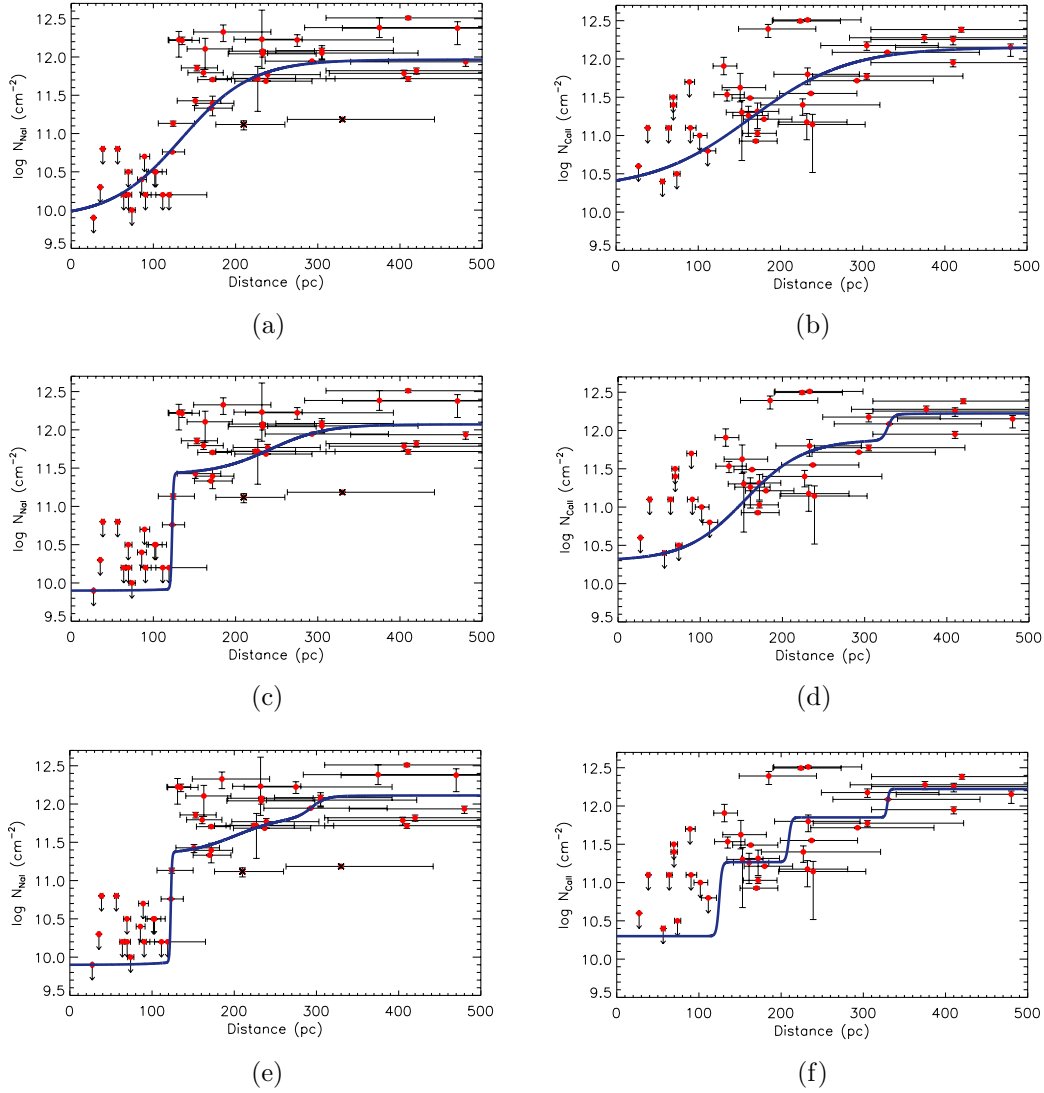


Figure 4.7: The Boltzmann fits to the sodium and calcium data. Plots (a) and (b) show the sodium and calcium data respectively with one Boltzmann fit. Plots (c) and (d) show the addition of another Boltzmann fit to the same data. Plots (e) and (f) show 3 Boltzmann functions fit to the data. Both the 2 and 3 Boltzmann fits failed the F-test, so the one Boltzmann fit is the most statistically significant solution to the data for both sodium and calcium.

When trying to fit a Boltzmann function to the sodium data (Figure 4.7, plots (a), (c) and (e)), there were two relatively low column density, high S/N data points that were well below the majority of the other measurements (HD28377 at 210 pc and HD34816 at 330 pc). These two points were forcing `amoeba` to make a fit that passes very near the column densities at these points, because fitting these high-quality points significantly improved the quality of the fit, even though the majority of the column density measurements were around an order of magnitude greater. With the inclusion of these points, we felt that `amoeba` was unable to return a fit that we felt accurately represented the overall trend of increasing column density. For this reason they were excluded from the fitting process, and marked with two black x's in the sodium plots of Figure 4.7. This allowed us to obtain much better fits.

Initially each data set was fit with one Boltzmann function, then additional functions were added to see if we could significantly increase the quality of the fit while abiding by the rules of the F-test. The results of the fitting routine for the Boltzmann fits to the sodium and calcium data are shown in Figure 4.7 for 1, 2 and 3 Boltzmann functions. For both the sodium and calcium data, each addition of a second or third Boltzmann did not significantly improve our model.

While the Boltzmann function might adequately represent the overall trend of increasing column density, which might be more clearly seen in a less angularly separated, more densely populated sample, our data seems to be dominated by the effects of spatial separation and small scale variation.

4.2.2 Brute Force Method

Since there is no obvious physical motivation for the increase in column density to behave analytically, we also employed a more brute force method of creating a monotonic fit.

An array of evenly spaced column densities were created to span the entire range of column densities in each data set. This array of column density values was set to increase in log steps of 0.12 cm^{-2} . A distance array was also created, ranging from 120 parsecs (corresponding to the rough distance of first detection of ISM absorption at the edge of the Local Bubble) to 500 parsecs and set to increase in steps of 10 parsecs. Essentially what we have created at this point is a grid of column densities and distances that we can plot over our column density profiles.

Using a series of nested `for` loops, we begin at the first distance value and start fitting possible data points for our column density array to the first distance value on our grid. After the program has run through all possible values of column density for that distance, it moves on to the second distance value. Now it simultaneously fits column density values to the two distance values with the requirement that the second column density value is not less than the column density at the previous distance value. In this way we can guarantee that the fit will always be monotonically increasing.

The program continues in this fashion, adding new distance values and trying every column density combination, until it has run through every possible column density value at each distance in our stand-in distance array, provided that the fit is always increasing. Every combination of column densities as a function of distance that are generated by this process is saved as a new array, this makes

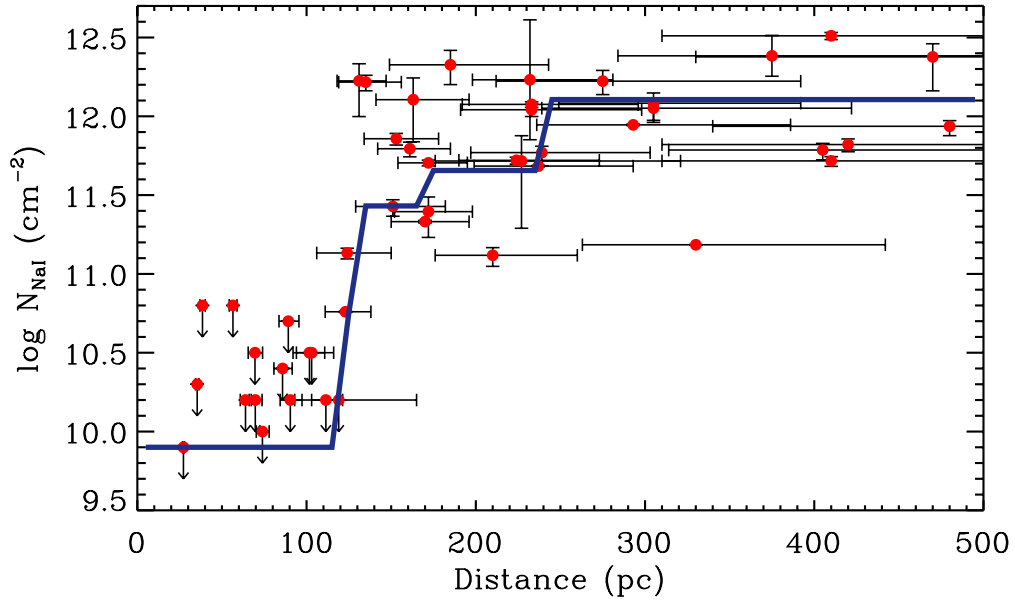
the process very computationally expensive. After the program has created and saved each possible monotonic fit, a χ^2 is evaluated for each possible profile and the fit with the lowest χ^2 corresponds to the best fit to the data. Figure 4.8 shows the results of this process.

4.3 Volume Densities from the Monotonic Fits

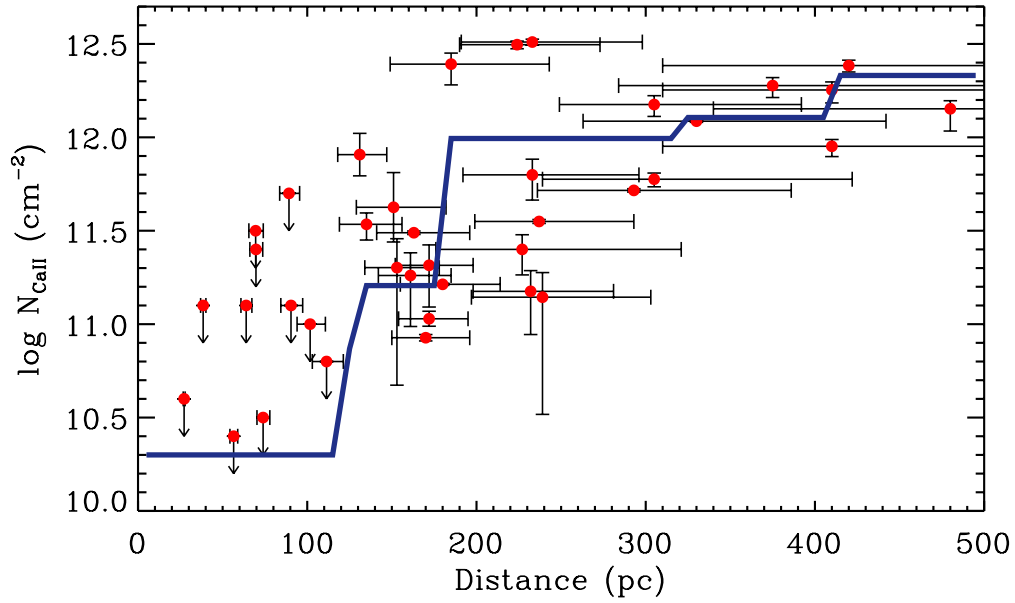
Once a satisfactory monotonic fit is made, a volume density profile can be calculated to place constraints on the locations of significant increases in absorbing material. Column densities up until this point have been calculated in log particles per square centimeter, it is a straightforward calculation to solve for the number of particles per cubic centimeter if you have information about the distance over which an increase in column density is taking place. First it is necessary to convert our sodium and calcium column densities to hydrogen column densities since any ISM cloud will be predominately composed of hydrogen.

Assuming a solar model for relative abundances of elements, our elements make up only a tiny fraction of the particle abundances in a typical ISM environment (sodium: $\frac{Na_{\odot}}{H_{\odot}} = 2.14 \times 10^{-6}$, calcium: $\frac{Ca_{\odot}}{H_{\odot}} = 2.29 \times 10^{-6}$, Gray (2005)). A more careful treatment of sodium resulted in a relation determined by Ferlet et al. (1985), where they found a linear relation between the abundances of neutral sodium and hydrogen that exists over three orders of magnitude, especially for low column densities. Equation 4.2 is a least-squares fit to their logarithmic correlation between NaI and (HI + H₂), where N(NaI) and N(HI + H₂) are in cm⁻².

$$\log N(\text{Na I}) = 1.04[\log N(\text{H I} + \text{H}_2)] - 9.09 \quad (4.2)$$



(a)



(b)

Figure 4.8: The brute force monotonic fit to the sodium (a) and calcium (b) data. Until the first real detection of sodium absorption, the fit was forced to remain at a column density below the upper limit values for inside the Local Bubble. After ~ 120 parsecs, the program was free to test values of column density for each distance value.

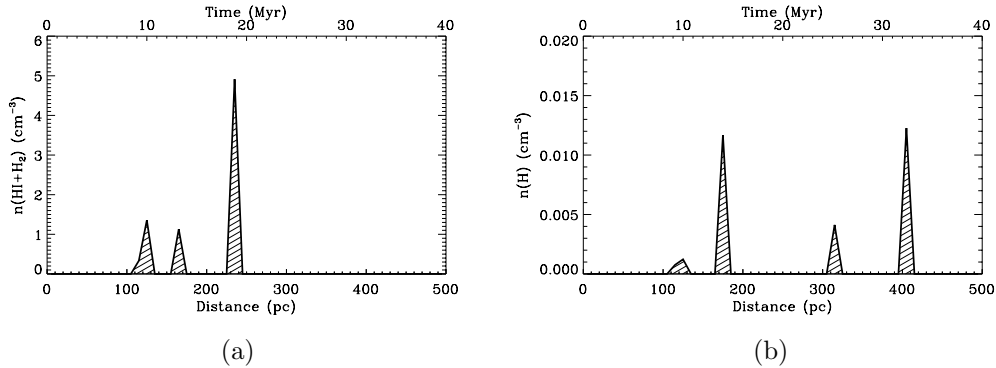


Figure 4.9: The volume plots of sodium (a) and calcium (b) determined from the brute force method described in §4.2.2.

Once we have transformed our column densities into hydrogen column densities, we can determine volume densities. This is accomplished by taking the increase in column density at each data point, and dividing by the distance represented by each data point. For the monotonic fit, each increase in distance corresponds to 10 parsecs, while the Boltzmann fit was created from an array of 10,000 elements, so each increase in distance for the Boltzmann fits was only 0.05 parsecs.

4.3.1 Volume Densities from the Brute Force Fits

The volume densities found from the sodium and calcium data are plotted in Figure 4.9. As of yet, no relationship (similar to the one found by Ferlet) has been found to relate calcium abundances to total hydrogen abundances, so we have plotted the total volume density of hydrogen based off of solar abundances.

Regions of high column densities as determined from the brute force monotonic fit are summarized in Tables 4.1 and 4.2. Time since interaction (TSI) is the approximate time that an encounter with the cloud might have happened, as

Table 4.1. Cloud Parameters determined from the Sodium Data

Cloud	TSI Myr	v km s ⁻¹	$n(\text{NaI})$ cm ⁻³	$n(\text{HI}+\text{H}_2)^{\text{a}}$ cm ⁻³
Do	10-11	23	4.25×10^{-9}	0.84
Re	12-13	18	5.94×10^{-9}	1.13
Mi	18-19	20	2.67×10^{-8}	4.92

^aCalculated using NaI-HI relationship in Ferlet et al. (1985)

Table 4.2. Cloud Parameters determined from the Calcium Data

Cloud	TSI Myr	v km s ⁻¹	$n(\text{CaII})$ cm ⁻³	$n(\text{H})^{\text{a}}$ cm ⁻³
Fa	9-10	22	2.28×10^{-9}	0.000997
So	14-15	24	2.67×10^{-8}	0.0117
La	25-26	22	9.45×10^{-9}	0.00412
Ti	32-33	-18	2.81×10^{-8}	0.0123

^aCalculated using solar abundance of calcium from Table 16.3 in Gray (2005)

determined from approximate distance to the absorbing material and the current solar velocity with respect to the LSR obtained from Schönrich et al. (2010). As we will see in the next chapter, relative ISM-Sun velocities can also have an effect on the size and shape of the heliosphere, so we estimate velocities for regions of high column densities by choosing the velocity of the strongest absorber in the region in which the cloud resides.

4.3.2 Volume Densities from the Boltzmann Fits

It was clear after the monotonic column density profiles were completed via the brute force method and the Boltzmann method that the brute force fit was better able to fit large increases in column density over short distances. Because of this, we feel that the volume densities derived from the brute force method do a better job of representing the increases in column densities that we would find in the ISM. However for completeness, we have plotted volume density profiles derived from the Boltzmann fits. One thing these volume profiles accomplish that the brute force volume profiles do not is that these profiles exhibit a slow gradual increase in volume density, with maximum density occurring at the center of the cloud. However, the large clouds implied by this method are just not seen in the data. Both the sodium and calcium monotonic fits suggest the existence of clouds that are 200 to 300 parsecs in size, and we see too much small scale variation in the data to support this.

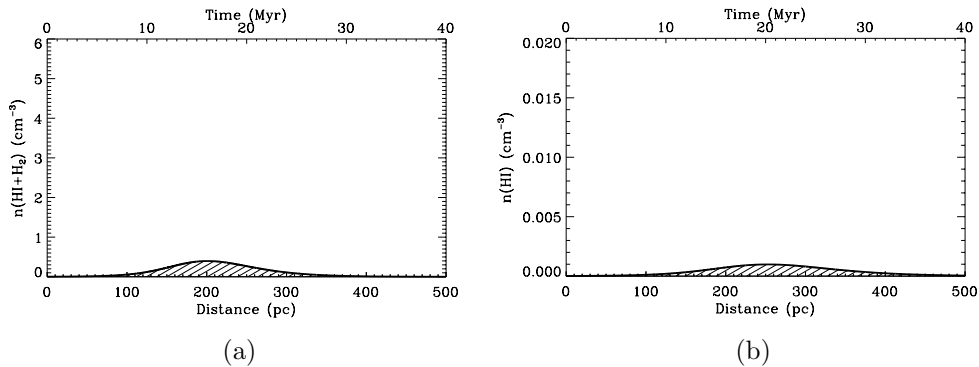


Figure 4.10: The volume plots of sodium (a) and calcium (b) determined from the Boltzmann method described in 4.2.1.

Drawbacks of the Monotonic Profile

One of the downfalls of fitting a monotonically increasing function to the column density profile is simply that the data is not monotonic. Our spatially separated sight lines probe different regions in space, and this leads to apparent decreases in column density with increasing distances. The monotonic fits do their best to find the average between the low column density measurements and the high. As a result, the fits end up creating increases in column density that correspond to no physical cloud in space. The next section explores a different approach to determining volume densities.

4.4 The Component-by-Component Method

It has been clearly established that our data set is dominated by the effects of small scale spatial variations across the viewing cone. This is what has made it difficult to place strong location constraints on large amounts of absorbing material and subsequently construct volume densities that we feel accurately reflect the location and nature of the individual clouds in the Sun's historical trajectory. Another way to derive volume densities as a function of distance involves establishing where a single absorption component first shows up in the data, and tabulating every time a component having roughly the same characteristics shows up with increasing distance. This way we will be documenting component-by-component increases in column density instead of using a model to infer the locations of large amounts of ISM.

We started by focusing on the region of the sodium velocity histogram (Figure 3.20) between 14 and 24 km s^{-1} , where we see a large number of ISM components. It is unlikely that this entire range of velocities is due to the motion of one cloud,

Table 4.3. Mean Component Parameters determined from the Sodium Data via the Component-by-Component Method

Cloud	Velocity Range km s ⁻¹	Mean v km s ⁻¹	Mean b km s ⁻¹	Mean $\log n(\text{NaI})$ cm ⁻²	Cloud Detections
A	22 - 24	23.02 ± 0.48	1.6 ± 1.1	11.124 ± 0.091	14
B	20 - 22	20.97 ± 0.55	1.54 ± 0.63	10.67 ± 0.61	8
C	18 - 20	18.99 ± 0.46	1.48 ± 0.80	11.28 ± 0.19	5
D	16 - 18	17.10 ± 0.40	2.4 ± 1.4	11.34 ± 0.52	4
E	14 - 16	14.71 ± 0.99	1.20 ± 0.62	10.67 ± 0.20	5

so the region was divided up into five 2 km s⁻¹ bins, for which we found the mean velocity of components in each bin as well as the mean Doppler parameters and column densities. While all column densities that resided in these velocity ranges were included in the mean parameter calculations, components with Doppler parameters greater than 5 km s⁻¹ were rejected since these were components used to represent the small amounts of excess absorption from weak, unresolved ISM clouds. These high Doppler parameters correspond to non-physical ISM temperature and components with these high values were left out of the calculations of mean cloud parameters. Table 4.3 lists the ranges of each velocity bin chosen in this process and the mean cloud parameters associated with clouds found within those ranges. The entire range of ISM component velocities were searched in this manner, however there were no other components with similar velocities, Doppler parameters, and column densities that appeared more than 4 times.

Components that fall within the parameter ranges in Table 4.3 are considered to be detections of the same cloud. Number of detections is listed in the last column of Table 4.3. Maps of each cloud found via this process are shown in Figure 4.11.

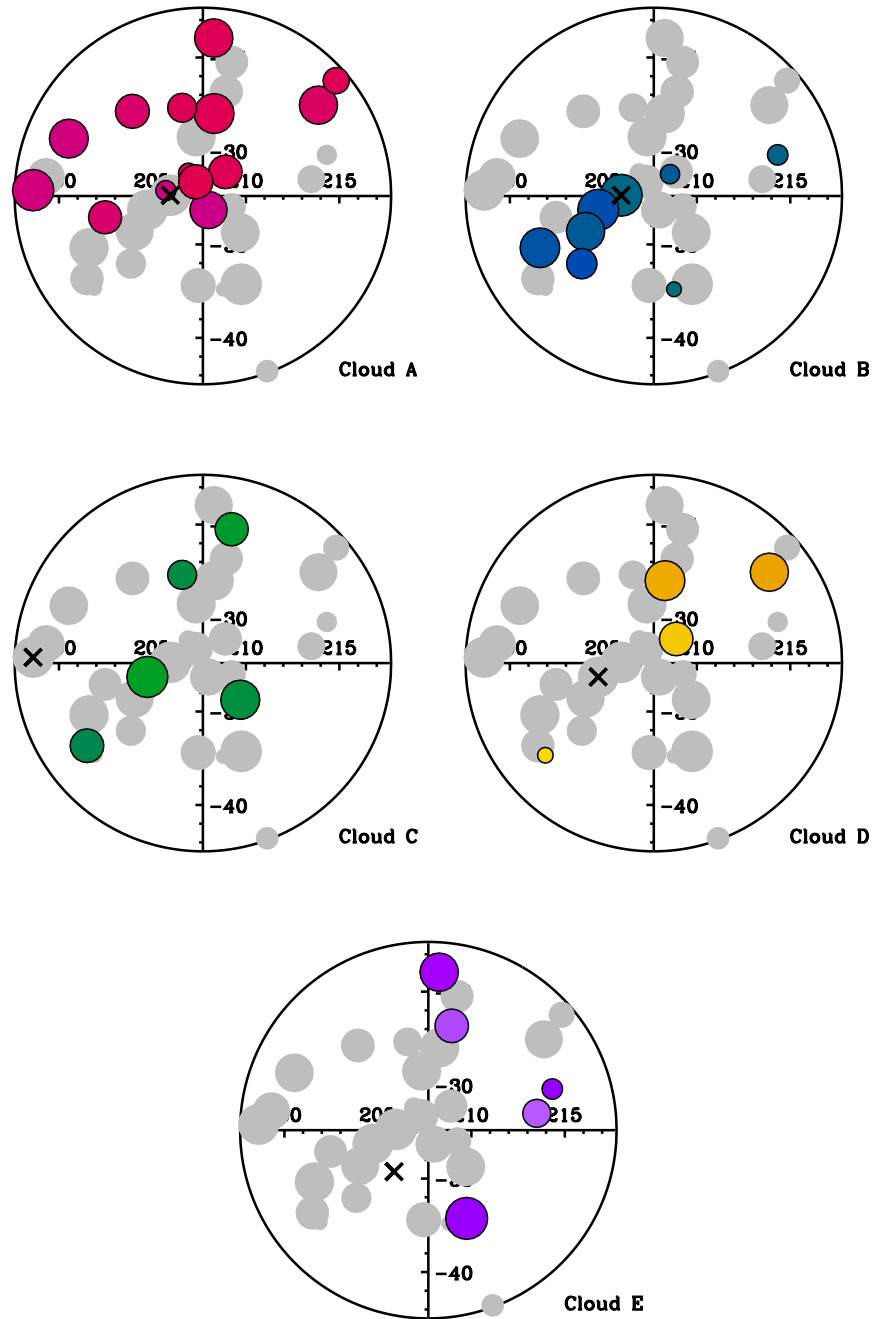


Figure 4.11: Map of sodium ISM absorption for the 5 clouds with more than 4 detections as determined via the component-by-component method. Size of symbol is inversely proportional to distance of sight line, shades of color within each plot corresponds to column density. Sight lines marked with a gray symbol correspond to non-detections. For each cloud, the location of the sight line of the last non-detection of each cloud is denoted by an “x.”

Now we can search our sodium data set for the first detection of each cloud. Once we find the observation that contains the first detection of a particular cloud, the observation immediately preceding it (with no detection) will give us a lower limit on distance to the absorbing medium since the absorption must occur after that star in order to be detected in the next absorption profile.

Cloud A is first detected in the absorption profile for HD28843 at a distance of 131 parsecs. The star immediately preceding it, or the last non-detection of this cloud, is from HD30020 at a distance of 124 parsecs. We will use the distances to these two sight lines at the upper and lower distance constraints for Cloud A. This means that an average log column density increase of 11.124 cm^{-2} is taking place over a distance of 7 parsecs. Using once more the neutral sodium to neutral hydrogen relation from Ferlet et al. (1985), we can calculate the hydrogen number density for this cloud, and after dividing this value by the distance, we arrive at a hydrogen volume density for Cloud A of 1.25 cm^{-3} .

Cloud B is first seen in absorption towards HD30020 at a distance of 124 parsecs. Last non-detection of Cloud B is HD27863 at a distance of 123 parsecs. These distance constraints imply an average increase in log column density of 10.67 cm^{-2} in just one parsec, which translates into a column density of 3.24 cm^{-3} .

The Cloud C increase occurs between the last non-detection towards HD28843 at a distance of 131 parsecs and the first detection at HD29554 at a distance of 135 parsecs, separated by 4 parsecs. This leads to a volume density of 3.13 cm^{-3} .

Cloud D must reside between the last non-detection towards HD29554 at a distance of 135 parsecs and the first detection at HD32468 at a distance of 151 parsecs, separated by 16 parsecs, resulting in a volume density of 0.89 cm^{-3} .

Cloud E is first seen towards HD28763 at a distance of 123 parsecs and is not seen in the sight line immediately preceding it: HD29173 at a distance of

Table 4.4. Summary of Clouds found Via the Component-by-Component Method

Cloud	Constraint parsecs	$n(\text{HI} + \text{H}_2)$ cm^{-3}
A	7	1.218 ± 0.016
B	1	5.46 ± 0.68
C	4	2.05 ± 0.13
D	16	0.651 ± 0.028
E	4	0.9867 ± 0.0088

119 parsecs. This means the increase must occur over 4 parsecs, which leads to a volume density of 0.81 cm^{-3} .

We have calculated the distance constraints on our clouds without incorporating the errors in stellar distances. For some of these clouds, the lower error bar on the upper distance constraint actually brings the upper distance constraint nearer to the Sun than the star we are using as a lower distance constraint. In some cases, this could effectively change the distance order of our upper and lower distance constraints of our clouds. In almost all cases (except for possibly Clouds C and E, which each have a last non-detection that is spatially separated from the other sight lines with detections) we are relatively safe in the assertion that the upper distance constraint we have used does lie beyond the lower distance constraint, simply based on where we see the absorption. In a way this information serves to reduce the error bars on the stellar distance measurements. However, the distance errors do mean that distances between these stars could be much less than one parsec or as great as the total range in errors for the two stars used as distance constraints. This will also have an effect on the actual volume densities of these clouds. The errors on volume density were calculated by propagating the errors

from the observation of each component with the highest precision measurement of the column density.

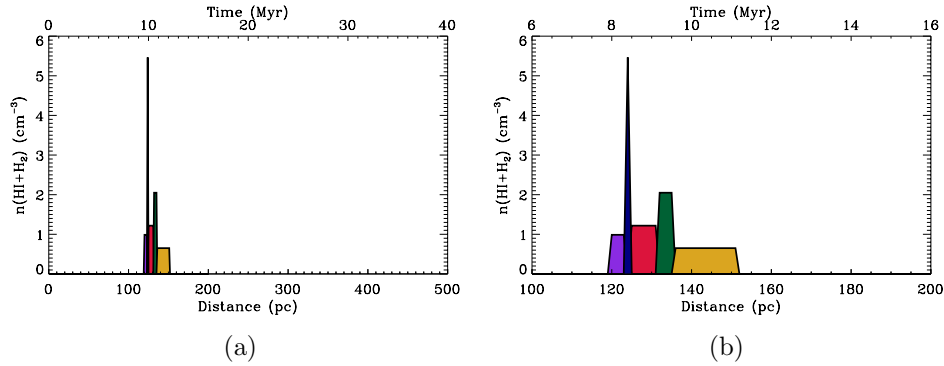


Figure 4.12: Plot (a) shows the volume density profile as determined from the component-by-component method. Colors match the maps of sight lines that probe each cloud shown in Figure 4.11. Plot (b) shows a close-up of the region surrounding the edge of the Local Bubble.

Note

An important caveat must be mentioned here. The volume densities calculated in this chapter by any method are necessarily lower limits on volume density for each cloud. Since we lack any information on the internal structure of the ISM between two distance measurements, we could be looking at a cloud that fills the entire distance between the two stars (which is what is assumed here, giving us a lower limit on the density) or we could be looking at mostly empty space between the two stars, where an intervening cloud takes up only a tiny fraction of the distance. If the latter were the case, the cloud would have a much higher density than calculated here, due to the fact that the same amount of material is compressed into a smaller volume instead of being stretched between two stars. Since it is unlikely that these ISM clouds are taking up the entire volume between the stars, it is very possible that each cloud is smaller than these

distance constraints, and in turn possess higher volume densities which, as we will soon see, have a greater effect on the compression of the heliosphere.

Chapter 5

Discussion

In Chapter 4 we discovered multiple ways to determine the size, location, and volume densities of general trends of increasing ISM as well as individual clouds. In this chapter we will explore what these results mean for our historical heliosphere. We can use the volume densities of these clouds, along with their velocities to determine what sort of effect individual clouds would have on the size of our heliosphere, while the locations of these clouds will tell us when in our history we would have encountered such a cloud. Also in this chapter we will address the relationship between size of the heliosphere and GCR flux at 1 AU.

5.1 Heliosphere Size

It's been postulated (Frisch 2004; Florinski et al. 2003a) and extensively modeled (Müller et al. 2009; Zank & Frisch 1999) that different interstellar environments may produce a change in the parameters of the heliosphere as well as dictate the filtering of specific ions and neutral particles as they propagate inwards towards the planets.

The sensitivity of the heliospheric variations in response to encounters with ISM clouds has been modeled by Müller et al. (2006) where they tested the heliospheric response to a range of low-density interstellar boundary conditions probing various combinations of possible ISM environments: densities ranging from 0.005

to 15 cm^{-3} , ionizations up to 100% and Sun-cloud velocities up to 100 km s^{-1} . Among the results of their 27 different models, the most striking variation was seen in the size of the heliosphere.

One of the major results of Müller's modeling was the development of correlations between the positions of the three major constituents of the heliosphere. The entire system is required to be pressure balanced so the point where the ISM and solar flows meet and divert from each other can be determined from combining the thermal (nkT) and ram (ρv^2) contributions to the pressures for both the ISM and solar wind (Holzer 1989).

The distance to this pressure balance on the stagnation axis at the point of the heliopause is calculated under Rankine-Hugoniot shock conditions, which are a set of conservation laws in magnetohydrodynamics that govern how an ideal gas operates under adiabatic conditions at an abrupt change such as a shock. It is also assumed that the material inside the heliosheath is incompressible, and that the two plasmas (ISM and SW) residing inside the heliosheath do not cross the heliopause and mix with one another (Suess & Nerney 1990).

$$r_{HP} = r_0 \sqrt{\frac{\rho_1 v_{SW}^2}{P_{ISM}}} \left(1 - \frac{v_{ISM}^2}{v_{SW}^2} \right)^{5/4} \quad (5.1)$$

In Equation 5.1, ρ_1 and v_{SW} are the mass density and the velocity of the solar wind. P_{ISM} is the total interstellar pressure which in a supersonic ISM is dominated by the ram pressure. r_0 is a product of the theoretical calculations, and is a fit between model results and calculated values of r_{HP} , which yield a result of 1.70 AU for r_0 (Müller et al. 2009).

Müller's equations also make the distinction between the plasma and neutral contribution to the ISM pressures. Unfortunately both of the methods we used

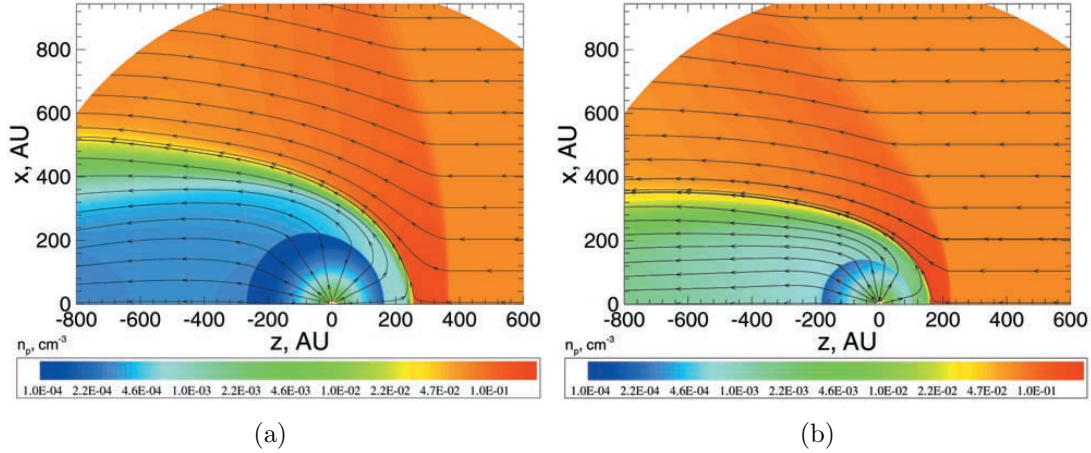


Figure 5.1: Models of the heliosphere embedded in an ISM cloud with no neutrals (a), and with the inclusion of neutrals (b). From Florinski et al. (2003b)

for translating our sodium and calcium column densities into hydrogen densities yield no information about the fraction of ionized hydrogen in our clouds. Using the solar model resulted in an total hydrogen density while the relation in Ferlet et al. (1985) yielded a total neutral hydrogen density which included diatomic hydrogen. This might not be a trivial deviation from what the equations are meant for. Florinski et al. (2003b) model a heliosphere embedded in an ISM cloud completely devoid of neutral particles. They found that the inclusion of ISM neutral hydrogen reduced the heliosphere by 60%. Figure 5.1 shows the two cases from this study. The difference is similar to the environment of the Local Bubble (which is relatively devoid of ISM neutrals) and the environment of a CNM cloud.

Granted we do have information about neutral hydrogen and we are safe in the assumption that the majority of hydrogen in these clouds will reside in this state, but the addition of H_2 or our lack of knowledge about the fractional ionization of hydrogen in these clouds might lead to errors in our calculated extent of the

heliosphere components based on these equations.

In addition to empirically determining the distance to the heliopause, Müller et al. (2006) also found a strong correlation in the position of the termination and bow shocks with respect to the heliopause. Because the whole system is pressure balanced, the position of the termination shock is coupled to the heliopause via the linear relation:

$$r_{HP} = (1.40 \pm 0.03)r_{TS}. \quad (5.2)$$

and the bow shock:

$$r_{BS} = (1.95 \pm 0.05)r_{HP}. \quad (5.3)$$

5.1.1 Historical Heliospheric Response

When calculating the heliospheric response to our clouds, we have adopted the same solar wind parameters used by Müller et al. (2006) in his parametric study.

At 1 AU from the Sun, the solar wind is assumed to be independent of longitude, latitude and time, with values of 5.0 cm^{-3} for plasma density, a temperature of 100,000 K and a radial velocity of 400 km s^{-1} . These values, along with contemporary measurements for the CISM ($v = 26.3 \text{ km s}^{-1}$, $T \sim 6300 \pm 340 \text{ K}$) place the current distance to the termination shock at 99 AU in the upwind direction (into the ISM flow vector) and 216 AU in the downwind direction. The heliopause resides at 148 AU, and as the LISM in the Local Bubble is supersonic, a bow shock forms at 285 AU in the upwind direction (Müller et al. 2009).

We have finally arrived at the point where we may begin to reconstruct our heliospheric history. Since we feel that the component by component method for

Table 5.1. Heliosphere Parameters determined from the Sodium Data

Cloud	TS (AU)	HP (AU)	BS (AU)
A	40.45 ± 0.89	56.64 ± 0.37	110.4 ± 2.8
B	20.73 ± 0.45	29.0 ± 2.0	56.6 ± 1.5
C	36.98 ± 0.81	51.8 ± 1.7	100.9 ± 2.6
D	72.1 ± 1.6	101.0 ± 2.3	197.0 ± 5.1
E	64.9 ± 1.4	90.87 ± 0.40	177.2 ± 4.5
S ^a	99	148	285

^aContemporary heliosphere boundaries from Müller et al. (2009).

determining volume densities described in §4.4 did the the best job at locating and reconstructing ISM density profiles, we will calculate the heliosphere size based on these clouds. Table 5.1 lists our calculated heliosphere sizes when the Sun was passing through each of the clouds detected.

Each time the Sun passed through one of these clouds, its heliosphere suffered a significant decrease in size. At its greatest reduction due to Cloud B, the termination shock lies very near to Uranus' distance from the Sun assuming that the ISM flow vector is in the plane of the ecliptic. If the ISM was streaming towards the Sun at an angle above or below the ecliptic, the reduction would not be as great near the planets since the point of greatest compression will occur along the stagnation axis.

When the Sun was passing through Cloud B, Uranus was likely spending part of its orbit outside the termination shock and inside the inner heliosheath. Here Uranus was probably subject to the higher thermal plasma velocities thought to exist downwind of the heliopause as well as a higher GCR flux and energetic particles in this region. During this same time, Neptune would have likely crossed

the heliopause during its orbit where it would have spent some time in the outer heliosheath's shocked ISM material. Also in this region it would have encountered a high number density of interstellar neutrals found in the neutral hydrogen wall downwind of the bow shock. A planet moving through this region would likely experience increased dust deposition on its surface and also be subject to atmospheric drag (Yeghikyan & Fahr 2004a).

Based on the information we have, none of the clouds in our data have the ability to compress the heliosphere to within one AU. Such a cloud would have to possess a density of $\sim 1500 \text{ cm}^{-3}$ or have a relative Sun-ISM velocity of 354 km s^{-1} to have such a dramatic effect (Müller et al. 2006). These values come directly from a simple evaluation of the empirical relationships, a more thorough evaluation would have to consider other physical processes which might come into play at such extreme compressions of the heliosphere (Yeghikyan & Fahr 2004b). However, it still is possible that a cloud possessing such a density could have passed over the heliosphere at some point since our densities derived in Chapter 4 are lower limits on the density.

While the heliosphere remains well outside of Earth's orbit for our encounters, there will still probably have been an appreciable change in the particle environment of the inner solar system. At the distance of Jupiter's orbit, the ratio of ISM neutrals to solar wind ions depends greatly on ISM velocity and density. Models from (Müller et al. 2006) show the ratio ranging greatly from between 7% and 25% for the current solar galactic environment and up to 120% when the termination shock is at Saturn's orbit.

5.1.2 Cosmic Ray Modulation

The size of the heliosphere as well as the particle environment inside the termination shock will affect the propagation of GCRs across each of the heliosphere boundaries. Müller et al. (2006) makes use of the self-consistent model developed by Florinski et al. (2003a) that includes the three principle species of particles found in the ISM: interstellar ions, neutrals, and GCRs to calculate the modulation of cosmic rays in their ISM environment models.

The derivation of the cosmic ray transport model is complicated, so a comparison to the GCR spectra based on calculations made by Müller et al. (2006) is what will be discussed here. The reader is referred to Florinski et al. (2003a) and Florinski & Zank (2006) for a more complete description of the GCR transport model.

Müller calculates the GCR modulation for three of his models. Figure 5.2 show's Müller's computed high-energy proton spectra for each of these models. In each case, he also makes the distinction between the effects on the modulation from the two main sources of GCR modulation: by the heliosheath (I) and by the solar wind (II). Model 1 corresponds to the heliosphere being placed in a hot, low density, ionized environment, much like the conditions inside the Local Bubble ($T = 1.26 \times 10^6$ K, $n_{\text{tot}} = 0.05 \text{ cm}^{-3}$, $n_{\text{H}^0} = 0.05 \text{ cm}^{-3}$). Model 10 was meant to mimic the contemporary environment of the Sun surrounded by a cloud much like the local interstellar cloud ($T = 8000$ K, $n_{\text{tot}} = 0.24 \text{ cm}^{-3}$, $n_{\text{H}^0} = 0.14 \text{ cm}^{-3}$). Model 15 was meant to model the encounter of the Sun with a cool, neutral, dense ISM cloud ($T = 100$ K, $n_{\text{tot}} = 11.15 \text{ cm}^{-3}$, $n_{\text{H}^0} = 11.0 \text{ cm}^{-3}$). Each of the neutral hydrogen number densities calculated for our clouds are between the number densities for models 10 and 15, so we expect the GCR modulation of the

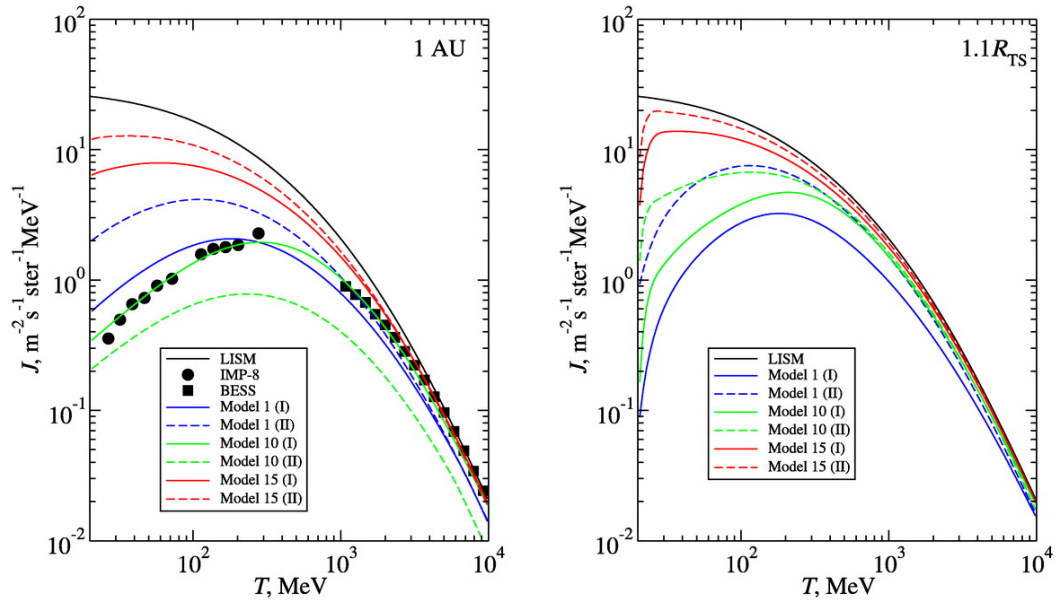


Figure 5.2: The high-energy proton GCR spectra for three models developed by Müller et al. (2006). The left-hand side shows the GCR flux at 1 AU, while the right shows the GCR flux just beyond the termination shock. Model 1 represents the heliosphere embedded in Local Bubble ISM, model 10 represents the contemporary circumheliospheric ISM, and model 15 represents an encounter with a high-density cloud.

heliosphere in our clouds to lie some where between these two.

The plots only show the high-energy region for cosmic rays since most of the low energy cosmic rays (T less than 10 MeV) are modulated out due to the solar wind (Bobik et al. 2010). The plot on the right side of 5.2 shows the GCR spectra right outside the termination shock for each ISM environment and each diffusion model. The plot on the left shows the same spectra at 1 AU. For an encounter with a cold dense ISM cloud like the one in model 15, we can see the number of 10^2 MeV GCRs increases by over an order of magnitude. This separation grows with increasing energies.

Chapter 6

Conclusions

About 9-12 million years ago, the Sun passed through a number of warm, neutral ISM clouds before it transitioned into the relatively empty and high temperature Local Bubble cavity. During this time, the heliosphere would have undergone changes due to the changing boundary conditions imposed on it by the surrounding ISM. This work has focused on the effect of an increase of neutral hydrogen number density of the size of the heliosphere.

6.1 Summary of Results

We find that during this transitional period, the termination shock occasionally crossed Neptune's orbit, and in one case possibly moved within Uranus' orbit. During these times, Uranus and Neptune were spending part of their orbit in shocked solar wind, and Neptune even crossed over the heliopause into shocked LISM material. In this region Neptune would have been subject to a high number density of neutral ISM particles found in the hydrogen wall as well as experience an increased number of charged particles found throughout the heliosheath.

Based on our calculations, none of the clouds we have detected within our recent solar history have had the densities or velocities required to compress the heliosphere to within 1 AU. Comparing our number densities to the GCR modulation effects calculated for ISM conditions modeled by Müller suggests that there

could have been an increase in the GCR flux at Earth by as much as an order of magnitude for the highest energy GCRs.

There is the possibility that a dense cloud might have passed over the heliosphere in our past and would have not been detected in this study. We have only been able to measure a clouds radial velocity, we have not considered a cloud's possible transverse velocity. This opens the possibility that a cloud we might have encountered in the past might have moved out of our Sun's past trajectory entirely. This also means that some of the clouds we detect in this path were not there when the Sun was moving through the region.

It is unknown whether or not evidence of an increase in the GCR flux suggested here could be found in Earth's geologic record. If we had experienced a heliosphere compression to within 1 AU, the consequences might have been very easily recognized. Such a removal of the heliosphere would have meant that the GCR flux at Earth would be the same as in the Local Bubble, and this dramatic increase could manifest itself in a large ^{10}Be increase in our geologic record.

6.2 Future Work

The component-by-component method would benefit greatly from higher resolution observations which would allow us to more easily distinguish absorption components from different clouds and reduce the information lost due to blending in the lower resolution observations.

6.2.1 The Literal Future

Data has been obtained for the same analysis to be completed for ISM clouds in the Sun's immediate path, again out to a distance of 500 parsecs. This will be

especially interesting since the solar system has already begun to transition out of the LIC where it will spend some time in the hot Local Bubble environment before moving into the G Cloud. As we have seen, these cloudlets in the ISM lack the densities required to be of much interest when looking for drastic changes in the size of the heliosphere, but we should be able to look ahead to the time when the Sun will be exiting the Local Bubble and search for heliosphere-compressing clouds there.

Bibliography

- Allen, D., Pickering, K., Duncan, B., & Damon, M. 2010, *Journal of Geophysical Research (Atmospheres)*, 115, D22301
- Aroesty, J., Zimmerman, R., & Logan, J. 1991, *Human Support Issues and Systems for the Space Exploration Initiative: Results from Project Outreach (RAND Publications)*
- Bevington, P. R. 2003, *Data Reduction and Error Analysis for the Physical Sciences (McGraw-Hill)*
- Bobik, P., Boschini, M. J., Consolandi, C., Della Torre, S., Gervasi, M., Grandi, D., Kudela, K., Pensotti, S., & Rancoita, P. G. 2010, *ArXiv e-prints*
- Bzowski, M., Fahr, H. J., & Rucinski, D. 1996, *ICAR*, 124, 209
- Carslaw, K. S., Harrison, R. G., & Kirkby, J. 2002, *Science*, 298, 1732
- Dame, T. M., Ungerechts, H., Cohen, R. S., de Geus, E. J., Grenier, I. A., May, J., Murphy, D. C., Nyman, L., & Thaddeus, P. 1987, *ApJ*, 322, 706
- Decker, R. B., Krimigis, S. M., Roelof, E. C., Hill, M. E., Armstrong, T. P., Gloeckler, G., Hamilton, D. C., & Lanzerotti, L. J. 2005, *Science*, 309, 2020
- Dehnen, W., & Binney, J. J. 1998, *MNRAS*, 298, 387
- Erlykin, A. D., & Wolfendale, A. W. 2010, *Surveys in Geophysics*, 31, 383
- Ferlet, R., Vidal-Madjar, A., & Gry, C. 1985, *ApJ*, 298, 838

- Florinski, V., & Zank, G. P. 2006, *GRL*, 33, L15110
- Florinski, V., Zank, G. P., & Axford, W. I. 2003a, *GRL*, 30, 2206
- Florinski, V., Zank, G. P., & Pogorelov, N. V. 2003b, *Journal of Geophysical Research (Space Physics)*, 108, 1228
- Frisch, P. C. 1995, *SSRv*, 72, 499
- Frisch, P. C. 2004, in *American Institute of Physics Conference Series*, Vol. 719, *Physics of the Outer Heliosphere*, ed. V. Florinski, N. V. Pogorelov, & G. P. Zank, 404–411
- Frisch, P. C., & Mueller, H. 2010, *ArXiv e-prints*
- Gies, D. R., & Helsel, J. W. 2005, *ApJ*, 626, 844
- Gosling, J. T. 1964, *JGR*, 69, 1233
- Gray, D. F. 2005, *The Observations and Analysis of Stellar Photospheres* (Cambridge University Press)
- Grenier, S., Baylac, M., Rolland, L., Burnage, R., Arenou, F., Briot, D., Delmas, F., Dufflot, M., Genty, V., Gómez, A. E., Halbwegs, J., Marouard, M., Oblak, E., & Sellier, A. 1999, *A&AS*, 137, 451
- Heiles, C., & Troland, T. H. 2003, *ApJ*, 586, 1067
- Holzer, T. E. 1989, *ARA&A*, 27, 199
- Hoyle, F., & Lyttleton, R. A. 1939, in *Proceedings of the Cambridge Philosophical Society*, Vol. 35, *Proceedings of the Cambridge Philosophical Society*, 405

- Lallement, R., Welsh, B. Y., Vergely, J. L., Crifo, F., & Sfeir, D. 2003, *A&A*, 411, 447
- Liewer, P. C., Mewaldt, R. A., Ayon, J. A., & Wallace, R. A. 2000, in American Institute of Physics Conference Series, Vol. 504, Space Technology and Applications International Forum, ed. M. S. El-Genk, 911–916
- Markson, R. 1981, *Nature*, 291, 304
- McCracken, K. G., McDonald, F. B., Beer, J., Raisbeck, G., & Yiou, F. 2004, *Journal of Geophysical Research (Space Physics)*, 109, A12103
- McCray, R. A. 1987, in *Spectroscopy of Astrophysical Plasmas*, ed. A. Dalgarno & D. Layzer, 255–278
- McKee, C. F., & Ostriker, J. P. 1977, *ApJ*, 218, 148
- Miller, S. L. 1953, *Science*, 117, 528
- Müller, H., Frisch, P. C., Fields, B. D., & Zank, G. P. 2009, *SSRv*, 143, 415
- Müller, H., Frisch, P. C., Florinski, V., & Zank, G. P. 2006, *ApJ*, 647, 1491
- Nordström, B., Mayor, M., Andersen, J., Holmberg, J., Pont, F., Jørgensen, B. R., Olsen, E. H., Udry, S., & Mowlavi, N. 2004, *A&A*, 418, 989
- Parker, E. N. 2006, *Scientific American*, 294, 40
- Pavlov, A. A., Toon, O. B., Pavlov, A. K., Bally, J., & Pollard, D. 2005, *GRL*, 32, L03705
- Redfield, S. 2006, in *Astronomical Society of the Pacific Conference Series*, Vol. 352, *New Horizons in Astronomy: Frank N. Bash Symposium*, ed. S. J. Kannappan, S. Redfield, J. E. Kessler-Silacci, M. Landriau, & N. Drory, 79

- Redfield, S. 2007, *ApJL*, 656, L97
- . 2009, *SSRv*, 143, 323
- Redfield, S., & Linsky, J. L. 2000, *ApJ*, 534, 825
- . 2002, *ApJS*, 139, 439
- . 2004, *ApJ*, 613, 1004
- . 2008, *ApJ*, 673, 283
- Savage, B. D., & Sembach, K. R. 1991, *ApJ*, 379, 245
- Schönrich, R., Binney, J., & Dehnen, W. 2010, *MNRAS*, 403, 1829
- Shapley, H. 1921, *Journal of Geology*, 29, 502
- Shaviv, N. J. 2003, *NA*, 8, 39
- Shorlin, S. L. S., Wade, G. A., Donati, J., Landstreet, J. D., Petit, P., Sigut, T. A. A., & Strasser, S. 2002, *A&A*, 392, 637
- Simmons, G. F. 1996, *Calculus with Analytic Geometry* (McGraw-Hill)
- Stawikowski, A., & Glebocki, R. 1994, *ACA*, 44, 33
- Suess, S. T., & Nerney, S. 1990, *JGR*, 95, 6403
- U. S. Space Studies Board, N. R. C., & Committee On Solar Space Physics. 2004, *Exploration of the outer heliosphere and the local interstellar medium*, Tech. rep.
- Webber, W. R., & Intriligator, D. S. 2011, ArXiv e-prints

Yeghikyan, A., & Fahr, H. 2004a, *A&A*, 415, 763

—. 2004b, *A&A*, 425, 1113

Zachos, J., Pagani, M., Sloan, L., Thomas, E., & Billups, K. 2001, *Science*, 292, 686

Zank, G. P., & Frisch, P. C. 1999, *ApJ*, 518, 965

Zank, G. P., & Müller, H. 2003, *Journal of Geophysical Research (Space Physics)*, 108, 1240